STRING PHENOMENOLOGY IN THE ERA OF LHC

A Dissertation

by

JAMES A. MAXIN

Submitted to the Office of Graduate Studies of
Texas A&M University
in partial fulfillment of the requirements for the degree of

DOCTOR OF PHILOSOPHY

August 2010

Major Subject: Physics

STRING PHENOMENOLOGY IN THE ERA OF LHC

A Dissertation

by

JAMES A. MAXIN

Submitted to the Office of Graduate Studies of
Texas A&M University
in partial fulfillment of the requirements for the degree of

DOCTOR OF PHILOSOPHY

Approved by:

Chair of Committee,	Dimitri V. Nanopoulos
Committee Members,	Bhaskar Dutta
	Christopher Pope
	Stephen Fulling
Head of Department,	Edward Fry

August 2010

Major Subject: Physics

ABSTRACT

String Phenomenology in the Era of LHC. (August 2010)

James A. Maxin, B.S., Southern Illinois University

Chair of Advisory Committee: Dr. Dimitri V. Nanopoulos

The low-energy supersymmetry phenomenology for specific classes of string compactifications is investigated given that the low-energy physics may provide a clue as to the structure of the fundamental theory at high energy scales. The one-parameter model (OPM), a highly constrained subset of minimal Supergravity where all the soft-supersymmetry breaking terms may be fixed in terms of the gaugino mass, is studied, in addition to a three-family Pati-Salam model constructed from intersecting $D6$-branes. Furthermore, the phenomenology of gravity mediated supersymmetry breaking F-theory $SU(5)$ and $SO(10)$ models, as well as $\mathcal{F}$-$SU(5)$ models with vector-like particles, are examined. We determine the viable parameter space that satisfies all the latest experimental constraints, including the most recent WMAP relic neutralino abundance observations, and find it to be consistent with the CDMS II and other concurrent direct-detection experiments. Moreover, we compute the gamma-ray flux and cross-sections of neutralino annihilations into gamma-rays and compare to the published Fermi-LAT satellite telescope measurements. In F-theory $SU(5)$ and $SO(10)$ models, we predict the exact small deviation of the gaugino mass relation at two-loop level near the electroweak scale, which can be tested at the colliders. Moreover, in $\mathcal{F}$-$SU(5)$, we predict the precise deviations from the mSUGRA gaugino mass relations due to the presence of the vector-like particles, also testable at the colliders. The compilation of all these results form a comprehensive collection of predictions with which to evaluate these string models alongside anticipated experimental discoveries in the coming decade.

ACKNOWLEDGMENTS

This research was supported in part by the Mitchell-Heep Chair in High Energy Physics (CMC), by the Cambridge-Mitchell Collaboration in Theoretical Cosmology, and by the DOE grant DE-FG03-95-Er-40917.

TABLE OF CONTENTS

CHAPTER Page

LIST OF TABLES

TABLE Page

TABLE Page

TABLE Page

LIST OF FIGURES

FIGURE Page

FIGURE Page

FIGURE Page

FIGURE Page

FIGURE Page

CHAPTER I

INTRODUCTION

A. Low-energy Phenomenology

As science leaps into the Large Hadron Collider (LHC) era, there is the much anticipated breakthrough of new physics. Specifically, we expect the discovery of supersymmetry, as well as the Higgs states necessary to break electroweak symmetry and stabilize the electroweak scale. Thus, comprehensive, concrete models derived from string theory are needed to formulate predictions of superpartner mass spectra and represent currently observed particle physics. However, at present there is no definitive worked out example capable of describing all physical phenomena in one complete mathematical framework. Certainly, the goal of string phenomenology is to construct a model that thoroughly explains all known particle physics, possibly predicts new phenomena, and can be substantiated at the LHC. The great challenge of string phenomenology is constructing realistic string models that allow us to make unique predictions that can be tested at the LHC, future International Linear Collider (ILC), and other experiments. If these predictions are confirmed in future experiments, we will possess strong evidence to support that string theory is indeed the correct fundamental description of nature.

In principle, it should be possible to derive all known physics in a top-down approach directly from a more fundamental theory such as string theory, as well as potentially predicting new and unexpected phenomena. Conversely, following a bottom-up approach, one may ask if it is possible to deduce the origin of new physics given such a signal at LHC. For example, in the case of low- energy supersymme-

---

This dissertation follows the style of Physical Review D.

try, it may be possible from the experimental data to deduce the structure of the fundamental theory at high energy scales which determines the soft-supersymmetry breaking terms and ultimately leads to electroweak symmetry breaking (EWSB).

This is the ambition of the research in this dissertation. The phenomenology of specific classes of string models are to be generated and investigated, and by analyzing the latest experimental data, the string models under scrutiny can be constrained and it may be ascertained whether the explicit string model under study is consistent with current experimental observation. Only then can the models under study offer distinct predictions testable at the colliders and other experiments. A summary of current experimental observations used in this research follows in the subsequent section.

B. Constraining the String Model

Observations in cosmology and astrophysics suggest the presence of a stable dark matter particle. Supersymmetry (SUSY) supplies a satisfactory candidate for a dark matter particle, where R-parity is conserved and the lightest supersymmetric particle (LSP) is stable [1], which is usually the lightest neutralino $\widetilde{\chi}_1^0$ [1, 2]. The Wilkinson Microwave Anisotropy Probe (WMAP) has completed a comprehensive sky survey and placed constraints on the neutralino relic density in the universe [3, 4]. The WMAP data sets constraints on the dark matter abundance in supersymmetric models and is a key factor in evaluating any particular model's experimental viability. Moreover, it is prudent to consider all possible relic neutralino scenarios, including Supercritical String Cosmology (SSC) [5, 6, 7] and the case where a neutralino LSP makes up a subdominant component of the dark matter density. The remaining fraction of the observed relic density in this situation where the LSP is a subdominant component would be composed of other particles, such as axions or cryptons, or

additional astrophysical matter.

Two proposed methods of discovering this weakly interacting massive particle (WIMP) are directly through WIMP interactions with ordinary matter and indirectly via the products of WIMP annihilations. The direct detection method searches for elastic scattering of WIMPs off nuclei in underground experiments [8, 9, 10, 11]. The experiments are conducted in deep underground laboratories in an effort to reduce the background to minimal levels. The indirect detection method seeks out debris resulting from WIMP annihilations in the galactic halo. One galactic process that could produce gamma-rays from WIMP annihilation is the process $\widetilde{\chi}_1^0\widetilde{\chi}_1^0 \to \gamma\gamma$, where two gamma-rays are produced directly from a WIMP annihilation, and another is $\widetilde{\chi}_1^0\widetilde{\chi}_1^0 \to q\overline{q} \to \pi^0 \to \gamma\gamma$. One such current experiment to measure the debris from WIMP annihilations is the Fermi gamma-ray space telescope [12] with new constraints on cross-sections of neutralino annihilations into two gamma-rays [13]. Analyses of direct detection cross-sections and gamma-ray flux, and cross-sections of neutralino annihilations into two gamma-rays within minimal Supergravity (or CMSSM) models have been completed [14, 15, 16, 17]. It is, however, a worthwhile pursuit to analyze the direct and indirect detection parameters in alternative frameworks, such as string models.

Recently, the Cryogenic Dark Matter Search (CDMS) II experiment has announced what may be the first positive evidence for the direct detection of WIMP-like dark matter [18], including the detection of two candidate events, although there is a 23% chance that these events could be due to background. These new CDMS II limits on the dark matter detection cross-section can be used to constrain the possible superpartner and Higgs spectra which may be observed at the LHC. Namely, only those spectra which possess an LSP consistent with the CDMS II constraints as well as all other constraints are viable. The discovery of a neutralino LSP at LHC

combined with data from direct and indirect detection experiments may shed direct light on the identity of the dark matter.

In addition, it is also imperative to implement constraints from more established experiments, such as the experimental limits on the Flavor Changing Neutral Current (FCNC) process $b \to s\gamma$ [19, 20], the anomalous magnetic moment of the muon, $g_\mu - 2$ [21], the process $B_s^0 \to \mu^+\mu^-$ [22], and the limit on the lightest CP-even Higgs boson mass [23]. These, combined with the WMAP, direct-detection, and indirect detection experiments, form an inclusive set of constraints with which to explore whether the structure of the underlying fundamental theory can be inferred in the model under study here.

The research presented in this dissertation is the result of a collaborative effort with Dimitri V. Nanopoulos, Van E. Mayes, Tianjun Li, and Joel W. Walker.

CHAPTER II

ONE-PARAMETER MODEL*

A. The One-parameter Model

No-scale supergravity (nSUGRA) [24] is a framework where it is possible to naturally explain radiative electroweak symmetry breaking (REWSB) [25, 26, 27] and correlate it with the gravitino mass, or more generally, the effective SUSY breaking scale. In the simplest no-scale models, the gravitino mass $m_{3/2}$ remains undetermined at the classical level, and is instead fixed by radiative corrections to be near the electroweak scale [24]. Thus, in this framework, we find that the scale of supersymmetry breaking is correlated with the electroweak scale [24]. Another striking feature of nSUGRA is that the cosmological constant vanishes at tree-level. Although it is presently known that the cosmological constant is in fact non-zero, its very small value is still consistent with the no-scale framework with small corrections. Furthermore, it is well-known that the Kähler moduli of Type I, IIB orientifold, and heterotic string compactifications have a classical no-scale structure [28, 29, 30]. The generic appearance of the no-scale structure across many string compactifications leads to the idea that supersymmetry breaking is moduli dominated.

In string models, supersymmetry breaking is typically performed in a hidden sector as well as through the universal moduli and dilaton fields. For a given string compactification, the precise nature of the supersymmetry breaking is determined by model-dependent calculations. However, at present there are no specific string

---

*Part of this chapter is reprinted with permission from "Supergravity and Superstring Signatures of the One-Parameter Model at LHC" by J. A. Maxin, V. E. Mayes and D. V. Nanopoulos, 2009, Physical Review D, **79**, 066010, Copyright 2009 by the American Physical Society.

compactifications which completely satisfy all theoretical criteria which are desired in such a model. Thus, a model-independent approach is perhaps wiser at the present time. The most studied model of supersymmetry breaking is minimal supergravity (mSUGRA), which arises from adopting the simplest ansatz for the Kähler metric, treating all chiral superfields symmetrically. In this framework, $\mathcal{N} = 1$ supergravity is broken in a hidden sector which is communicated to the observable sector through gravitational interactions. Such models are characterized by the following parameters: a universal scalar mass m_0, a universal gaugino mass $m_{1/2}$, the Higgsino mixing μ-parameter, the Higgs bilinear B-parameter, a universal trilinear coupling A_0, and $\tan\beta$. One then determines the B and $|\mu|$ parameters by the minimization of the Higgs potential triggering REWSB, with the sign of μ remaining undetermined. Thus, we are left with only four parameters. Although, this is one of the most generic frameworks that can be adopted, and many string compactifications typically yield expressions for the soft terms which are even more constrained due to the no-scale structure which emerges naturally in these theories assuming that supersymmetry breaking is dominated by the Kähler moduli and/or dilaton. In particular, in such nSUGRA models, we will generically have $m_0 = m_0(m_{1/2})$ and $A = A(m_{1/2})$. This reduces the number of free parameters compared to mSUGRA down to two, $m_{1/2}$ and $\tan\beta$. In fact, adopting a strict no-scale framework, one can also fix the B-parameter as $B = B(m_{1/2})$, and thus we are led to a *one-parameter* model where all of the soft terms may be fixed in terms of $m_{1/2}$.

If we assume that the supersymmetry breaking is triggered by some of the moduli fields in a given string compactification, namely the dilaton S and the three Kähler moduli T which obtain VEVs $\langle F_S\rangle$ and $\langle F_T\rangle$ respectively, a simple expression for the

scalar masses may be adopted:

$$\tilde{m}_i^2 = m_{3/2}^2(1 + n_i \cos^2\theta), \tag{2.1}$$

with $\tan\theta = \langle F_S \rangle \,/\, \langle F_T \rangle$ and where $m_{3/2}$ is the gravitino mass and n_i are the modular weights of the respective matter fields.

In order to obtain universal scalar masses, which are highly suggested by the required absence of FCNC [31], there are two possible cases which may be considered: (i) setting $\theta = \pi/2$ so that $\langle F_S \rangle >> \langle F_T \rangle$; or (ii) setting all n_i to be the same ($n_i = -1$) and $\theta = 0$ so that $\langle F_T \rangle >> \langle F_S \rangle$ so that all scalar masses vanish at the unification scale. The first of these two cases is referred to as the special *dilaton* scenario,

$$m_0 = \frac{1}{\sqrt{3}} m_{1/2}, \qquad A = -m_{1/2}, \qquad B = \frac{2}{\sqrt{3}} m_{1/2}. \tag{2.2}$$

while the second is referred to as the strict *moduli* scenario,

$$m_0 = 0, \qquad A = 0, \qquad B = 0. \tag{2.3}$$

For many string compactifications, especially those within the free-fermionic class of models in particular those with a flipped $SU(5)$ gauge group [32], the soft-terms will have such a form. Interestingly, soft terms for heterotic M-theory compactifications with moduli dominated supersymmetry breaking take the form [33]

$$\begin{aligned} m_{1/2} &= \tfrac{x}{1+x} m_{3/2} \\ m_0 &= \tfrac{x}{3+x} m_{3/2} \\ A &= -\tfrac{3x}{3+x} m_{3/2} \end{aligned} \tag{2.4}$$

while for dilaton dominated supersymmetry breaking they take the form

$$m_{1/2} = \tfrac{\sqrt{3} m_{3/2}}{1+x} \tag{2.5}$$

$$m_0^2 = m_{3/2}^2 - \frac{3m_{3/2}^2}{(3+x)^2}x(6+x)$$
$$A = -\frac{\sqrt{3}m_{3/2}}{3+x}(3-2x)$$

which reduce to the above moduli and dilaton scenarios in the limit $x \to 0$, where

$$x \propto \frac{(T+\overline{T})}{S+\overline{S}} \tag{2.6}$$

In addition, the so-called large-volume models have been studied extensively [34] [35] in recent years and the generic soft terms for this framework have been calculated in [36]. These models involve Type IIB compactifications where the moduli are stabilized by fluxes and quantum corrections to the Kähler potential generate an exponentially large volume. This exponentially large volume may lower the string scale to an intermediate level which can be in the range $m_s \sim 10^{3-15}$ GeV. In such models, the soft terms can take the form

$$m_0 = \frac{1}{\sqrt{3}}M$$
$$A_0 = -M$$
$$B = -\frac{4}{3}M \tag{2.7}$$

where M is a universal gaugino mass, which are essentially identical to the special dilaton scenario given above. However, this framework is different from our analysis in that the string scale may be lower than what is usually taken for the grand unification scale $\approx 2.1 \times 10^{16}$ GeV. Thus, in this scenario the observed unification of the gauge couplings when extrapolated to high energies is merely coincidental. Of course, this then also affects the running of the soft-masses resulting in different superpartner spectra than what would otherwise be obtained.

In this work, we identify the regions of the supersymmetry parameter space for a generic one-parameter model which are allowed by current experimental constraints

and survey the signatures which may be observable at LHC. We find that in the strict moduli scenario, there are no regions of the parameter space which may satisfy all constraints. However, for the dilaton scenario, there are small regions of the parameter space where all constraints may be satisfied and for which the observed dark matter density may be generated. The model is thus a highly constrained subset of mSUGRA, which allows the model to potentially be predictive. Conversely, if the superpartner spectrum actually observed at LHC lies within the OPM parameter space, then this may provide a strong clue to the underlying theory at high energy scales. Finally, we simulate the different LHC signatures for this model and compare to those for an intersecting $D6$-brane model which possesses many desirable phenomenological characteristics [37]. We find certain signatures may indicate there are distinguishing phenomenological characteristics between these different types of constructions.

B. OPM Low Energy Supersymmetry

A one-parameter model of the above form has been much studied in the past [38, 39, 40], however, the last such analysis was performed some years ago. In the intervening time, the experimental constraints on SUSY models have been updated considerably, especially in regards to the constraints on the dark matter density. In addition, the experimental determination of the top quark mass has become considerably more precise in recent years. Here, we will generate a set of soft terms at the unification scale using the ansatz given in Eqs. 2.2 and Eqs. 2.3 for both the dilaton and moduli scenarios. The soft terms are then input into `MicrOMEGAs 2.0.7` [41] using `SuSpect 2.34` [42] as a front end to evolve the soft terms down to the electroweak scale via the Renormalization Group Equations (RGEs) and then to calculate the corresponding relic neutralino density. We take the top quark mass to be $m_t = 171.4$ GeV [43] and

leave tan β as a free parameter, while μ is determined by the requirement of REWSB. However, we do take $\mu > 0$ as suggested by the results of $g_\mu - 2$ for the muon. The resulting superpartner spectra are filtered according to the following criteria, which we consistently apply throughout this work:

1. The 5-year WMAP data combined with measurements of Type Ia supernovae and baryon acoustic oscillations in the galaxy distribution for the cold dark matter density [4], $0.1109 \leq \Omega_{\chi^\circ} h^2 \leq 0.1177$, where a neutralino LSP is the dominant component of the relic density. We also consider the WMAP 2σ results [3], $0.095 \leq \Omega_{\chi^\circ} h^2 \leq 0.129$. In addition, we look at the SSC model [5], in which a dilution factor of $\mathcal{O}(10)$ is allowed [6], where $\Omega_{\chi^\circ} h^2 \leq 1.1$. For a discussion of the SSC model within the context of mSUGRA, see [7]. We also investigate another case where a neutralino LSP makes up a subdominant component, allowing for the possibility that dark matter could be composed of matter such as axions, cryptons, or other particles. We employ this possibility by removing the lower bound.

2. The experimental limits on the Flavor Changing Neutral Current (FCNC) process, $b \to s\gamma$. The results from the Heavy Flavor Averaging Group (HFAG) [19], in addition to the BABAR, Belle, and CLEO results, are: $Br(b \to s\gamma) = (355 \pm 24^{+9}_{-10} \pm 3) \times 10^{-6}$. There is also a more recent estimate [20] of $Br(b \to s\gamma) = (3.15 \pm 0.23) \times 10^{-4}$. For our analysis, we use the limits $2.86 \times 10^{-4} \leq Br(b \to s\gamma) \leq 4.18 \times 10^{-4}$, where experimental and theoretical errors are added in quadrature.

3. The anomalous magnetic moment of the muon, $g_\mu - 2$. For this analysis we use the 2σ level boundaries, $11 \times 10^{-10} < \Delta a_\mu < 44 \times 10^{-10}$ [21].

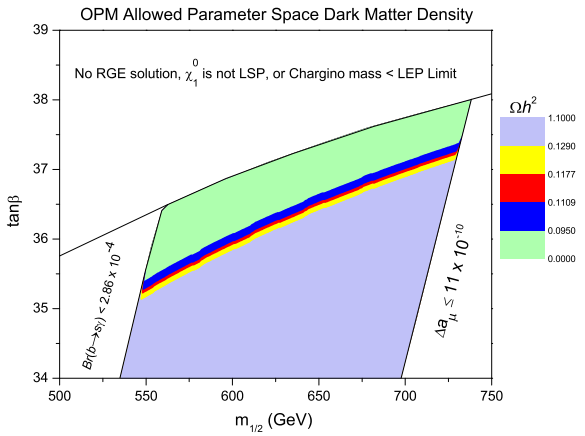

Fig. 1. Parameter space allowed by all constraints for the WMAP constraints. The thin shaded areas constitute the WMAP region. The shaded area below the WMAP region is allowed by all constraints, though $0.129 < \Omega_{\chi^o} h^2 \leq 1.1$. The region on the far right side of the plot is excluded by the $g_\mu - 2$ results. The region on the far left side of the plot is excluded by $Br(b \to s\gamma) < 2.86 \times 10^{-4}$. The remaining area at the top of the plot is excluded for the reasons noted.

4. The process $B_s^0 \to \mu^+\mu^-$ where the decay has a $\tan^6\beta$ dependence. We take the upper bound to be $Br(B_s^0 \to \mu^+\mu^-) < 5.8 \times 10^{-8}$ [22].

5. The LEP limit on the lightest CP-even Higgs boson mass, $m_h \geq 114$ GeV [23].

A scan of the full parameter space is performed for both the strict moduli scenario and the dilaton scenario. The gaugino mass $m_{1/2}$ is varied in increments of 1 GeV in the range $50 - 2000$ GeV while $\tan\beta$ is varied in increments of 0.1 in the range $1 - 60$. For the moduli scenario for $m_{1/2}$, $m_0 = 0$, $A_0 = 0$, and $\tan\beta$ taken as a free parameter, it is found that there are no spectra which satisfy all constraints. This analysis was conducted for the strict no-scale moduli scenario only. However, solutions may potentially be found when non-leading order corrections to the no-scale model are taken into account. For a detailed study concerning these corrections to the no-scale model, see [44]. We conclude that there are no solutions for the moduli

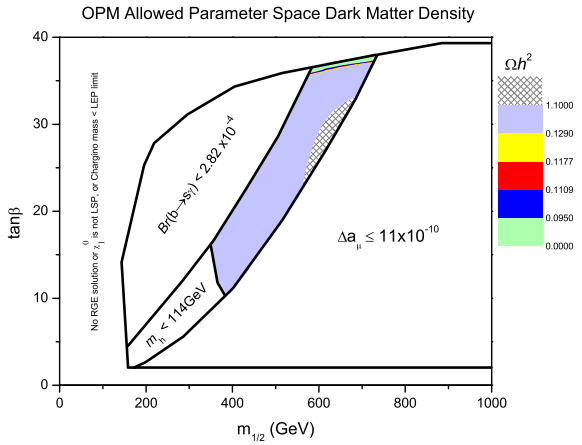

Fig. 2. Parameter space allowed by all constraints for the SSC constraints. The WMAP region is the small thin region at the top. The shaded area below the WMAP region is allowed by all constraints, though $0.129 < \Omega_{\chi^o} h^2 \leq 1.1$. The region excluded by $m_h < 114$ GeV satisfies all other constraints, including $\Omega_{\chi^o} h^2 \leq 1.1$. The cross-hatched region satisfies all constraints, though $\Omega_{\chi^o} h^2 > 1.1$. The remaining areas are excluded for the reasons noted.

scenario unless these corrections are incorporated, and for the present work no further study will be conducted into the strict moduli scenario.

Next, a full scan of the parameter space is performed for the dilaton scenario for $m_{1/2}$, $m_0 = \frac{1}{\sqrt{3}} m_{1/2}$, $A_0 = -m_{1/2}$, and taking $\tan\beta$ as a free parameter. With $m_t = 171.4$ GeV, a small region of the parameter space which satisfies all constraints is found. We exhibit the parameter space which results in a relic density satisfying the WMAP limits in Fig. 1. If the relic neutralino LSP comprises a sub-dominant component of the dark matter, we should not impose the lower bound on the WMAP limits. Thus, the parameter space for the four cases considered are 1) $0.1109 \leq \Omega_{\chi^o} h^2 \leq 0.1177$, 2) $0.095 \leq \Omega_{\chi^o} h^2 \leq 0.129$, 3) $0 \leq \Omega_{\chi^o} h^2 \leq 0.1177$, and 4) $0 \leq \Omega_{\chi^o} h^2 \leq 0.129$. Note that the parameter space shown in Fig. 1 is allowed by all constraints, except those regions noted. Fig. 2 also displays the parameter space

Table I. Allowed ranges of the CP-even Higgs boson mass (in GeV) which satisfy the WMAP and SSC dark matter density limits as well as all other constraints.

$\Omega_{\chi^o}h^2$	m_h (GeV)
$0.1109 \leq \Omega_{\chi^o}h^2 \leq 0.1177$	117.17 - 118.58
$0.095 \leq \Omega_{\chi^o}h^2 \leq 0.129$	117.16 - 118.60
$0 \leq \Omega_{\chi^o}h^2 \leq 0.1177$	116.90 - 118.64
$0 \leq \Omega_{\chi^o}h^2 \leq 0.129$	116.90 - 118.64
$0 \leq \Omega_{\chi^o}h^2 \leq 1.1$	114.00 - 118.64

allowed by all constraints, though the parameter space for the SSC model of the dark matter density is shown in totality.

Imposing all the experimental constraints, we find that the viable WMAP parameter space is in the range $\tan\beta = 35.2$ to $\tan\beta = 38$ as shown in Fig. 1. Extending the dark matter density to the SSC model as shown in Fig. 2, the allowed parameter space expands from $\tan\beta = 10.2$ to $\tan\beta = 38$. We show in Table I the allowed ranges for the CP-even Higgs boson mass satisfying all constraints for each range of $\Omega_{\chi^o}h^2$ within the parameter space. As we see, the range of the Higgs mass is highly constrained in each of the cases. For the superpartner spectra allowed by the constraints, there are only two hierarchal mass patterns of the four lightest sparticles: 1) $\widetilde{\chi}_1^0 < \widetilde{\tau} < \widetilde{e}_R < \widetilde{\chi}_1^{\pm}$, and 2) $\widetilde{\chi}_1^0 < \widetilde{\tau} < \widetilde{e}_R < \widetilde{\nu}_\tau$. The stau is NLSP in each case. A characteristic of this coannihilation region is the nearly degenerate mass of the lightest neutralino and the stau, which is in fact what we find for these spectra in the WMAP region. The LSP in both the WMAP and SSC regions allowed by the constraints is found to be Bino-like.

It has been shown in [45, 46] that it is possible to obtain mass measurements of the supersymmetric particles in the neutralino-stau coannihilation region by utilizing

each final state and parameterizing kinematical observables, such as those described in the previous section, in terms of the SUSY masses. The goal of such an analysis would be to determine the mSUGRA model parameters m_0, $m_{1/2}$, A_0, and $\tan\beta$ since we want to determine the dark matter content and the neutralino-nucleon cross section, while the fifth mSUGRA model parameter, $\mathrm{sign}(\mu)$, is assumed to be positive, since this is preferred by measurements of the $b \to s\gamma$ branching ratio and the muon $g_\mu - 2$. To determine the mSUGRA parameters, we need four kinematical observables which are linearly independent functions of those parameters. The determination of the parameters is then accomplished by inverting four such functional relationships. An analysis of this type was discussed in [47].

The OPM parameter space satisfying all constraints which has been found is a subset of the minimal supergravity (mSUGRA) parameter space, whose collider signals has been the subject of much study over the years. In particular, the allowed parameter space of OPM satisfying the WMAP constraints falls into the coannihilation regions of mSUGRA. However, since this is a very small subset of the mSUGRA parameter space, the allowed superpartner spectra are somewhat constrained, and thus the possible signals of the model which might be observed at LHC are constrained as well. Once there is experimental data from LHC available, one may perform the analysis discussed in the previous paragraph to determine the mSUGRA model parameters. These may then be compared to the above OPM parameter space allowed by constraints. If the experimentally determined mSUGRA parameters happen to coincide with the allowed OPM parameter space, then this may provide an important clue to the structure of the underlying theory at high energy scales. One may also focus on the superpartner spectra of OPM and the resulting experimental signatures which should be observed at LHC if we live in a one-parameter model universe. We give a generic discussion of the experimental signatures of OPM in the next section.

C. Generic Phenomenological Features and Possible Signatures of OPM at LHC

In a one-parameter model universe, predominantly squarks and gluinos will be produced at LHC. To discuss the possible phenomenology of the one-parameter model, we select one spectrum from each of the two regions of the parameter space: WMAP and SSC. The spectra are identified as the WMAP Sparticle Spectrum (WMAP SS), and the SSC Sparticle Spectrum (SSC SS). We can then analyze the probable channels and resulting signatures at LHC, and construct the opposite sign (OS) ditau invariant mass. The anticipated states decaying from the squarks and gluinos involve hadronic jets and tau, so the OS ditau invariant mass may provide some clues leading to discovery at LHC. To examine these probable channels, the cross-sections and branching ratios can then be calculated with `PYTHIA 6.4` [48] and cross-checked with `ISAJET 7.67` [49], using `ISASUGRA` [49] to calculate the sparticle masses. Many analyses have been completed on the entire mSUGRA parameter space, the stau-neutralino coannihilation region in particular. We do not repeat these analyses, but focus on this much more constrained region of the mSUGRA parameter space predicted by the one-parameter model.

1. WMAP Sparticle Spectrum

The WMAP parameter space for OPM is quite constrained by Eqs. 2.2. This defines the one-parameter model as a very constrained subset of mSUGRA. For a detailed analysis of potential LHC signals of mSUGRA in the context of CMS, see [50]. Here we will examine the probable states within only the one-parameter model region of the mSUGRA parameter space. The WMAP SS selected is shown in Table II.

The mass of the gluino is greater than the mass of the squarks, hence the allowed processes with the largest differential cross-sections are $q+q \to \widetilde{q}+\widetilde{q}$ and $q+g \to \widetilde{q}+\widetilde{g}$,

Table II. Low energy supersymmetric particles and their masses (in GeV) for $m_{1/2} = 606$, $m_0 = 349.9$, $A_0 = -606$, $\tan\beta = 36$, $\mu > 0$, $\Omega_{\chi^o} h^2 = 0.1147$.

h^0	H^0	A^0	$H^\pm$	$\widetilde{g}$	$\widetilde{\chi}_1^\pm$	$\widetilde{\chi}_2^\pm$	$\widetilde{\chi}_1^0$	$\widetilde{\chi}_2^0$
117.6	753.9	753.9	758.4	1377	482.9	840.8	254.1	483.0
$\widetilde{\chi}_3^0$	$\widetilde{\chi}_4^0$	$\widetilde{t}_1$	$\widetilde{t}_2$	$\widetilde{u}_R/\widetilde{c}_R$	$\widetilde{u}_L/\widetilde{c}_L$	$\widetilde{b}_1$	$\widetilde{b}_2$	
832.4	840.4	932.6	1169	1251	1294	1109	1174	
$\widetilde{d}_R/\widetilde{s}_R$	$\widetilde{d}_L/\widetilde{s}_L$	$\widetilde{\tau}_1$	$\widetilde{\tau}_2$	$\widetilde{\nu}_\tau$	$\widetilde{e}_R/\widetilde{\mu}_R$	$\widetilde{e}_L/\widetilde{\mu}_L$	$\widetilde{\nu}_e/\widetilde{\nu}_\mu$	*LSP*
1246	1297	263.2	509.3	485.2	416.5	532.8	527.0	*Bino*

where $\widetilde{q} = (\widetilde{q}_L, \widetilde{q}_R)$. The largest cross-section is $q + q \rightarrow \widetilde{q}_R + \widetilde{q}_R$, with $\widetilde{q}_R \rightarrow q\widetilde{\chi}_1^0$ for $\widetilde{q}_R = (\widetilde{u}_R, \widetilde{d}_R, \widetilde{c}_R, \widetilde{s}_R)$. The resulting signature is a high number of 2 jets events plus missing energy. The next largest cross-section is $q + q \rightarrow \widetilde{q}_L + \widetilde{q}_L$, where the branching ratio for $\widetilde{q}_L \rightarrow q\widetilde{\chi}_1^\pm$ is 65% and the branching ratio for $\widetilde{q}_L \rightarrow q\widetilde{\chi}_2^0$ is 33% for $\widetilde{q}_L = (\widetilde{u}_L, \widetilde{d}_L, \widetilde{c}_L, \widetilde{s}_L)$. Therefore, $\widetilde{q}_L$ will decay to either a $\widetilde{\chi}_1^\pm$ or $\widetilde{\chi}_2^0$. The lightest chargino decays to a stau by $\widetilde{\chi}_1^\pm \rightarrow \widetilde{\tau}_1^\pm \nu_\tau$. The second lightest neutralino decays to a stau through $\widetilde{\chi}_2^0 \rightarrow \widetilde{\tau}_1^\mp \tau^\pm$. The probability of either a $\widetilde{\chi}_1^\pm$ or $\widetilde{\chi}_2^0$ decaying to a $\widetilde{\tau}_1$ is essentially the same, and this can be attributed to the nearly degenerate mass between the $\widetilde{\chi}_1^\pm$ and $\widetilde{\chi}_2^0$, as shown in Table II. The stau will always decay to tau and LSP via $\widetilde{\tau}_1^\pm \rightarrow \widetilde{\chi}_1^0 \tau^\pm$. The process $q + q \rightarrow \widetilde{q}_L + \widetilde{q}_R$, which are just combinations of the above, has the next largest cross-section. To summarize the probable cascade decays for $q + q \rightarrow \widetilde{q} + \widetilde{q}$ where $\widetilde{q} = (\widetilde{u}, \widetilde{d}, \widetilde{c}, \widetilde{s})$, they are:

- $\widetilde{q}_R \rightarrow q\widetilde{\chi}_1^0$
- $\widetilde{q}_L \rightarrow q\widetilde{\chi}_1^\pm \rightarrow q\widetilde{\tau}_1^\pm \nu_\tau \rightarrow q\nu_\tau \tau^\pm \widetilde{\chi}_1^0$
- $\widetilde{q}_L \rightarrow q\widetilde{\chi}_2^0 \rightarrow q\widetilde{\tau}_1^\mp \tau^\pm \rightarrow q\tau^\pm \tau^\mp \widetilde{\chi}_1^0$

As these processes show, combinations of these three channels will result in one tau, two tau, and three tau events with two hadronic jets, plus missing energy from

the stable $\widetilde{\chi}_1^0$ LSP and tau neutrinos. These tau events will be well in excess of the observable limit as calculated in the next section, presenting the opportunity for clear distinction between the one-parameter model region of the mSUGRA parameter space and the background. Now we examine gluino decays. After the production of exclusively squarks, the next largest cross-sections are $q + g \rightarrow \widetilde{q} + \widetilde{g}$, where $\widetilde{q} = (\widetilde{q}_L, \widetilde{q}_R)$. The heavier mass of the gluinos over the squarks in the one-parameter model requires the gluinos decay to squarks. The stop and sbottom are the lightest squarks, so these decays will be from gluinos to bottom and top squarks 73% of the time. The remaining 27% of the time the gluinos will decay to up, down, charm, and strange squarks. The branching ratios for the decay $\widetilde{g} \rightarrow \widetilde{b}_1\bar{b}$ is 20% and $\widetilde{g} \rightarrow \widetilde{b}_2\bar{b}$ is 13%, whereas $\widetilde{g} \rightarrow \widetilde{t}_1\bar{t}$ is 28% and $\widetilde{g} \rightarrow \widetilde{t}_2\bar{t}$ is 12%. Therefore, the $\widetilde{t}_1$ and $\widetilde{b}_1$ channels are most favored since $\widetilde{t}_1$ and $\widetilde{b}_1$ are lighter than $\widetilde{t}_2$ and $\widetilde{b}_2$. The top squark will decay via $\widetilde{t}_1 \rightarrow t\widetilde{\chi}_1^0$ 41% of the time, and $\widetilde{t}_1 \rightarrow b\widetilde{\chi}_1^{\pm}$ 34% of the time. The top quark decays to a b quark plus either jets or leptons through a $W^{\pm}$ boson. The bottom squark decays via $\widetilde{b}_1 \rightarrow t\widetilde{\chi}_1^-$ 41% of the time. To summarize the most probable results of the gluino cascade decays are

- $\widetilde{g} \rightarrow \widetilde{t}_1\bar{t} \rightarrow t\bar{t}\widetilde{\chi}_1^0$
- $\widetilde{g} \rightarrow \widetilde{b}_1\bar{b} \rightarrow \bar{b}t\widetilde{\chi}_1^- \rightarrow \bar{b}t\widetilde{\tau}_1^-\nu_\tau \rightarrow \bar{b}t\tau^-\nu_\tau\widetilde{\chi}_1^0$
- $\widetilde{g} \rightarrow \widetilde{q}_R\bar{q} \rightarrow q\bar{q}\widetilde{\chi}_1^0$

The combination of one of these gluino decays with one of the squark decays will produce one tau, two tau, and three tau events with two or more jets, plus missing energy. It is significant to notice that each $\widetilde{t}_1$ and $\widetilde{b}_1$ will produce a b-jet. Each stop and sbottom is accompanied by a top or bottom quark. Each top quark also produces a b-jet, so all b-jets will be produced in pairs, most in pairs of $b\bar{b}$. To emulate

the expected LHC experience, we use the code PGS4 [51] to simulate events, which parameterizes b-tagging efficiency as a function of jet P_T. For our study here, we use a post-trigger level jet P_T cut of 60 GeV. For jet $P_T > 60$ GeV, the b-tagging efficiency in PGS4 varies from $\sim$ 37% to $\sim$ 45% [52]. Therefore, the number of events will decline for sequentially higher number of b-jets, and there will be more than three times as many one b-jet events as two b-jet events. For this reason, we will use the percentage of one b-jet events to understand the phenomenology of the one-parameter model, even though no single b-jets are produced. Examining the processes listed above, only the gluino decays result in a lepton as a result of the $W^{\pm}$ boson from the top quark, where $l = (e, \mu, \tau)$, therefore the number of tau events will encompass the majority of overall lepton events, in contrast to the low percentage of tau events per overall lepton events within the background. Namely, the large number of tau events in excess of the background are the most likely one-parameter model fingerprint. Hence, we conclude the most constructive analysis of the one-parameter model phenomenology is to study these specific collider signatures:

- 1 tau lepton, 1 tau and $\geq$1 b-jet, 2 tau leptons, 1 lepton, 2 leptons and $\geq$2 jets, 2 jets, 3 jets, 1 b-jet

In fact, we will use these signatures in the next section in our effort to compare the phenomenology of the one-parameter model with a different string vacua, that is, an intersecting $D6$-brane model. To conclude the analysis of the WMAP SS, we construct the $\tau^+\tau^-$ invariant mass for this WMAP spectrum in Fig. 3.

2. SSC Sparticle Spectrum

One representative spectrum was selected from the SSC region of the parameter space, and the masses are shown in Table III. The probable states do not vary from those

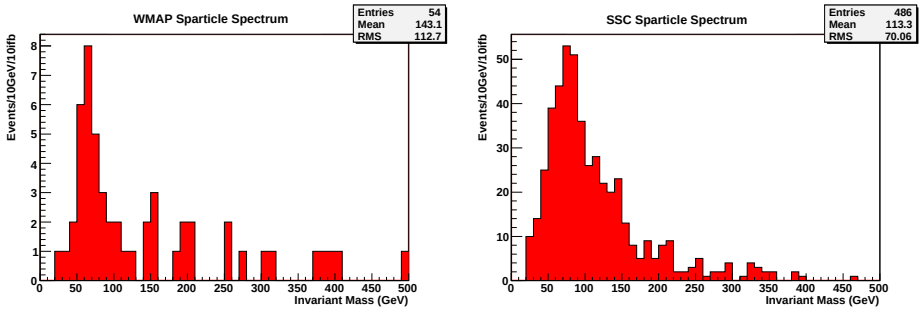

Fig. 3. $\tau^+\tau^-$ invariant mass of the WMAP sparticle spectrum (in GeV), $m_{1/2} = 606$, $m_0 = 349.9$, $A_0 = -606$, $\tan\beta = 36$, $\mu > 0$, $\Omega_{\chi^o}h^2 = 0.1147$, and the SSC sparticle spectrum (in GeV), $m_{1/2} = 475$, $m_0 = 274.2$, $A_0 = -475$, $\tan\beta = 18$, $\mu > 0$, $\Omega_{\chi^o}h^2 = 0.8496$.

Table III. Low energy supersymmetric particles and their masses (in GeV) for $m_{1/2} = 475$, $m_0 = 274.2$, $A_0 = -475$, $\tan\beta = 18$, $\mu > 0$, $\Omega_{\chi^o}h^2 = 0.8496$.

h^0	H^0	A^0	$H^\pm$	$\widetilde{g}$	$\widetilde{\chi}_1^\pm$	$\widetilde{\chi}_2^\pm$	$\widetilde{\chi}_1^0$	$\widetilde{\chi}_2^0$
116.1	746.5	746.5	751.1	1100	372.6	689.3	196.0	372.6
$\widetilde{\chi}_3^0$	$\widetilde{\chi}_4^0$	$\widetilde{t}_1$	$\widetilde{t}_2$	$\widetilde{u}_R/\widetilde{c}_R$	$\widetilde{u}_L/\widetilde{c}_L$	$\widetilde{b}_1$	$\widetilde{b}_2$	
679.1	689.0	733.4	973.4	999.7	1033	922.5	979.8	
$\widetilde{d}_R/\widetilde{s}_R$	$\widetilde{d}_L/\widetilde{s}_L$	$\widetilde{\tau}_1$	$\widetilde{\tau}_2$	$\widetilde{\nu}_\tau$	$\widetilde{e}_R/\widetilde{\mu}_R$	$\widetilde{e}_L/\widetilde{\mu}_L$	$\widetilde{\nu}_e/\widetilde{\nu}_\mu$	*LSP*
996.6	1036	294.3	418.4	403.4	327.7	419.6	412.2	*Bino*

of the WMAP region, though the branching ratios for the chargino and neutralino decays do vary. The processes with the largest cross-sections are the same as with the WMAP SS, that is, the production of squarks and then the production of squarks and gluinos. The only real difference involves the decay of charginos and neutralinos. The branching ratio for $\widetilde{\chi}_1^\pm \rightarrow \widetilde{\tau}_1^\pm\nu_\tau$ is 70%, as opposed to 95% for the WMAP SS. The masses of $\widetilde{\chi}_1^\pm$ and $\widetilde{\chi}_2^0$ are still nearly degenerate for the SSC SS spectrum, however, the masss difference between the $\widetilde{\chi}_1^\pm$ or $\widetilde{\chi}_2^0$ and the $\widetilde{\tau}_1$ is about 78 GeV as opposed to 220 GeV for the WMAP SS. This accounts for the smaller branching ratio for the SSC SS. For the same reason, the decay $\widetilde{\chi}_2^0 \rightarrow \widetilde{\tau}_1^\mp\tau^\pm$ is now a little less likely with a branching ratio of 72%, as opposed to 96% for the WMAP SS. The other non-negligible decay

process for the chargino is $\widetilde{\chi}_1^{\pm} \rightarrow W^{\pm}\widetilde{\chi}_1^0$, where the branching ratio for this is 29% since the SSC SS has a lighter LSP than the WMAP SS. This process was negligible for the WMAP SS. The production of a higgs boson is now a little more probable at 24% via $\widetilde{\chi}_2^0 \rightarrow h_0\widetilde{\chi}_1^0$, whereas WMAP SS higgs production through χ_2^0 was negligible. The branching ratios for the bottom and top squark decays are little changed, hence, the most probable processes remain the same as those for the WMAP SS. This is also true for the gluinos as well. Therefore, the signatures to study for the SSC are the same as those listed for WMAP. Fig. 3 plots the OS ditau invariant mass for the SSC SS, in addition to the WMAP SS invariant mass. The peak occurs about 10 GeV higher for the SSC SS, however, the main distinction is the number of events per 10 GeV per 10 fb^{-1} of LHC data. The lighter sparticle spectrum of the SSC SS affords higher sparticle production than the WMAP SS for the same integrated luminosity.

D. Signatures of OPM vs. Non-universality at LHC

In this section, we discuss the LHC signatures of the one-parameter model and compare them to those of an intersecting D6-brane model non-universal soft terms. See [53] for a similar analysis. To simulate events for different regions of the allowed parameter space, the superpartner mass spectra are first calculated using `SuSpect 2.34`. Then production cross-sections and branching ratios are calculated using `PYTHIA 6.4`. The simulated events are then generated using the code PGS4 [51]. A SUSY Le Houches Accord (SLHA) [54] file is output by `SuSpect 2.34` and this SLHA file is then called by `PYTHIA 6.4` via PGS4. In the `PYTHIA 6.4` card file, MSEL = 39 is used to generate 91 Minimal Symmetric Standard Model (MSSM) $2 \rightarrow 2$ production processes, excluding only single Higgs production. The default configuration of the LHC Detector Card and the Level 1 (L1) trigger are used in

PGS4. The L1 trigger level cuts are close to the actual values used by the Compact Muon Solenoid Detector (CMS) experiment. A table of the L1 trigger level cuts can be found here [55]. A total integrated luminosity of 10 fb^{-1} of data was simulated for all signatures. This corresponds to approximately the first few years of data collection at LHC. At this point, post-trigger level cuts over and above the L1 trigger level cuts can be applied to streamline the data even further. To apply post-trigger level cuts and count collider observables, the program Chameleon Root (ChRoot) [56] was used. The post-trigger level cuts used for the one-parameter model are:

- $P_T > 60$ GeV and $|\eta| < 3$ for jets
- $P_T > 20$ GeV and $|\eta| < 2.4$ for photons and leptons
- $P_T^{miss} > 215$ GeV for missing transverse momentum.

These same post-trigger level cuts are also applied to the Standard Model (SM) background. Constructing an estimate of the SM background is certainly nontrivial. The technical difficulty involves the number of background events. The number of background events can be six orders of magnitude larger than the signal, so most SM events must be discarded in the interest of compute time. Another major issue concerns simulating the largest component of the SM background, QCD physics. The simulation of W-bosons, quarks, and gluons is problematic. In the interest of reducing the compute time as much as possible, we use the SM background sample on the LHC Olympics website [57]. This background sample was used for the LHC Olympics and contains 5 fb^{-1} of LHC SM background data. We utilize this sample to formulate an estimate of the SM background for an integrated luminosity of 10 fb^{-1} of detector data. This SM background sample contains dijets, $t\bar{t}$, and W/Z+jets processes. To determine if a signal is observable above the SM background, an inclusive count of the

individual signatures in the signal is compared to a count of the individual signatures in the background. In order for a signature to be observable above the background, the following statistical requirements must be satisfied [58]:

$$\frac{S}{\sqrt{B}} > 4, \qquad\qquad S > 5$$

where S is the number of signal events and B is the number of background events that survive the trigger level and post-trigger level cuts. An estimate of the observable limit due to the SM background can be computed and compared to the MSSM production process number of events for the signature in order to determine whether a particular signature is observable above the background after all cuts have been applied. In our analysis, the signal is composed of SUSY signatures involving leptons (e, μ, and τ), jets, and b-tagged jets.

Much of the older work toward constructing semi-realistic string vacua was done in the context of heterotic strings. In particular, many of the most phenomenologically interesting models were those constructed within the free-fermionic formulation [32], and it is really from these types of models that the one-parameter model was first defined [38, 39, 40]. As we have mentioned, the same basic structure of the one-parameter model also arises in the context of heterotic M-theory constructions as well as Type IIB orientifold flux compactifications. Besides these types of string vacua, there are also recent constructions involving Type IIA compactifications involving $D6$-branes intersecting at angles. Such models have been the subject of much study in recent years, and we refer the reader to [59, 60] for recent reviews. The soft terms for intersecting $D6$-branes are in general non-universal [61], in contrast in the one-parameter model as well as the standard framework, mSUGRA. Thus, it is an interesting question whether or not it is phenomenologically possible to distinguish between these two different types of string compactifications by what is observed at

LHC.

In ref. [37] an explicit example of a supersymmetric intersecting $D6$-brane model in Type IIA string theory was constructed which possesses many desirable phenomenological properties. In particular, the model has three generations of SM fermions and also exhibits automatic gauge coupling unification at tree-level. In addition, it is possible to obtain correct masses and mixings for both up and down-type quarks as well as the tau lepton. The soft supersymmetry breaking terms were also calculated for this model, and it was shown that there are regions within the parameter space which may generate the observed dark matter density and superpartner spectra satisfying all presently known constraints. Given the desirable phenomenology of this model, it provides a suitable candidate with which to compare the one-parameter model. In particular, the question that we would like to address is if there are distinguishing characteristics in the collider signatures between this class of string vacua constructed with intersecting $D6$-branes in Type IIA and other string constructions mentioned earlier having soft terms similar to OPM.

As discussed in the previous section, there are signatures at LHC that could provide distinguishing characteristics of the one-parameter model. For the present, we want to investigate if these signatures differ between the one-parameter model and the intersecting $D6$-brane model. In Fig. 4 we plot two of these collider signatures against each other for both the one-parameter model and the intersecting $D6$-brane model. For each of the cases shown, there seems to be a clear separation between the one-parameter model and the intersecting $D6$-brane model. All spectra simulated in these figures from both models are within the WMAP region of the allowed parameter space. Namely, thirty-one spectra from the one-parameter model and thirty-five spectra from the intersecting $D6$-brane model were simulated in the event generator. Table IV lists the different patterns of mass hierarchies for the one-parameter

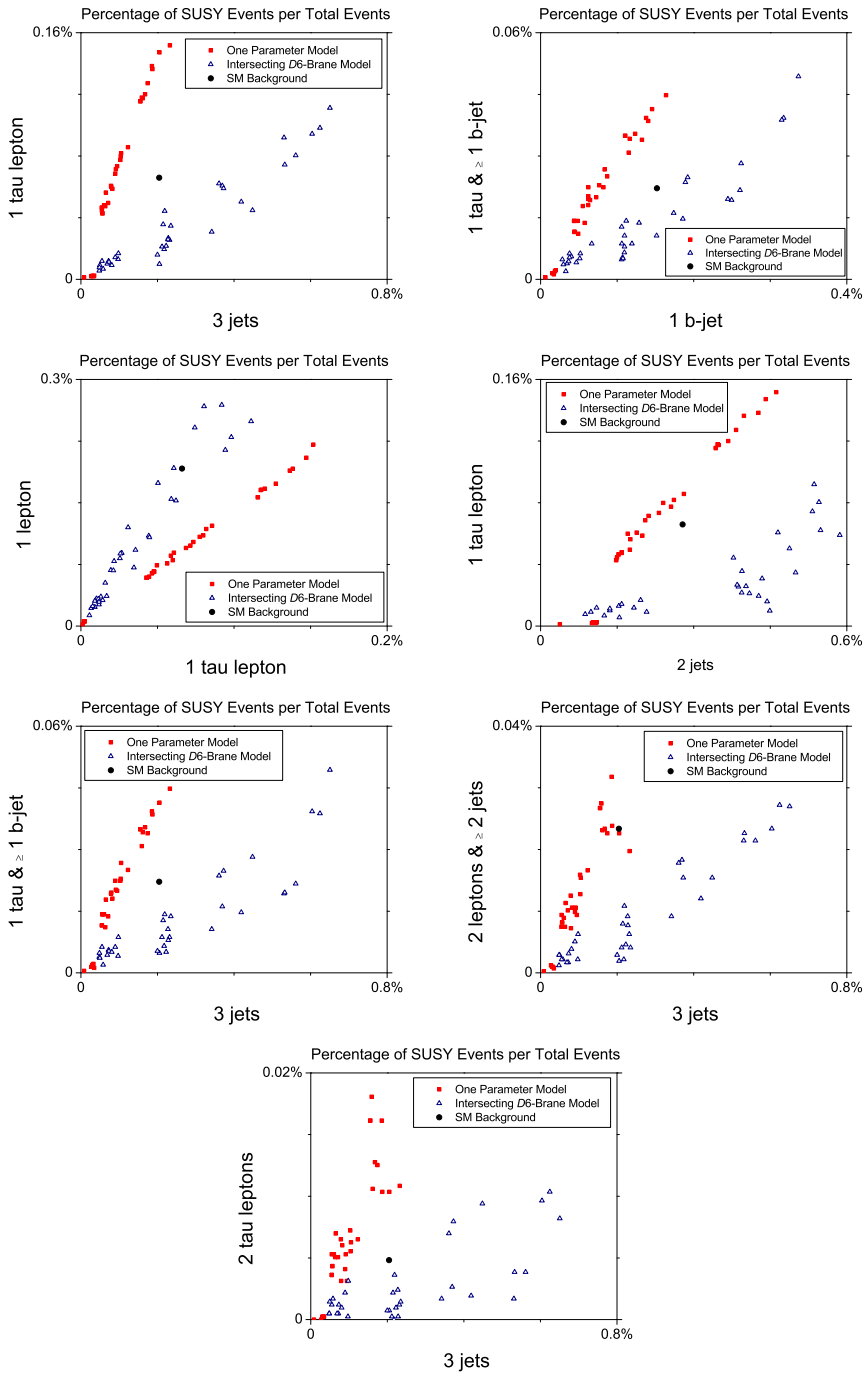

Fig. 4. Percentage of lepton vs. jet and lepton vs. lepton events at LHC for both the intersecting $D6$-brane model and the one-parameter model. The round marker indicates the observable limit due to the Standard Model background. Total events = signal + background.

model parameter space and the intersecting $D6$-brane model. The mass patterns of the thirty-five superpartner spectra for the intersecting $D6$-brane model simulated in the event generator are the *ID6BraneP1* chargino pattern. This is in contrast to the two different stau patterns of the one-parameter model, *OPMP1* and *OPMP2*. The thirty-one one-parameter model spectra simulated in the event generator were a combination of both the *OPMP1* and *OPMP2* stau mass patterns. The patterns in these charts corroborate the details given in the previous section that the number of tau events as a percentage of overall lepton events for the one-parameter model will be high. In fact, the percentage of tau events is much higher in the one-parameter model than in the intersecting $D6$-brane model. We will perform a complete phenomenological analysis of the intersecting $D6$-brane model in the future, but suffice it to say that by examining the mass pattern for *ID6BraneP1* in Table IV, it is evident that the decay of the $\widetilde{\chi}_1^{\pm}$ or $\widetilde{\chi}_2^0$ to a $\widetilde{\tau}_1$ is no longer present due to the $\widetilde{\tau}_1$ now being heavier than the $\widetilde{\chi}_1^{\pm}$ and $\widetilde{\chi}_2^0$. The elimination of this channel alone will reduce the production of tau, as the charts illustrate. We defer a more in-depth study of the additional intersecting $D6$-brane mass patterns in Table IV versus the one-parameter model for future work.

E. B-parameter

For modulus-dominated supersymmetry breaking, we generically have $m_0 = m_0(m_{1/2})$ and $A = A(m_{1/2})$. This reduces the number of free parameters compared to mSUGRA down to two, $m_{1/2}$ and $\tan\beta$. In fact, adopting a strict no-scale framework, one can also fix the B-parameter as $B = B(m_{1/2})$, and thus we are led to a *one-parameter* model where all of the soft terms may be fixed in terms of $m_{1/2}$. However, for this framework to be consistent, the value of $\tan\beta$ at the electroweak scale should be

Table IV. Mass patterns of spectra allowed by all constraints for the one-parameter model (OPM) and the intersecting $D6$-brane model (IBM).

Model	Pattern No.	Pattern Type	Mass Pattern
OPM	*OPMP1*	Stau	$\widetilde{\chi}_1^0 < \widetilde{\tau} < \widetilde{e}_R < \widetilde{\chi}_1^\pm$
OPM	*OPMP2*	Stau	$\widetilde{\chi}_1^0 < \widetilde{\tau} < \widetilde{e}_R < \widetilde{\nu}_\tau$
IBM	*ID6BraneP1*	Chargino	$\widetilde{\chi}_1^0 < \widetilde{\chi}_1^\pm < \widetilde{\chi}_2^0 < \widetilde{\tau}$
IBM	*ID6BraneP2*	Chargino	$\widetilde{\chi}_1^0 < \widetilde{\chi}_1^\pm < \widetilde{\tau} < \widetilde{\chi}_2^0$
IBM	*ID6BraneP3*	Chargino	$\widetilde{\chi}_1^0 < \widetilde{\chi}_1^\pm < \widetilde{\tau} < \widetilde{e}_R$
IBM	*ID6BraneP4*	Stau	$\widetilde{\chi}_1^0 < \widetilde{\tau} < \widetilde{\chi}_1^\pm < \widetilde{\chi}_2^0$
IBM	*ID6BraneP5*	Stau	$\widetilde{\chi}_1^0 < \widetilde{\tau} < \widetilde{e}_R < \widetilde{\chi}_1^\pm$

consistent with B at the string scale.

In the previous sections, we studied a generic one-parameter model and found its viable parameter space [62]. However, we did not require that $\tan\beta$ obtained at the electroweak scale be consistent with the value of $B = B(m_{1/2})$ defined at the GUT scale. Now, we shall impose this constraint for a generic one-parameter model and find that there is no viable supersymmetry parameter space, assuming the standard RGE running between the electroweak scale and the GUT scale. Furthermore, we find the same result for M-theory and Type IIB flux compactifications. In addition, we consider different modular weights for some of the chiral fields, again with negative results. We conclude that modulus-dominated supersymmetry breaking is not viable, in the case of a standard RGE running of the soft terms starting from the GUT scale.

As can be seen for these different string compactifications, the soft terms can generically be of the form

$$m_0 = c_1 m_{1/2},$$

$$A_0 = c_2 m_{1/2},$$
$$B = c_3 m_{1/2}, \tag{2.8}$$

where c_1, c_2, and c_3 are constants. In addition, we will take the string scale to be $M_{GUT} = 2 \times 10^{16}$ GeV. However, we should note that the string scale at which the soft-terms are defined could be different from the conventional GUT scale. In particular, we can see for the case of the M-theory compactifications, the unification scale can be higher than the GUT scale, while for the large-volume Type IIB flux compactifications, the string scale could be substantially lower.

F. Imposing the B Constraint

As briefly mentioned previously in this chapter, the value of the μ parameter and $\tan\beta$ are determined at the electroweak scale by imposing the conditions

$$\mu^2 = \frac{-m_{H_u}^2 \tan^2\beta + m_{H_d}^2}{\tan^\beta - 1} - \frac{1}{2} M_Z^2, \tag{2.9}$$

and

$$\mu B = \frac{1}{2} \sin 2\beta (m_{H_d}^2 + m_{H_u}^2 + 2\mu^2), \tag{2.10}$$

which follow from the minimization of the Higgs potential triggering REWSB. From these equations, one can calculate the value of the B-parameter at the electroweak scale. In order for this to be a true one-parameter model, B at the electroweak scale should be consistent with the ansatz $B = B(m_{1/2})$ at the GUT scale.

The usual procedure to find the viable parameter space is to calculate the sparticle masses using the parameters m_0, $m_{1/2}$, A_0, $sgn(\mu)$, and $\tan\beta$, and plot m_0 *vs.* $m_{1/2}$ for a specific $\tan\beta$, and further scan the entire $\tan\beta$ space for solutions that satisfy the current experimental constraints and corresponding relic neutralino density. In particular, such an analysis was performed for a generic one-parameter model in [62].

However, the consistency constraint between the B-parameter at the electroweak scale and the GUT scale has not been imposed in this analysis. For the present work, we perform a scan of the parameter space, including tanβ, and filter the results through the latest experimental constraints and dark matter density, and in addition, compare the allowed parameter space with the value of the B-parameter at M_{High}. For the present work, we will identify M_{High} with M_{GUT}. This determines whether the allowed parameter space calculated from tanβ can also satisfy the constraint on the B-parameter at the unification scale (see [63] for a similar study in the case of F-theory compactifications).

To determine the B-parameter at $M_{High} = M_{GUT}$, B is determined at m_Z from Eqns. (2.9) and (2.10). Then it is run up to the unification scale to compute the boundary condition for B. A sufficient number of iterations between m_Z and m_{GUT} are calculated until stable results are achieved. The value for B at the GUT scale we use is at the last iteration before the results become stable. To accomplish this, we modify the `SuSpect 2.34` code to output the B-parameter value from the RGE loop during this final iteration. We capture the B-parameter through this method for all sets of the soft-supersymmetry breaking terms that we calculated the experimentally allowed parameter space. Once B is computed for all points, we compare this value of B to the theoretical prediction for B at the unification scale for each model we consider in a plot of the ratio of B to the gaugino mass versus tanβ. The only points that satisfy the B constraint are those points on the B-parameter curves that intersect with the horizontal lines representing the theoretical prediction. Additionally, it is also necessary for these points of intersection between the B curves and predictions to lie within the range of points within the experimentally allowed parameter space. These points just described will satisfy not just the aforementioned five experimental constraints, but also the constraint on the B-parameter at the unification

scale. However, as we will show here, it is very difficult to satisfy all these constraints simultaneously for a model with universal soft-supersymmetry breaking parameters.

We compute the B-parameter at the GUT scale here for two models: a generic one-parameter model [38, 39, 40, 62] and an M-Theory model [33]. We find that for the models with a predicted B-parameter at the GUT scale, namely the minimal one-parameter model and the M-Theory model without corrections, i.e. $x = 0$, contrary to the solutions discovered when only considering the experimental constraints, there are no solutions when the B-parameter constraint is taken into account. In light of this, we shall vary the moduli for the one-parameter model to investigate whether some solutions can be found that satisfy the B-parameter constraint, in addition to only satisfying the experimental constraints. It is also necessary to determine whether solutions exist for the M-Theory model when $x \neq 0$ that can satisfy the B-parameter constraint.

For the one-parameter model, we begin with the minimal model in the special dilaton scenario with the soft terms of the form

$$m_0 = \frac{1}{\sqrt{3}} m_{1/2}, \qquad A = -m_{1/2}, \qquad B = -\frac{2}{\sqrt{3}} m_{1/2}. \tag{2.11}$$

and construct a method of varying the modular weights. To accomplish this, we modify the expressions above and introduce three new parameters ξ, δ, and η that will allow us to investigate more general cases:

$$m_0 = \frac{\xi}{\sqrt{3}} m_{1/2}, \qquad A = -\delta m_{1/2}, \qquad B = -\frac{\eta}{\sqrt{3}} m_{1/2}. \tag{2.12}$$

Using these expressions, the minimal one-parameter model is the case $(\xi, \delta) = (1, 1)$. We now let $\xi = \frac{1}{2}, 1, \frac{3}{2}, 2$ and $\delta = \frac{1}{2}, 1, \frac{3}{2}, 2$, which will give us 16 different cases to examine. The 16 cases shall be divided up into four data sets such that each

data set will be plotted independently. Each data set will have constant ξ, and thus constant m_0, while δ is varied, and hence A is varied. Therefore, each of the four plots will contain four sets of curves, where each set of curves pertains to one (ξ, δ). The gaugino mass is incremented from 100 GeV to 1000 GeV in steps of 100 GeV, whereas tanβ is varied in increments of one from 2 to 60. From these specifications, a list of soft supersymmetry breaking terms is generated and the B-parameter at the GUT scale is calculated for each set of soft terms. As shown in Fig. 5, there are solutions to the one-parameter model when only the experimental constraints are considered, though when the B-parameter constraint is applied, the experimentally allowed parameter space is nullified. There are no intersections between the B-parameter curves and the horizontal lines representing the predictions for the B-parameter. Note that η for the three predictions are

$$\eta = 2 \quad (heterotic)$$

$$\eta = \tfrac{4}{\sqrt{3}} \quad (TypeIIB)$$

$$\eta = 1 + \sqrt{3} \quad (M - Theory)$$

To further ensure that we have examined all possibilities for the minimal one-parameter model, we computed an additional case with an independent modular weight for the Higgs scalars at the unification scale. Our motivation for attempting this is that since the Higgs typically come from a different sector, the dependence on the Kahler moduli should be different. While keeping $(\xi, \delta) = (1, 1)$, the modular weight on the Higgs scalar was varied, nonetheless, there was no shifting of the B-parameter curves and only a slight change in the number of points allowed by the experimental constraints. Lastly, we varied the stop mass at the unification scale for the minimal one-parameter model case $(\xi, \delta) = (1, 1)$ in an attempt to find solutions allowed by the experimental constraints that can also meet the B-parameter

constraint, however there were no solutions in this case either. Therefore, for the minimal one-parameter model parameterizations, the B-parameter constraint at the scale $M_{High} = M_{GUT}$ cannot be satisfied.

We now look more closely at an M-Theory model by varying the unknown parameter x, and due to restrictions on the gauge coupling, seek solutions only for $0 \leq x \leq 1$. The angle θ in the expressions in [33] can also represent an unknown parameter, but we choose to let it remain constant for our study here and only vary the parameter x. The M-Theory expressions are given in terms of the gravitino mass $m_{3/2}$, so first the relations for the soft terms must be solved in terms of $m_{1/2}$, and these are

$$m_0 = (1+x)\sqrt{\tfrac{1}{3} - \tfrac{x(6+x)}{(3+x)^2}}\, m_{1/2}$$

$$A = -\tfrac{(3-2x)(1+x)}{(3+x)} m_{1/2}$$

$$B = -\tfrac{[3+3\sqrt{3}-(\sqrt{3}-1)x](1+x)}{\sqrt{3}(3+x)} m_{1/2}$$

We scan for real solutions that give $m_0 > 0$, $A < 0$, and $B < 0$, and find these solutions only exist for $0 \leq x \leq 0.6742$. The case $x = 0$ is shown in Fig. 5, so we run the three additional cases $x = 0.1, 0.3, 0.5$ for the same increments of $m_{1/2}$ and tanβ as the one-parameter model, and compute the allowed parameter space from the experimental constraints. Again, even though there are points allowed within the parameter space when only considering the experimental constraints, none of these allowed points can satisfy the B-parameter constraint for $0 \leq x \leq 0.6742$. This is clearly shown in Fig. 6 where the horizontal line representing the prediction for the B-parameter at the GUT scale does not intersect the B-parameter curves in any of the three sample cases. In fact, as the unknown variable x increases toward the upper

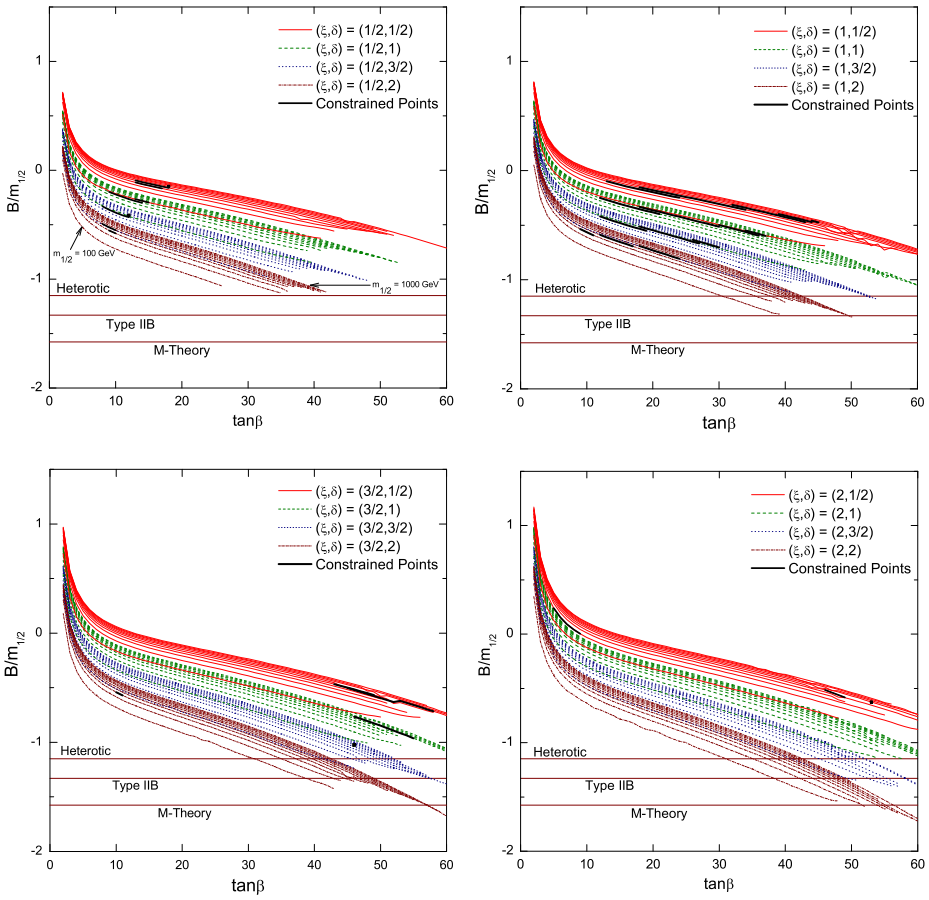

Fig. 5. B/$m_{1/2}$ vs. tanβ at the GUT scale for the one-parameter model. Each plot contains four sets of ten curves, each set with a different (ξ, δ). The ten curves are for $m_{1/2}$ = 100, 200,..., 900, 1000 GeV, where the lowermost curve in each set is $m_{1/2}$ = 100 GeV and the uppermost curve in each set is $m_{1/2}$ = 1000 GeV. The three horizontal lines represent the predictions for B at the GUT scale. The segments of the curves highlighted in thick black represent those points in the parameter space which are experimentally allowed. The minimal one-parameter model and the M-Theory model with $x = 0$ is the case $(\xi, \delta) = (1, 1)$. In these plots, all the allowed points highlighted in black satisfy the relic neutralino density in the SSC scenario. Those points satisfying only the WMAP relic density are not highlighted. As the plots show, the points experimentally allowed do not intersect the predictions for B, hence, the B-parameter constraint cannot be satisfied by the models displayed in this Figure.

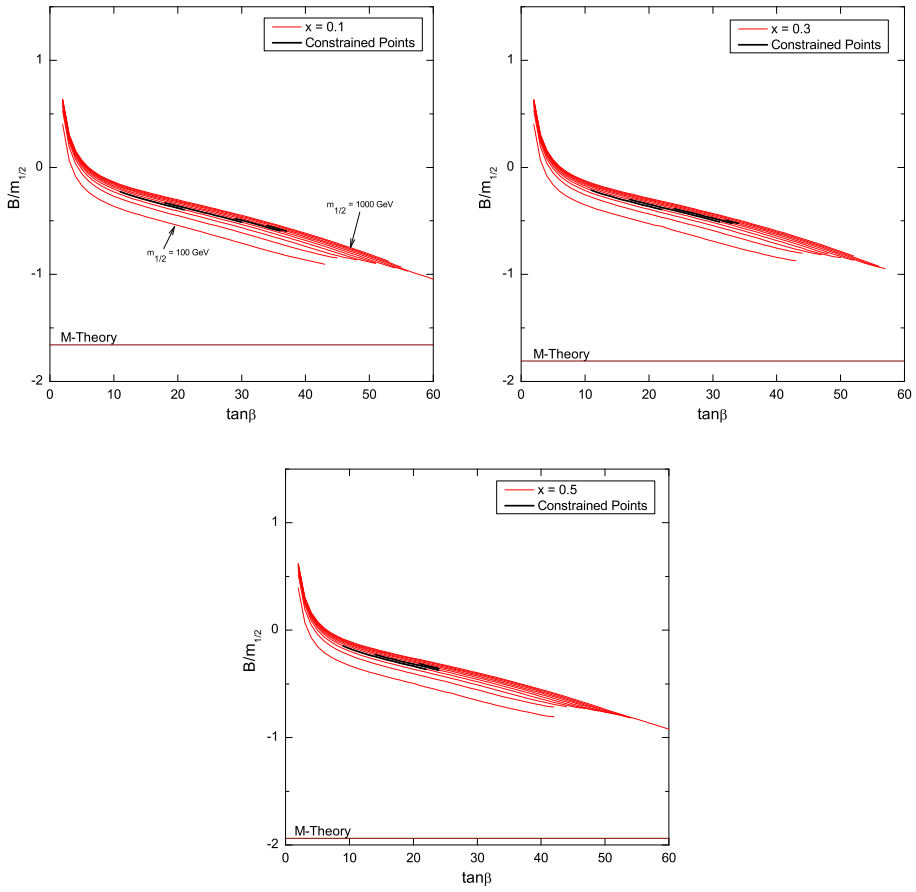

Fig. 6. B/$m_{1/2}$ vs. tanβ at the GUT scale for an M-Theory model. Each plot contains a set of curves for a different x. The ten curves in each plot are for $m_{1/2} = 100$, 200,..., 900, 1000 GeV, where the lowermost curve in each plot is $m_{1/2} = 100$ GeV and the uppermost curve in each plot is $m_{1/2} = 1000$ GeV. The horizontal lines represent the predictions for B at the GUT scale. The segments of the curves highlighted in thick black represent those points in the parameter space which are experimentally allowed. In these plots, all the allowed points highlighted in black satisfy the relic neutralino density in the SSC scenario. Those points satisfying only the WMAP relic density are not highlighted. As the plots show, the points experimentally allowed do not intersect the predictions for B, hence, the B-parameter constraint cannot be satisfied by the model displayed in this Figure.

end of its range, the discrepancy becomes larger. Here again, as in the one-parameter model, the M-Theory model cannot produce any viably allowed parameter space that satisfies both the experimental constraints and the B-parameter constraint.

CHAPTER III

INTERSECTING $D6$-BRANE MODEL*

A. The Intersecting $D6$-brane Model

The main goal of string phenomenology is to make contact between string theory and the real world. In particular, this involves searching for a specific string vacuum which reproduces the Standard Model (SM) in complete detail. This is not an easy task. The SM has an intricate structure, with three-generations of chiral fermions which transform as bifundamental representations of $SU(3)_C \times SU(2)_L \times U(1)_Y$. In addition to the fact that the SM fermions are replicated into three distinct families, the families exhibit a pattern of mass hierarchies and mixings. Although there have been many models which can reproduce the gross features of the SM, there are generally problems either with extra exotic particles or an inability to generate fermion mass hierarchies and mixings.

Interestingly, the so-called intersecting $D6$-brane models where the chiral fermions arise at the intersections between $D6$ branes (Type IIA) in the internal space [64] have provided an exciting approach toward constructing semi-realistic string vacua (for reviews, see [59, 60]). In particular, intersecting D-brane models may naturally generate the SM fermion mass hierarchies and mixings, as well as an explanation for the replication of chirality. Indeed, such models provide promising setups which may accommodate semi-realistic features of low-energy physics. In short, $D6$-branes (in

*Part of this chapter is reprinted with permission from "Stringy WIMP Detection and Annihilation" by J. A. Maxin, V. E. Mayes and D. V. Nanopoulos, 2009, Physical Review D, **79**, 123528, Copyright 2009 by the American Physical Society. Part of this chapter is reprinted with permission from "The Search for a Realistic String Model at LHC" by J. A. Maxin, V. E. Mayes and D. V. Nanopoulos, 2010, Physical Review D, **81**, 015008, Copyright 2010 by the American Physical Society.

Type IIA string theory) fill four-dimensional Minkowski space-time and wrap 3-cycles in the compact manifold, with a stack of N $D6$-branes having a gauge group $U(N)$ (or $U(N/2)$ in the case of $\mathbf{T^6}/(\mathbf{Z}_2 \times \mathbf{Z}_2)$) in its world volume. The 3-cycles wrapped by the D-branes will in general intersect multiple times in the internal space, resulting in chiral fermions in the bifundamental representation localized at the intersections between different stacks. The multiplicity of such fermions is then given by the number of times the 3-cycles intersect.

In most intersecting D-brane models, problems arise that prevent the generation of masses and mixings for the first two families of quarks and leptons. However, there is one example known of an intersecting $D6$-brane model in Type IIA on the $\mathbf{T^6}/(\mathbf{Z_2} \times \mathbf{Z_2})$ orientifold where these problems may be solved [65, 66]. Thus, this particular model may be a step forward to obtaining realistic phenomenology from string theory. Indeed, as it has been recently shown [67, 68], it is possible within the moduli space of this model to obtain the correct SM quark masses and mixings, the tau lepton mass, and to generate naturally small neutrino masses. In addition to these features, the model exhibits automatic gauge coupling unification, and it is possible to generate realistic low-energy supersymmetric particle spectra, a subset of which may produce the observed dark matter density [67, 68, 69].

Although this model exhibits a realistic chiral sector, it cannot be considered fully realistic until the moduli stabilization problem has been completely addressed. For example, although it has been shown that it is possible to obtain correct Yukawa mass matrices, it is not possible to say that this is a unique solution until both open and closed string moduli VEVs can be fixed dynamically. However, in light of the soon to be operational Large Hadron Collider (LHC), it is still an interesting exercise to study the possible phenomenology of this model which could potentially be observed at LHC, which is the subject here.

Next, we turn our attention to the soft-supersymmetry breaking terms at the Grand Unification Theory (GUT) scale. In the present analysis, not all the F-terms of the moduli get VEVs for simplicity, as in [70, 71]. As discussed in [67, 68, 69], we will assume that the soft terms have no dependence on the physical Yukawa couplings.

For the present work we will consider u-moduli dominated SUSY breaking where both the cosmological constant V_0 and the goldstino angle are set to zero [67, 68]. Thus, with this parametrization, the gaugino mass terms may be written as [67, 68]

$$M_P = \frac{-\sqrt{3}m_{3/2}}{\mathrm{Re}f_P}\sum_{j=1}^{3}\left(\mathrm{Re}u^j\,\Theta_j\,e^{-i\gamma_j}\,n_P^j m_P^k m_P^l\right) \qquad (j,k,l)=(\overline{1,2,3}). \tag{3.1}$$

The Bino mass parameter is a linear combination of the gaugino mass for each stack,

$$M_Y = \frac{1}{f_Y}\sum_P c_P M_P \tag{3.2}$$

where the the coefficients c_P correspond to the linear combination of $U(1)$ factors which define the hypercharge, $U(1)_Y = \sum c_P U(1)_P$.

For the trilinear parameters, we have [67, 68]

$$\begin{aligned} A_{PQR} &= -\sqrt{3}m_{3/2}\sum_{j=1}^{3}\left[\Theta_j e^{-i\gamma_j}\left(1+(\sum_{k=1}^{3}\xi_{PQ}^{k,j}\Psi(\theta_{PQ}^k)-\frac{1}{4})+(\sum_{k=1}^{3}\xi_{RP}^{k,j}\Psi(\theta_{RP}^k)-\frac{1}{4})\right)\right] \\ &\quad +\frac{\sqrt{3}}{2}m_{3/2}\Theta_3 e^{-i\gamma_1} \end{aligned} \tag{3.3}$$

where P,Q, and R label the stacks of branes whose mutual intersections define the fields present in the corresponding trilinear coupling and the angle differences are defined as

$$\theta_{PQ} = \theta_Q - \theta_P. \tag{3.4}$$

We must be careful when dealing with cases where the angle difference is negative. Note for the present model, there is always either one or two of the θ_{PQ} which are

negative. The parameter

$$\eta_{PQ} = \mathrm{sgn}(\prod_i \theta^i_{PQ}), \tag{3.5}$$

is defined such that $\eta_{PQ} = -1$ indicates that only one of the angle differences is negative while $\eta_{PQ} = +1$ indicates that two of the angle differences are negative.

Finally, the squark and slepton (1/4 BPS) scalar mass-squared parameters are given by [67, 68]

$$\mathrm{m}^2_{PQ} = m^2_{3/2}\left[1 - 3\sum_{m,n=1}^{3}\Theta_m\Theta_n e^{-i(\gamma_m-\gamma_n)}\left(\frac{\delta_{mn}}{4} + \sum_{j=1}^{3}(\xi^{j,m}_{PQ}\Psi(\theta^j_{PQ}) + \xi^{j,m}_{PQ}\xi^{j,\bar{n}}_{PQ}\Psi'(\theta^j_{PQ}))\right)\right]. \tag{3.6}$$

The functions $\Psi(\theta_{PQ}) = \frac{\partial \ln(e^{-\phi_4}\tilde{K}_{PQ})}{\partial\theta_{PQ}}$ in the above formulas defined for $\eta_{PQ} = -1$ are [67, 68]

$$\begin{aligned}
&\text{if } \theta_{PQ} < 0 \quad : \qquad\qquad (3.7)\\
&\Psi(\theta^j_{PQ}) \;=\; -\gamma_E + \frac{1}{2}\frac{d}{d\theta^j_{PQ}}\ln\Gamma(-\theta^j_{PQ}) - \frac{1}{2}\frac{d}{d\theta^j_{PQ}}\ln\Gamma(1+\theta^j_{PQ}) + \ln(t^j + \bar{t}^j)\\
&\text{if } \theta_{PQ} > 0 \quad :\\
&\Psi(\theta^j_{PQ}) \;=\; -\gamma_E + \frac{1}{2}\frac{d}{d\theta^j_{PQ}}\ln\Gamma(1-\theta^j_{PQ}) - \frac{1}{2}\frac{d}{d\theta^j_{PQ}}\ln\Gamma(\theta^j_{PQ}) + \ln(t^j + \bar{t}^j),
\end{aligned}$$

and for $\eta_{PQ} = +1$ are

$$\begin{aligned}
&\text{if } \theta_{PQ} < 0 \quad : \qquad\qquad (3.8)\\
&\Psi(\theta^j_{PQ}) \;=\; \gamma_E + \frac{1}{2}\frac{d}{d\theta^j_{PQ}}\ln\Gamma(1+\theta^j_{PQ}) - \frac{1}{2}\frac{d}{d\theta^j_{PQ}}\ln\Gamma(-\theta^j_{PQ}) - \ln(t^j + \bar{t}^j)\\
&\text{if } \theta_{PQ} > 0 \quad :\\
&\Psi(\theta^j_{PQ}) \;=\; \gamma_E + \frac{1}{2}\frac{d}{d\theta^j_{PQ}}\ln\Gamma(\theta^j_{PQ}) - \frac{1}{2}\frac{d}{d\theta^j_{PQ}}\ln\Gamma(1-\theta^j_{PQ}) - \ln(t^j + \bar{t}^j).
\end{aligned}$$

The function $\Psi'(\theta_{PQ})$ is just the derivative

$$\Psi'(\theta^j_{PQ}) \;=\; \frac{d\Psi(\theta^j_{PQ})}{d\theta^j_{PQ}}, \tag{3.9}$$

and $\theta^{j,k}_{PQ}$ and $\theta^{j,k\bar{l}}_{PQ}$ are defined [71] as

$$\xi^{j,k}_{PQ} \equiv (u^k + \bar{u}^k)\,\frac{\partial\theta^j_{PQ}}{\partial u^k} = \begin{cases} \left[-\frac{1}{4\pi}\sin(2\pi\theta^j)\right]^P_Q & j = k \\ \left[\frac{1}{4\pi}\sin(2\pi\theta^j)\right]^P_Q & j \neq k, \end{cases} \tag{3.10}$$

$$\xi^{j,k\bar{l}}_{PQ} \equiv (u^k + \bar{u}^k)(u^l + \bar{u}^l)\,\frac{\partial^2\theta^j_{PQ}}{\partial u^k \partial \bar{u}^l} = \begin{cases} \frac{1}{16\pi}\left[\sin(4\pi\theta^j) + 4\sin(2\pi\theta^j)\right]^P_Q & j = k = l \\ \frac{1}{16\pi}\left[\sin(4\pi\theta^j) - 4\sin(2\pi\theta^j)\right]^P_Q & j \neq k = l \\ -\frac{1}{16\pi}\left[\sin(4\pi\theta^j)\right]^P_Q & j = k \neq l \text{ or } j = l \neq k \\ \frac{1}{16\pi}\left[\sin(4\pi\theta^j)\right]^P_Q & j \neq k \neq l \neq j. \end{cases} \tag{3.11}$$

Note that the only explicit dependence of the soft terms on the u and s moduli is in the gaugino mass parameters. The trilinears and scalar mass-squared values depend explicitly only on the angles.

In contrast to heterotic string models, the gaugino and scalar masses are typically not universal in intersecting D-brane constructions, although in the present case, there is some partial universality of the scalar masses due to the Pati-Salam unification at the string scale. In particular, the trilinear A couplings are found to be equal to a universal parameter, A_0, and the left-handed and right-handed squarks and sleptons respectively are degenerate. The Higgs scalar mass-squared values are found to be [67, 68]

$$m_H^2 = m_{3/2}^2\left(1 - \frac{3}{2}\left|\Theta_3\right|^2\right). \tag{3.12}$$

The complex structure moduli u^i and the four-dimensional dilaton ϕ_4 are fixed by the supersymmetry conditions and gauge coupling unification, respectively. Thus,

the free parameters which remain are Θ_1, Θ_2, sgn(Θ_3), t^2, t^3, the phases γ_i, and the gravitino mass $m_{3/2}$. In order to eliminate potential problems with electric dipole moments (EDM's) for the neutron and electron, $\gamma_i = 0$. In addition, the Kähler moduli on the second and third tori equal to one another, $\mathrm{Re}(t^2) = \mathrm{Re}(t^3) = 0.5$. Note that the soft terms only have a weak logarithmic dependence on the Kähler moduli. We constrain the parameter space such that neither the Higgs nor the squark and slepton scalar masses are tachyonic at the high scale, as well as imposing the unitary condition $\Theta_1^2 + \Theta_2^2 + \Theta_3^3 = 1$. In particular, we require $\Theta_3^2 \leq 2/3$, or equivalently $\Theta_1^2 + \Theta_2^2 \geq 1/3$. We thus now have three free parameters, Θ_1, Θ_2, and $m_{3/2}$.

Our goal in this work is to construct the expected final states at LHC and discuss how the model parameters can be determined at LHC for an intersecting $D6$-brane model. First, we generate sets of soft-supersymmetry breaking terms to reveal those regions of the parameter space that satisfy all the presently known experimental constraints and can generate the WMAP observed dark matter density and the relic density in the SSC scenario. Then we categorize all the regions of the experimentally allowed parameter space into different patterns of the superpartner mass spectra, where these patterns are organized by the masses of the four lightest sparticles. Using this data, we construct the intersecting $D6$-brane model final states at LHC and compare to the final states of mSUGRA. Next we show that the correct dark matter density can be obtained within this model in both the stau-neutralino and chargino-neutralino coannihilation regions. Finally, we discuss the challenges of constructing experimental observables to determine the $D6$-brane model parameters.

B. Parameter Space and Supersymmetry Spectra

We generate sets of the seven soft-supersymmetry breaking mass parameters at the unification scale using the equations given in Eqs. (3.1), (3.2), (3.3), (3.6), and (3.12) for u-moduli dominated SUSY breaking. The seven soft-supersymmetry breaking mass parameters are the gaugino masses $M3$, $M2$, and $M1$, the Higgs scalar mass-squared m_H^2, the left scalar mass m_L, the right scalar mass m_R, and the universal trilinear coupling A_0. We leave $\tan\beta$ as a free parameter, which gives a total of four free parameters, $\Theta_1,\ \Theta_2,\ m_{3/2}$, and $\tan\beta$, so we are led to a four-parameter model. The seven soft-supersymmetry breaking mass parameters at the unification scale are functions of the three goldstino angles $\Theta_1,\ \Theta_2,\ m_{3/2}$ which parameterize the F-terms.

The soft terms are run down to the electroweak scale via the Renormalization Group Equations (RGEs) and the corresponding relic neutralino density calculated as in Chapter II. We take the top quark mass to be $m_t = 172.6$ GeV [72]. The results are then filtered according to the criteria given in Chapter II.

The gravitino mass $m_{3/2}$ linearly scales the seven mass parameters at the unification scale. We scan these seven mass parameters for the u-moduli dominated SUSY breaking scenario for various values of $m_{3/2}$ and $\tan\beta$ to determine a suitable range for $m_{3/2}$, where we want to establish an upper limit such that $m_{3/2}$ becomes too massive at which few sparticles could be produced at LHC for an integrated luminosity of 10 fb^{-1}, and at the lower limit the Higgs mass becomes too light and violates the LEP constraint. To satisfy these conditions, we position the upper limit to be $m_{3/2} \approx 700$ GeV and compute the lower limit to be in the range $m_{3/2} = 400 \sim 500$ GeV. Consequently, to efficiently execute the substantial quantity of requisite computations, we limit our calculations of the experimental constraints, supersymmetry spectra, and relic density to $m_{3/2} = 500$ GeV and $m_{3/2} = 700$ GeV. For each $m_{3/2}$, the calculations

were completed for tanβ = 10, 25, and 46. Regions of the parameter space satisfying all the experimental constraints exist for five of the six cases; only $m_{3/2}$ = 700 GeV, tanβ = 10 produced no spectra that fulfilled the constraints. Additional low values of tanβ were run for $m_{3/2}$ = 700 GeV, though tanβ = 25 is the approximate minimum tanβ that violates none of the constraints. Thus, we study five cases for the u-moduli dominated SUSY breaking scenario in this work: $m_{3/2}$ = 500 GeV and tanβ = 10, $m_{3/2}$ = 500 GeV and tanβ = 25, $m_{3/2}$ = 500 GeV and tanβ = 46, $m_{3/2}$ = 700 GeV and tanβ = 25, $m_{3/2}$ = 700 GeV and tanβ = 46. These five cases will produce a broad spectrum of mass parameters at the unification scale such that a representative allowed parameter space can be determined.

We delineate the parameter space for the $D6$-brane model in terms of the goldstino angles Θ_1 and Θ_2. A detailed discussion of the goldstino angles Θ_1 and Θ_2 and how they relate to the non-universal gaugino masses and scalar masses can be found in [67] [68]. For clarity, we segregate the parameter space into distinctive scenarios of $m_{3/2}$ and tanβ, each scenario delineated by Θ_1 and Θ_2. One set of these four free parameters determines a unique point in the parameter space described by the seven soft-supersymmetry breaking mass parameters. The experimentally allowed parameter space for each of the five scenarios of $m_{3/2}$ and tanβ is exhibited in Fig. 7. Note in Fig. 7 that very constrained regions in the allowed parameter space exist that can generate the WMAP observed dark matter density, and furthermore, larger regions exist that can generate the diluted relic density in the SSC scenario. We see one consequence of raising $m_{3/2}$, which in effect increases the mass parameters, most consistently the gaugino mass $M3$, is to drive the relic density of some regions with already high levels of Ω_χ to levels where $\Omega_\chi \geq 1.1$. The increase in the mass parameters expands the mass difference between the lightest SUSY particle (LSP) $\widetilde{\chi}_1^0$ and the next to lightest SUSY particle (NLSP), thereby diminishing the prospects

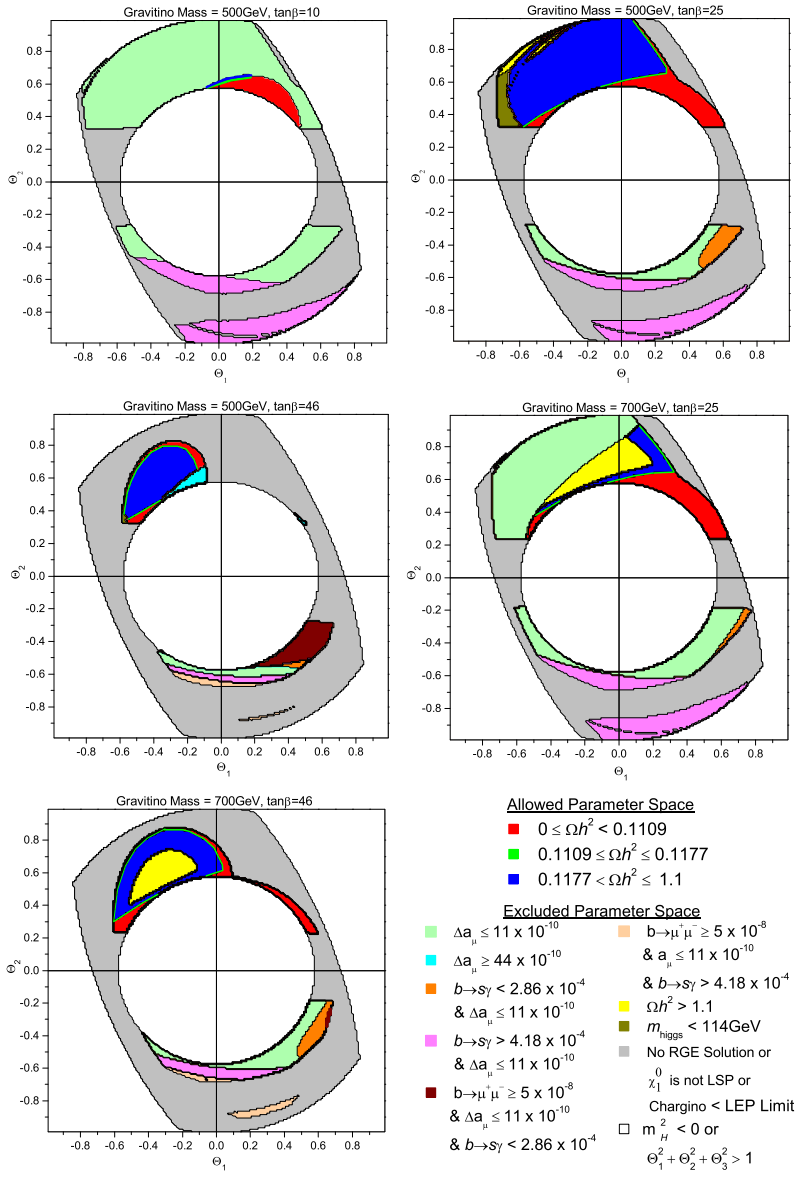

Fig. 7. Allowed parameter space for u-moduli dominated SUSY breaking scenario for an intersecting $D6$-brane model. The five individual charts represent different gravitino masses and $\tan\beta$. The chart legend describes the reasons for inclusion and exclusion of the shaded regions. Each separate region is outlined in black. Note the small regions excluded by the Higgs mass $m_h < 114$ GeV and $\Omega_{\chi^o} h^2 > 1.1$ satisfy all other constraints. The unshaded circular region centered at the origin is prohibited for driving m_H^2 to negative values, and the remaining unshaded regions are rejected since $\Theta_1^2 + \Theta_2^2 + \Theta_3^2 \neq 1$.

for coannihilation between the LSP and NLSP, and as a result, elevating the relic density. Those regions in Fig. 7 that can generate the WMAP observed dark matter density and relic density in the context of SSC are vital in this work to uncovering the expected final states at LHC. The circular region centered at the origin of the plot is excluded for driving m_H^2 to negative values. The region outside the allowed parameter space is excluded since the goldstino angles Θ_1, Θ_2, and Θ_3 do not satisfy the unitary condition $\Theta_1^2 + \Theta_2^2 + \Theta_3^2 = 1$ [67] [68].

We find that different regions of the parameter space that are allowed by the experimental constraints possess different patterns of mass hierarchies of the four lightest supersymmetric partners. Identification of the landscape of such mass patterns is of interest in classifying the possible experimental signals that may be expected at LHC [73]. Through a comprehensive scan of all regions of the allowed parameter space, we uncover five such patterns of mass hierarchies present. The five patterns present in the supersymmetry parameter space are shown in Table V for the u-moduli dominated SUSY breaking scenario.

Table V. Patterns of the four lightest sparticles for spectra allowed by all constraints for the intersecting $D6$-brane model (IBM).

Model	Pattern No.	Pattern Type	Mass Pattern
IBM	*ID6BraneP1*	Chargino	$\widetilde{\chi}_1^0 < \widetilde{\chi}_1^\pm < \widetilde{\chi}_2^0 < \widetilde{\tau}$
IBM	*ID6BraneP2*	Chargino	$\widetilde{\chi}_1^0 < \widetilde{\chi}_1^\pm < \widetilde{\tau} < \widetilde{\chi}_2^0$
IBM	*ID6BraneP3*	Chargino	$\widetilde{\chi}_1^0 < \widetilde{\chi}_1^\pm < \widetilde{\tau} < \widetilde{e}_R$
IBM	*ID6BraneP4*	Stau	$\widetilde{\chi}_1^0 < \widetilde{\tau} < \widetilde{\chi}_1^\pm < \widetilde{\chi}_2^0$
IBM	*ID6BraneP5*	Stau	$\widetilde{\chi}_1^0 < \widetilde{\tau} < \widetilde{e}_R < \widetilde{\chi}_1^\pm$

We now discuss each of these five patterns in detail. The $\widetilde{\chi}_1^\pm$ is the NLSP for the first three patterns in Table V. A small region of the allowed parameter space with

the *ID6BraneP1* pattern has the $\widetilde{\chi}_1^{\pm}$ and $\widetilde{\chi}_2^0$ mass nearly degenerate with the $\widetilde{\chi}_1^0$, with a mass difference ≤ 20 GeV, allowing for the observed dark matter density by WMAP to be generated in the chargino-neutralino coannihilation region. In addition, a large region of the allowed parameter space with the *ID6BraneP1* pattern has a very large mass difference between the $\widetilde{\chi}_1^{\pm}$ and $\widetilde{\chi}_1^0$, up to $\sim$150 GeV, generating a dark matter density up to $\Omega_\chi \sim 1.1$, possessing characteristics of the SSC scenario. In those regions of the parameter space in the SSC scenario with pattern *ID6BraneP1*, the $\widetilde{\chi}_1^{\pm}$ and $\widetilde{\chi}_2^0$ are virtually degenerate as well. We shall discuss the case of neutralino coannihilation in more detail later.

All the regions of the allowed parameter space with patterns *ID6BraneP2* and *ID6BraneP3* have a virtually degenerate mass between the $\widetilde{\chi}_1^{\pm}$ and $\widetilde{\chi}_1^0$, with a mass difference of less than 1 GeV. The virtually degenerate mass between the $\widetilde{\chi}_1^{\pm}$ and $\widetilde{\chi}_1^0$ in the regions of the allowed parameter space with patterns *ID6BraneP2* and *ID6BraneP3* allow for only a very small dark matter density to be generated, $\Omega_\chi \leq 0.01$, well below the WMAP observed relic density. Thus, in these regions with patterns *ID6BraneP2* and *ID6BraneP3*, the WMAP observed dark matter density must be predominantly composed of something other than the LSP since the lightest neutralino can only generate a small fraction of the dark matter for these regions of the parameter space.

We identify the fourth and fifth patterns in Table V as stau patterns since the $\widetilde{\tau}_1$ is the NLSP. As we shall soon discuss, regions of the allowed parameter space with the *ID6BraneP4* and *ID6BraneP5* patterns in the intersecting $D6$-brane model will produce physics similar to the stau-neutralino coannihilation region in mSUGRA. There are small regions of the allowed parameter space with both the *ID6BraneP4* and *ID6BraneP5* patterns with a mass difference between the $\widetilde{\tau}_1$ and $\widetilde{\chi}_1^0$ less than $\sim$20 GeV, generating the WMAP observed dark matter density in the stau-neutralino

coannihilation region. Furthermore, there are large regions of the allowed parameter space with patterns *ID6BraneP4* and *ID6BraneP5* that have a mass difference between the $\widetilde{\tau}_1$ and $\widetilde{\chi}_1^0$ of up to ∼160 GeV, generating a dark matter density up to Ω_χ ∼1.1, within the SSC scenario.

When discussing the final states which may be produced at the LHC in the next section, we shall focus on the *ID6BraneP1*, *ID6BraneP4*, and *ID6BraneP5* patterns since only these three patterns can generate the WMAP observed relic density, within the chargino-neutralino and stau-neutralino coannihilation regions, in addition to the diluted dark matter density in the context of SSC. We show in Fig. 8 all the regions of the allowed parameter space partitioned into the five patterns of the mass spectra we have discussed. In order to correlate the pattern space in Fig. 8 with the allowed parameter space in Fig. 7, the plots of the different patterns of the mass spectra in Fig. 8 are also delineated in terms of Θ_1 and Θ_2, segregated into the five $m_{3/2}$ and tanβ scenarios for clarity. The parameter space shown in Fig. 7 and the correlated landscape of mass patterns shown in Fig. 8 will serve as the basis for selection of typical points with which to derive the final states at LHC in the next section.

C. The Final States at LHC

The ultimate goal is to derive the model parameters from the experimental data. This is accomplished by constructing experimental kinematic observables that extract the expected final states while suppressing the Standard Model background. Measurements of the kinematic variables are then used to compute the model parameters. The final states in the present model will vary dependent upon the superpartner mass spectra patterns we have identified since each pattern may possess distinctive dominant decay chains and final states. Only regions of the parameter space with pat-

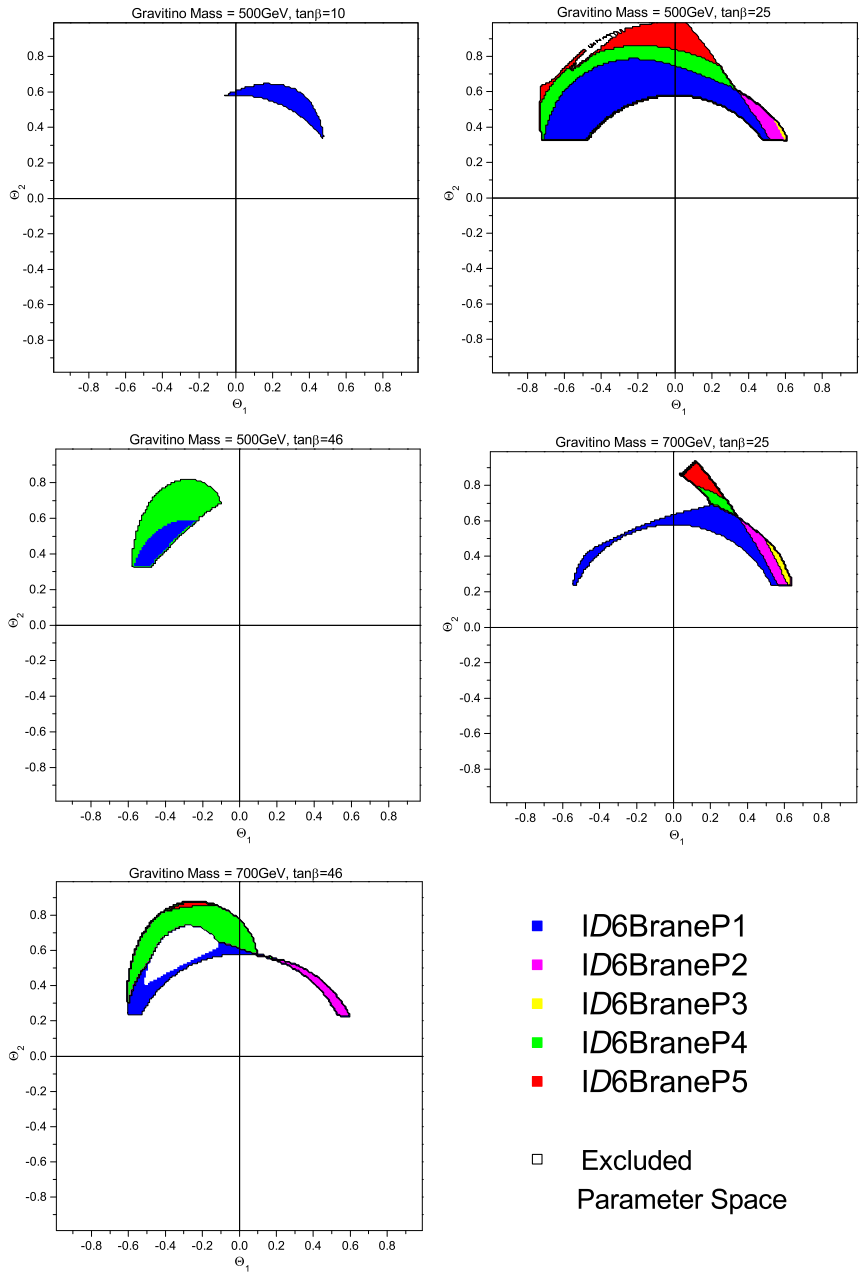

Fig. 8. Patterns of the mass spectra allowed by all the experimental constraints for the u-moduli dominated SUSY breaking scenario. The five individual charts represent different gravitino masses and tanβ. The allowed parameter space here correlates directly with the allowed parameter space in Fig 7. The shaded regions within each chart identify the five different patterns, and each separate region is outlined in black.

terns *ID6BraneP1*, *ID6BraneP4*, and *ID6BraneP5* will generate the WMAP observed relic density and the diluted dark matter density in the SSC scenario, so consequently, we shall only analyze the final states at LHC for points within the regions of the allowed parameter space with these three patterns. We select typical points from each of these three regions of the parameter space and examine the decay modes and final states. We shall choose a sample point and compute the final states, then vary the gaugino mass parameters $M3$, $M2$, and $M1$, the Higgs scalar mass-squared parameter m_H^2, the left scalar mass parameter m_L, the right scalar mass parameter m_R, and the universal trilinear coupling parameter A_0 to understand the effect of the variance on the states, while leaving $\tan\beta$ constant. The cross-sections and branching ratios are calculated with `PYTHIA 6.4`, using `SuSpect 2.34` to compute the sparticle masses.

We first analyze points within regions of the parameter space with pattern *ID6BraneP1* that generate the WMAP observed dark matter density. These points reside in the chargino-neutralino coannihilation region due to the small mass difference between the $\widetilde{\chi}_1^{\pm}$ and $\widetilde{\chi}_2^0$ with the $\widetilde{\chi}_1^0$. The processes with the largest production cross-sections are $q + \overline{q} \to \widetilde{\chi}_2^0 + \widetilde{\chi}_1^{\pm}$ and $q + \overline{q} \to \widetilde{q} + \widetilde{q}$. The NLSP is the $\widetilde{\chi}_1^{\pm}$, which is virtually degenerate with the $\widetilde{\chi}_2^0$, so for this reason, the $\widetilde{\chi}_1^{\pm}$ and $\widetilde{\chi}_2^0$ have large production cross-sections. Recall $\langle \sigma_{ann} v \rangle \propto \frac{1}{m^2}$, thus the more massive the particle, the smaller the differential cross-section. Since the $\widetilde{\tau}_1^{\pm}$ is more massive than the either the $\widetilde{\chi}_1^{\pm}$ or $\widetilde{\chi}_2^0$, the $\widetilde{\chi}_1^{\pm}$ and $\widetilde{\chi}_2^0$ will decay directly to opposite sign $\sim$20GeV lepton pairs and hadronic jets. Two typical points are shown in Table VI and Table VII. We see the most favored decay for $\widetilde{\chi}_2^0$ is $\widetilde{\chi}_2^0 \to \nu\overline{\nu}\widetilde{\chi}_1^0$, producing high energy $\sim$20GeV neutrinos. This is certainly not a dominant decay mode since production of low energy leptons (e, μ, τ) have a roughly equal branching ratio to the production of these high energy neutrinos. The $\widetilde{\chi}_1^0$ and neutrinos will exit the detector undetected, producing only missing energy P_{miss}^T. For the decay of $\widetilde{\chi}_1^{\pm}$, we are chiefly looking at the production

of jets through $\widetilde{\chi}_1^{\pm} \rightarrow q\overline{q}\widetilde{\chi}_1^0$, with a smaller branching ratio for the decay to low energy leptons. The other primary sources of jets are from $\widetilde{q}_R \rightarrow q\widetilde{\chi}_1^0$, $\widetilde{q}_L \rightarrow q\widetilde{\chi}_2^0$, and $\widetilde{q}_L \rightarrow q\widetilde{\chi}_1^{\pm}$. There is no change in these decay modes when we vary the mass parameters. Therefore, we have three principal signals to expect at LHC for these points that produce the WMAP observed dark matter density, where $l = (e, \mu)$:

- $jets + P_{Miss}^T$
- $2\tau + jets + P_{Miss}^T$
- $2l + jets + P_{Miss}^T$

Now we examine points within regions of the parameter space with pattern *ID6BraneP1* that generate the diluted dark matter density in the context of SSC. The mass difference between the $\widetilde{\chi}_1^{\pm}$ and $\widetilde{\chi}_2^0$ with the $\widetilde{\chi}_1^0$ is much greater, so these points do not necessarily lie within the chargino-neutralino coannihilation region of the parameter space. The three reference points we select are shown in Tables VIII, IX, and X. The processes with the largest production cross-sections for the point shown in Table VIII are $q + \overline{q} \rightarrow \widetilde{\chi}_1^{\pm} + \widetilde{\chi}_1^{\pm}$ and $q + \overline{q} \rightarrow \widetilde{q} + \widetilde{q}$. This point has the smallest mass parameters of these three points, however, as we increase the mass parameters to those in Tables IX and X, the production cross-sections for the aforementioned processes remain large, though the largest cross-section becomes $q + \overline{q} \rightarrow \widetilde{\chi}_1^0 + \widetilde{\chi}_1^{\pm}$. We have the same dominant decay modes as the WMAP points, but as the mass parameters increase, the branching ratios for the $\widetilde{\chi}_1^{\pm}$ decays change only slightly, while the branching ratio for the high energy neutrinos increases to as high as 50%. Additionally, the branching ratios for the production of two tau decrease from those of the WMAP regions, and the larger mass difference between the $\widetilde{\chi}_1^{\pm}$ and $\widetilde{\chi}_2^0$ with the $\widetilde{\chi}_1^0$ will produce $\geq$ 20 GeV lepton pairs and neutrinos. The primary source of jets

Table VI. Low energy supersymmetric particles and masses (in GeV) for *ID6BraneP1* point, Θ_1 = -0.08, Θ_2 = 0.58, $M3 = 602$, $M2 = 251$, $M1 = 430$, $m_H = 59$, $m_L = 273$, $m_R = 312$, A_0 = -37, tan$\beta = 25$, $m_{3/2} = 500$. The relic density for this point is $\Omega_\chi = 0.1127$. Here, $l = (e, \mu)$.

$\widetilde{g}$	$\widetilde{u}_L$	$\widetilde{t}_2$	$\widetilde{b}_2$	$\widetilde{e}_L$	$\widetilde{\tau}_2$	$\widetilde{\chi}_2^0$	$\widetilde{\chi}_2^\pm$
	$\widetilde{u}_R$	$\widetilde{t}_1$	$\widetilde{b}_1$	$\widetilde{e}_R$	$\widetilde{\tau}_1$	$\widetilde{\chi}_1^0$	$\widetilde{\chi}_1^\pm$
1373	1228	1176	1213	324	380	193	809
	1237	1017	1127	352	268	175	193

$Br(\widetilde{\chi}_2^0 \to \nu\bar{\nu}\widetilde{\chi}_1^0)(\%)$	$Br(\widetilde{\chi}_1^\pm \to q\bar{q}\widetilde{\chi}_1^0)(\%)$
$Br(\widetilde{\chi}_2^0 \to l^+l^-\widetilde{\chi}_1^0)(\%)$	$Br(\widetilde{\chi}_1^\pm \to l^\pm\nu\widetilde{\chi}_1^0)(\%)$
$Br(\widetilde{\chi}_2^0 \to \tau^+\tau^-\widetilde{\chi}_1^0)(\%)$	$Br(\widetilde{\chi}_1^\pm \to \tau^\pm\nu\widetilde{\chi}_1^0)(\%)$
46.2	59.3
17.7	26.7
33.0	13.9

are the same as the WMAP regions. Hence, we expect essentially the same signals as those of the WMAP regions, but the signals in the SSC regions should be easily distinguished from the WMAP regions by observing a larger mass difference between the $\widetilde{\chi}_1^\pm$ and $\widetilde{\chi}_2^0$ with the $\widetilde{\chi}_1^0$.

Next we study points within regions of the allowed parameter space with pattern *ID6BraneP4* that generate the observed WMAP dark matter density. Here, the mass difference between the $\widetilde{\tau}_1$ and $\widetilde{\chi}_1^0$ is nearly degenerate, so these points lie within the stau-neutralino coannihilation region of the parameter space. Three typical points from regions of the parameter space with pattern *ID6BraneP4* are shown

Table VII. Low energy supersymmetric particles and masses (in GeV) for *ID6BraneP1* point, Θ_1 = -0.06, $\Theta_2 = 0.58$, $M3 = 844$, $M2 = 351$, $M1 = 611$, $m_H = 69$, $m_L = 376$, $m_R = 435$, A_0 = -67, $\tan\beta = 25$, $m_{3/2} = 700$. The relic density for this point is $\Omega_\chi = 0.1117$. Here, $l = (e, \mu)$.

$\widetilde{g}$	$\widetilde{u}_L$	$\widetilde{t}_2$	$\widetilde{b}_2$	$\widetilde{e}_L$	$\widetilde{\tau}_2$	$\widetilde{\chi}_2^0$	$\widetilde{\chi}_2^\pm$
	$\widetilde{u}_R$	$\widetilde{t}_1$	$\widetilde{b}_1$	$\widetilde{e}_R$	$\widetilde{\tau}_1$	$\widetilde{\chi}_1^0$	$\widetilde{\chi}_1^\pm$
1873	1669	1572	1646	446	508	275	1091
	1683	1401	1534	490	396	254	275

$Br(\widetilde{\chi}_2^0 \to \nu\bar{\nu}\widetilde{\chi}_1^0)(\%)$	$Br(\widetilde{\chi}_1^\pm \to q\bar{q}\widetilde{\chi}_1^0)(\%)$
$Br(\widetilde{\chi}_2^0 \to l^+l^-\widetilde{\chi}_1^0)(\%)$	$Br(\widetilde{\chi}_1^\pm \to l^\pm\nu\widetilde{\chi}_1^0)(\%)$
$Br(\widetilde{\chi}_2^0 \to \tau^+\tau^-\widetilde{\chi}_1^0)(\%)$	$Br(\widetilde{\chi}_1^\pm \to \tau^\pm\nu\widetilde{\chi}_1^0)(\%)$
47.4	62.1
22.8	25.2
26.4	12.7

Table VIII. Low energy supersymmetric particles and masses (in GeV) for *ID6BraneP1* point, Θ_1 = -0.43, Θ_2 = 0.47, $M3 = 537$, $M2 = 203$, $M1 = 303$, $m_H = 164$, $m_L = 406$, $m_R = 298$, $A_0 = 186$, tan$\beta = 25$, $m_{3/2} = 500$. The relic density for this point is $\Omega_\chi = 1.0076$. Here, $l = (e, \mu)$.

$\widetilde{g}$	$\widetilde{u}_L$	$\widetilde{t}_2$	$\widetilde{b}_2$	$\widetilde{e}_L$	$\widetilde{\tau}_2$	$\widetilde{\chi}_2^0$	$\widetilde{\chi}_2^\pm$
	$\widetilde{u}_R$	$\widetilde{t}_1$	$\widetilde{b}_1$	$\widetilde{e}_R$	$\widetilde{\tau}_1$	$\widetilde{\chi}_1^0$	$\widetilde{\chi}_1^\pm$
1239	1149	1098	1103	428	433	154	722
	1116	929	1057	320	285	122	154

$Br(\widetilde{\chi}_2^0 \to \nu\overline{\nu}\widetilde{\chi}_1^0)(\%)$	$Br(\widetilde{\chi}_1^\pm \to q\bar{q}\widetilde{\chi}_1^0)(\%)$
$Br(\widetilde{\chi}_2^0 \to l^+l^-\widetilde{\chi}_1^0)(\%)$	$Br(\widetilde{\chi}_1^\pm \to l^\pm\nu\widetilde{\chi}_1^0)(\%)$
$Br(\widetilde{\chi}_2^0 \to \tau^+\tau^-\widetilde{\chi}_1^0)(\%)$	$Br(\widetilde{\chi}_1^\pm \to \tau^\pm\nu\widetilde{\chi}_1^0)(\%)$
30.8	64.8
21.6	23.3
10.3	11.8

Table IX. Low energy supersymmetric particles and masses (in GeV) for *ID6BraneP1* point, Θ_1 = -0.19, $\Theta_2 = 0.66$, $M3 = 600$, $M2 = 285$, $M1 = 379$, $m_H = 227$, $m_L = 327$, $m_R = 306$, A_0 = -11, $\tan\beta = 25$, $m_{3/2} = 500$. The relic density for this point is $\Omega_\chi = 0.9166$. Here, $l = (e, \mu)$.

$\widetilde{g}$	$\widetilde{u}_L$	$\widetilde{t}_2$	$\widetilde{b}_2$	$\widetilde{e}_L$	$\widetilde{\tau}_2$	$\widetilde{\chi}_2^0$	$\widetilde{\chi}_2^\pm$
	$\widetilde{u}_R$	$\widetilde{t}_1$	$\widetilde{b}_1$	$\widetilde{e}_R$	$\widetilde{\tau}_1$	$\widetilde{\chi}_1^0$	$\widetilde{\chi}_1^\pm$
1368	1238	1178	1206	378	398	221	787
	1229	1007	1134	338	286	154	221

$Br(\widetilde{\chi}_2^0 \to \nu\bar{\nu}\widetilde{\chi}_1^0)(\%)$	$Br(\widetilde{\chi}_1^\pm \to q\bar{q}\widetilde{\chi}_1^0)(\%)$
$Br(\widetilde{\chi}_2^0 \to l^+l^-\widetilde{\chi}_1^0)(\%)$	$Br(\widetilde{\chi}_1^\pm \to l^\pm\nu\widetilde{\chi}_1^0)(\%)$
$Br(\widetilde{\chi}_2^0 \to \tau^+\tau^-\widetilde{\chi}_1^0)(\%)$	$Br(\widetilde{\chi}_1^\pm \to \tau^\pm\nu\widetilde{\chi}_1^0)(\%)$
42.5	59.2
27.8	26.8
10.0	14.0

Table X. Low energy supersymmetric particles and masses (in GeV) for *ID6BraneP1* point, $\Theta_1 = 0.2$, $\Theta_2 = 0.69$, $M3 = 839$, $M2 = 418$, $M1 = 661$, $m_H = 366$, $m_L = 384$, $m_R = 322$, A_0 = -336, tan$\beta = 25$, $m_{3/2} = 700$. The relic density for this point is $\Omega_\chi = 1.0790$. Here, $l = (e, \mu)$.

$\widetilde{g}$	$\widetilde{u}_L$	$\widetilde{t}_2$	$\widetilde{b}_2$	$\widetilde{e}_L$	$\widetilde{\tau}_2$	$\widetilde{\chi}_2^0$	$\widetilde{\chi}_2^\pm$
	$\widetilde{u}_R$	$\widetilde{t}_1$	$\widetilde{b}_1$	$\widetilde{e}_R$	$\widetilde{\tau}_1$	$\widetilde{\chi}_1^0$	$\widetilde{\chi}_1^\pm$
1862	1670	1554	1607	477	487	331	1072
	1651	1340	1519	404	339	276	331

$Br(\widetilde{\chi}_2^0 \to \nu\overline{\nu}\widetilde{\chi}_1^0)(\%)$	$Br(\widetilde{\chi}_1^\pm \to q\bar{q}\widetilde{\chi}_1^0)(\%)$
$Br(\widetilde{\chi}_2^0 \to l^+l^-\widetilde{\chi}_1^0)(\%)$	$Br(\widetilde{\chi}_1^\pm \to l^\pm\nu\widetilde{\chi}_1^0)(\%)$
$Br(\widetilde{\chi}_2^0 \to \tau^+\tau^-\widetilde{\chi}_1^0)(\%)$	$Br(\widetilde{\chi}_1^\pm \to \tau^\pm\nu\widetilde{\chi}_1^0)(\%)$
50.5	57.0
28.8	27.9
14.1	15.1

in Tables XI, XII, and XIII. The processes with the largest production cross-sections for these points are $q + \overline{q} \rightarrow \widetilde{\chi}_1^{\pm} + \widetilde{\chi}_1^{\pm}$, $q + \overline{q} \rightarrow \widetilde{\chi}_2^0 + \widetilde{\chi}_1^{\pm}$, and $q + \overline{q} \rightarrow \widetilde{q} + \widetilde{q}$. The $\widetilde{\chi}_1^{\pm}$ and $\widetilde{\chi}_2^0$ are virtually degenerate, whereas the $\widetilde{\tau}_1^{\pm}$ is lighter than both the $\widetilde{\chi}_1^{\pm}$ and $\widetilde{\chi}_2^0$, so both the $\widetilde{\chi}_1^{\pm}$ and $\widetilde{\chi}_2^0$ will decay to $\widetilde{\tau}_1^{\pm}$ nearly 100% of the time. The second lightest neutralino will decay to tau through the decay chain $\widetilde{\chi}_2^0 \rightarrow \widetilde{\tau}_1^{\pm}\tau^{\mp} \rightarrow \tau^{\pm}\tau^{\mp}\widetilde{\chi}_1^0$, while the chargino will also decay to tau through $\widetilde{\chi}_1^{\pm} \rightarrow \widetilde{\tau}_1^{\pm}\nu \rightarrow \tau^{\pm}\nu\widetilde{\chi}_1^0$, so the results of both decay chains will be low energy tau. The squark decay chain will provide jets through $\widetilde{q}_R \rightarrow q\widetilde{\chi}_1^0$, $\widetilde{q}_L \rightarrow q\widetilde{\chi}_2^0$, and $\widetilde{q}_L \rightarrow q\widetilde{\chi}_1^{\pm}$. As the mass parameters were varied, there was no change in the final states. Therefore, we expect to see the signal $\tau + jets + P_{Miss}^T$ at LHC for these points that produce the WMAP observed dark matter density.

We now analyze points within regions of the parameter space with pattern *ID6BraneP4* that generate the diluted dark matter density in the context of SSC. The three sample points from regions of the parameter space with pattern *ID6BraneP4* are shown in Tables XIV, XV, and XVI. Here the mass difference between the $\widetilde{\tau}_1$ and $\widetilde{\chi}_1^0$ is much greater than those points in the WMAP region, so we are no longer within the stau-neutralino coannihilation region, so accordingly, the relic density is larger. The $\widetilde{\chi}_1^{\pm}$ and $\widetilde{\chi}_2^0$ are still virtually degenerate, so both will decay to $\widetilde{\tau}_1$ almost 100% of the time, with the exception of the point in Table XV. The mass parameters for this point will produce some $W^{\pm}$ bosons through $\widetilde{\chi}_1^{\pm} \rightarrow W^{\pm}\widetilde{\chi}_1^0$ with a branching ratio of 25.5%, though $\widetilde{\chi}_1^{\pm} \rightarrow \widetilde{\tau}^{\pm}\nu$ is still the dominant decay mode. Otherwise, the dominant decay chains and source of the jets remain the same as the WMAP regions, as well as the processes with the largest cross-sections. In essence, we expect the same signals as those of the WMAP regions, but the signals in the SSC regions should be clearly discriminated from the WMAP regions by observing a larger mass difference between the $\widetilde{\tau}_1$ with the $\widetilde{\chi}_1^0$, namely the production of high energy tau as opposed to the low

Table XI. Low energy supersymmetric particles and masses (in GeV) for *ID6BraneP4* point, Θ_1 = -0.19, $\Theta_2 = 0.75$, $M3 = 599$, $M2 = 324$, $M1 = 354$, $m_H = 315$, $m_L = 346$, $m_R = 292$, A_0 = -50, tan$\beta = 46$, $m_{3/2} = 500$. The relic density for this point is $\Omega_\chi = 0.1166$.

$\widetilde{g}$	$\widetilde{u}_L$	$\widetilde{t}_2$	$\widetilde{b}_2$	$\widetilde{e}_L$	$\widetilde{\tau}_2$	$\widetilde{\chi}_2^0$	$\widetilde{\chi}_2^\pm$	$Br(\widetilde{\chi}_2^0 \to \widetilde{\tau}_1\tau)(\%)$
	$\widetilde{u}_R$	$\widetilde{t}_1$	$\widetilde{b}_1$	$\widetilde{e}_R$	$\widetilde{\tau}_1$	$\widetilde{\chi}_1^0$	$\widetilde{\chi}_1^\pm$	$Br(\widetilde{\tau}_1 \to \tau\widetilde{\chi}_1^0)(\%)$
								$Br(\widetilde{\chi}_1^\pm \to \widetilde{\tau}^\pm\nu)(\%)$
1363	1244	1150	1157	406	422	254	760	99.9
	1222	989	1087	321	161	144	254	100.0
								99.6

energy tau in the WMAP region.

Lastly, we consider points within regions of the allowed parameter space with pattern *ID6BraneP5* that generate the observed WMAP dark matter density. In this region, the mass difference between the $\widetilde{\tau}_1$ and $\widetilde{\chi}_1^0$ is nearly degenerate, so these points lie within the stau-neutralino coannihilation region. Two representative points from regions of the parameter space with pattern *ID6BraneP5* are shown in Table XVII and Table XVIII. The processes with the largest production cross-sections for these points are $q + \overline{q} \to \widetilde{q} + \widetilde{q}$, $q + \overline{q} \to \widetilde{q} + \widetilde{g}$, $q + \overline{q} \to \widetilde{\chi}_1^\pm + \widetilde{\chi}_1^\pm$, and $q + \overline{q} \to \widetilde{\chi}_2^0 + \widetilde{\chi}_1^\pm$. The $\widetilde{\chi}_1^\pm$ and $\widetilde{\chi}_2^0$ are virtually degenerate, and the $\widetilde{\tau}_1^\pm$ is lighter than both the $\widetilde{\chi}_1^\pm$ and $\widetilde{\chi}_2^0$, so the decay chains for the $\widetilde{\chi}_1^\pm$ and $\widetilde{\chi}_2^0$ are the same as those for regions of the parameter space with pattern *ID6BraneP4* that generate the WMAP observed relic density, resulting in low energy tau. However, with a larger gluino production cross-section, we can include the process $\widetilde{g} \to q\widetilde{q}$ as one of the primary sources of jets, in

Table XII. Low energy supersymmetric particles and masses (in GeV) for *ID6BraneP4* point, Θ_1 = -0.59, Θ_2 = 0.46, $M3$ = 681, $M2$ = 278, $M1$ = 299, m_H = 407, m_L = 693, m_R = 349, A_0 = 371, tanβ = 46, $m_{3/2}$ = 700. The relic density for this point is $\Omega_\chi = 0.1130$.

$\widetilde{g}$	$\widetilde{u}_L$	$\widetilde{t}_2$	$\widetilde{b}_2$	$\widetilde{e}_L$	$\widetilde{\tau}_2$	$\widetilde{\chi}_2^0$	$\widetilde{\chi}_2^\pm$	$Br(\widetilde{\chi}_2^0 \to \widetilde{\tau}_1\tau)(\%)$
	$\widetilde{u}_R$	$\widetilde{t}_1$	$\widetilde{b}_1$	$\widetilde{e}_R$	$\widetilde{\tau}_1$	$\widetilde{\chi}_1^0$	$\widetilde{\chi}_1^\pm$	$Br(\widetilde{\tau}_1 \to \tau\widetilde{\chi}_1^0)(\%)$
								$Br(\widetilde{\chi}_1^\pm \to \widetilde{\tau}^\pm\nu)(\%)$
1545	1501	1376	1374	713	684	217	859	99.9
	1374	1135	1267	365	132	121	217	100.0
								99.5

Table XIII. Low energy supersymmetric particles and masses (in GeV) for *ID6BraneP4* point, Θ_1 = 0.02, Θ_2 = 0.68, $M3$ = 856, $M2$ = 412, $M1$ = 616, m_H = 308, m_L = 381, m_R = 396, A_0 = -186, tanβ = 46, $m_{3/2}$ = 700. The relic density for this point is $\Omega_\chi = 0.1128$.

$\widetilde{g}$	$\widetilde{u}_L$	$\widetilde{t}_2$	$\widetilde{b}_2$	$\widetilde{e}_L$	$\widetilde{\tau}_2$	$\widetilde{\chi}_2^0$	$\widetilde{\chi}_2^\pm$	$Br(\widetilde{\chi}_2^0 \to \widetilde{\tau}_1\tau)(\%)$
	$\widetilde{u}_R$	$\widetilde{t}_1$	$\widetilde{b}_1$	$\widetilde{e}_R$	$\widetilde{\tau}_1$	$\widetilde{\chi}_1^0$	$\widetilde{\chi}_1^\pm$	$Br(\widetilde{\tau}_1 \to \tau\widetilde{\chi}_1^0)(\%)$
								$Br(\widetilde{\chi}_1^\pm \to \widetilde{\tau}^\pm\nu)(\%)$
1895	1694	1551	1586	471	512	327	1073	99.9
	1692	1389	1498	457	276	257	327	100.0
								99.9

Table XIV. Low energy supersymmetric particles and masses (in GeV) for *ID6BraneP4* point, Θ_1 = -0.44, $\Theta_2 = 0.58$, $M3 = 548$, $M2 = 251$, $M1 = 283$, $m_H = 271$, $m_L = 431$, $m_R = 291$, $A_0 = 147$, $\tan\beta = 46$, $m_{3/2} = 500$. The relic density for this point is $\Omega_\chi = 0.5003$.

$\widetilde{g}$	$\widetilde{u}_L$	$\widetilde{t}_2$	$\widetilde{b}_2$	$\widetilde{e}_L$	$\widetilde{\tau}_2$	$\widetilde{\chi}_2^0$	$\widetilde{\chi}_2^\pm$	$Br(\widetilde{\chi}_2^0 \to \widetilde{\tau}_1\tau)(\%)$
	$\widetilde{u}_R$	$\widetilde{t}_1$	$\widetilde{b}_1$	$\widetilde{e}_R$	$\widetilde{\tau}_1$	$\widetilde{\chi}_1^0$	$\widetilde{\chi}_1^\pm$	$Br(\widetilde{\tau}_1 \to \tau\widetilde{\chi}_1^0)(\%)$
								$Br(\widetilde{\chi}_1^\pm \to \widetilde{\tau}^\pm\nu)(\%)$
1260	1178	1095	1094	461	460	195	711	99.9
	1131	930	1026	310	173	114	195	100.0
								99.9

Table XV. Low energy supersymmetric particles and masses (in GeV) for *ID6BraneP4* point, Θ_1 = -0.51, $\Theta_2 = 0.52$, $M3 = 730$, $M2 = 315$, $M1 = 355$, $m_H = 380$, $m_L = 642$, $m_R = 387$, $A_0 = 286$, $\tan\beta = 46$, $m_{3/2} = 700$. The relic density for this point is $\Omega_\chi = 1.0030$.

$\widetilde{g}$	$\widetilde{u}_L$	$\widetilde{t}_2$	$\widetilde{b}_2$	$\widetilde{e}_L$	$\widetilde{\tau}_2$	$\widetilde{\chi}_2^0$	$\widetilde{\chi}_2^\pm$	$Br(\widetilde{\chi}_2^0 \to \widetilde{\tau}_1\tau)(\%)$
	$\widetilde{u}_R$	$\widetilde{t}_1$	$\widetilde{b}_1$	$\widetilde{e}_R$	$\widetilde{\tau}_1$	$\widetilde{\chi}_1^0$	$\widetilde{\chi}_1^\pm$	$Br(\widetilde{\tau}_1 \to \tau\widetilde{\chi}_1^0)(\%)$
								$Br(\widetilde{\chi}_1^\pm \to \widetilde{\tau}^\pm\nu)(\%)$
1644	1560	1430	1431	672	649	247	917	94.6
	1469	1220	1352	408	238	145	247	100.0
								74.5

Table XVI. Low energy supersymmetric particles and masses (in GeV) for *ID6BraneP4* point, Θ_1 = -0.27, Θ_2 = 0.76, $M3$ = 819, $M2$ = 460, $M1$ = 444, m_H = 482, m_L = 535, m_R = 408, A_0 = -20, tanβ = 46, $m_{3/2}$ = 700. The relic density for this point is Ω_χ = 1.0521.

$\widetilde{g}$	$\widetilde{u}_L$	$\widetilde{t}_2$	$\widetilde{b}_2$	$\widetilde{e}_L$	$\widetilde{\tau}_2$	$\widetilde{\chi}_2^0$	$\widetilde{\chi}_2^\pm$	$Br(\widetilde{\chi}_2^0 \to \widetilde{\tau}_1\tau)(\%)$
	$\widetilde{u}_R$	$\widetilde{t}_1$	$\widetilde{b}_1$	$\widetilde{e}_R$	$\widetilde{\tau}_1$	$\widetilde{\chi}_1^0$	$\widetilde{\chi}_1^\pm$	$Br(\widetilde{\tau}_1 \to \tau\widetilde{\chi}_1^0)(\%)$
								$Br(\widetilde{\chi}_1^\pm \to \widetilde{\tau}^\pm\nu)(\%)$
1821	1677	1523	1535	611	594	367	986	98.1
	1627	1331	1469	439	267	184	367	100.0
								98.0

addition to the squark decay chains $\widetilde{q}_R \to q\widetilde{\chi}_1^0$, $\widetilde{q}_L \to q\widetilde{\chi}_2^0$, and $\widetilde{q}_L \to q\widetilde{\chi}_1^\pm$. Thus, we anticipate the signal $\tau + jets + P_{Miss}^T$ at LHC for these points that produce the WMAP observed dark matter density.

To conclude the discussion of the final states, we investigate points within regions of the parameter space with pattern *ID6BraneP5* that generate the diluted dark matter density in the SSC scenario. Two representative points from regions of the parameter space with pattern *ID6BraneP5* are shown in Table XIX and Table XX. Here the mass difference between the $\widetilde{\tau}_1$ and $\widetilde{\chi}_1^0$ is much larger than those points in the WMAP region, thus, these points do not reside within the stau-neutralino coannihilation region. The $\widetilde{\chi}_1^\pm$ and $\widetilde{\chi}_2^0$ are still virtually degenerate, so the dominant decay mode for both is to $\widetilde{\tau}_1$, but not necessarily 100% of the time. We do find for the point in Table XIX a small branching ratio of 16.2% for the production of the lightest Higgs boson through $\widetilde{\chi}_2^0 \to h_0\widetilde{\chi}_1^0$, though the dominant decay chain remains $\widetilde{\chi}_2^0 \to \widetilde{\tau}_1\tau$.

Table XVII. Low energy supersymmetric particles and masses (in GeV) for *ID6BraneP5* point, $\Theta_1 = 0.14$, $\Theta_2 = 0.88$, $M3 = 577$, $M2 = 381$, $M1 = 385$, $m_H = 415$, $m_L = 305$, $m_R = 187$, A_0 = -295, tan$\beta = 25$, $m_{3/2} = 500$. The relic density for this point is $\Omega_\chi = 0.1118$.

$\widetilde{g}$	$\widetilde{u}_L$ $\widetilde{u}_R$	$\widetilde{t}_2$ $\widetilde{t}_1$	$\widetilde{b}_2$ $\widetilde{b}_1$	$\widetilde{e}_L$ $\widetilde{e}_R$	$\widetilde{\tau}_2$ $\widetilde{\tau}_1$	$\widetilde{\chi}_2^0$ $\widetilde{\chi}_1^0$	$\widetilde{\chi}_2^\pm$ $\widetilde{\chi}_1^\pm$	$Br(\widetilde{\chi}_2^0 \to \widetilde{\tau}_1\tau)(\%)$ $Br(\widetilde{\tau}_1 \to \tau\widetilde{\chi}_1^0)(\%)$ $Br(\widetilde{\chi}_1^\pm \to \widetilde{\tau}^\pm\nu)(\%)$
1313	1201	1123	1131	395	394	299	728	97.0
	1161	904	1078	237	166	158	299	100.0
								96.9

The lower mass parameters for the point in Table XIX will also produce some $W^\pm$ bosons through $\widetilde{\chi}_1^\pm \to W^\pm\widetilde{\chi}_1^0$ with a branching ratio of 21.7%, though $\widetilde{\chi}_1^\pm \to \widetilde{\tau}^\pm\nu$ is still the dominant decay mode. The h_0 and $W^\pm$ branching ratios decrease as the mass parameters are increased. Other than these differences, the dominant decay chains and source of the jets remain the same as the WMAP regions, as well as the processes with the largest production cross-sections. Thus, we foresee similar signals as those of the WMAP regions, however, the signals in the SSC regions should be distinguished from the WMAP regions by observation of the much larger mass difference between the $\widetilde{\tau}_1$ with the $\widetilde{\chi}_1^0$, resulting in high energy tau, in contrast to low energy tau in the WMAP region.

We now have the complete set of final states for the model in hand, so we can compare them to the expected final states for mSUGRA. In the region of the mSUGRA allowed parameter space that can generate the WMAP observed dark

Table XVIII. Low energy supersymmetric particles and masses (in GeV) for *ID6BraneP5* point, $\Theta_1 = 0.27$, $\Theta_2 = 0.73$, $M3 = 823$, $M2 = 442$, $M1 = 655$, $m_H = 447$, $m_L = 411$, $m_R = 253$, A_0 = -420, tan$\beta = 25$, $m_{3/2} = 700$. The relic density for this point is $\Omega_\chi = 0.1117$.

$\widetilde{g}$	$\widetilde{u}_L$	$\widetilde{t}_2$	$\widetilde{b}_2$	$\widetilde{e}_L$	$\widetilde{\tau}_2$	$\widetilde{\chi}_2^0$	$\widetilde{\chi}_2^\pm$	$Br(\widetilde{\chi}_2^0 \to \widetilde{\tau}_1\tau)(\%)$
	$\widetilde{u}_R$	$\widetilde{t}_1$	$\widetilde{b}_1$	$\widetilde{e}_R$	$\widetilde{\tau}_1$	$\widetilde{\chi}_1^0$	$\widetilde{\chi}_1^\pm$	$Br(\widetilde{\tau}_1 \to \tau\widetilde{\chi}_1^0)(\%)$
								$Br(\widetilde{\chi}_1^\pm \to \widetilde{\tau}^\pm\nu)(\%)$
								99.9
1827	1651	1528	1565	508	505	351	1043	100.0
	1610	1289	1494	350	280	274	351	99.9

Table XIX. Low energy supersymmetric particles and masses (in GeV) for *ID6BraneP5* point, Θ_1 = -0.23, $\Theta_2 = 0.87$, $M3 = 565$, $M2 = 376$, $M1 = 279$, $m_H = 422$, $m_L = 389$, $m_R = 271$, A_0 = -89, tan$\beta = 25$, $m_{3/2} = 500$. The relic density for this point is $\Omega_\chi = 0.8199$.

$\widetilde{g}$	$\widetilde{u}_L$	$\widetilde{t}_2$	$\widetilde{b}_2$	$\widetilde{e}_L$	$\widetilde{\tau}_2$	$\widetilde{\chi}_2^0$	$\widetilde{\chi}_2^\pm$	$Br(\widetilde{\chi}_2^0 \to \widetilde{\tau}_1\tau)(\%)$
	$\widetilde{u}_R$	$\widetilde{t}_1$	$\widetilde{b}_1$	$\widetilde{e}_R$	$\widetilde{\tau}_1$	$\widetilde{\chi}_1^0$	$\widetilde{\chi}_1^\pm$	$Br(\widetilde{\chi}_2^0 \to h_0\widetilde{\chi}_1^0)(\%)$
								$Br(\widetilde{\tau}_1 \to \tau\widetilde{\chi}_1^0)(\%)$
								$Br(\widetilde{\chi}_1^\pm \to \widetilde{\tau}^\pm\nu)(\%)$
								80.2
1294	1205	1130	1133	458	456	295	701	16.2
	1156	917	1089	292	244	113	295	100.0
								78.3

Table XX. Low energy supersymmetric particles and masses (in GeV) for *ID6BraneP5* point, Θ_1 = 0.09, Θ_2 = 0.84, $M3$ = 833, $M2$ = 509, $M1$ = 560, m_H = 528, m_L = 418, m_R = 312, A_0 = -344, tanβ = 25, $m_{3/2}$ = 700. The relic density for this point is Ω_χ = 1.0380.

								$Br(\widetilde{\chi}_2^0 \to \widetilde{\tau}_1\tau)(\%)$
$\widetilde{g}$	$\widetilde{u}_L$	$\widetilde{t}_2$	$\widetilde{b}_2$	$\widetilde{e}_L$	$\widetilde{\tau}_2$	$\widetilde{\chi}_2^0$	$\widetilde{\chi}_2^\pm$	$Br(\widetilde{\chi}_2^0 \to h_0\widetilde{\chi}_1^0)(\%)$
	$\widetilde{u}_R$	$\widetilde{t}_1$	$\widetilde{b}_1$	$\widetilde{e}_R$	$\widetilde{\tau}_1$	$\widetilde{\chi}_1^0$	$\widetilde{\chi}_1^\pm$	$Br(\widetilde{\tau}_1 \to \tau\widetilde{\chi}_1^0)(\%)$
								$Br(\widetilde{\chi}_1^\pm \to \widetilde{\tau}^\pm\nu)(\%)$
								94.6
1847	1674	1547	1588	534	529	405	1017	4.3
	1633	1306	1515	375	308	233	405	100.0
								94.5

matter density, primarily squarks and gluinos will be produced in the stau-neutralino coannihilation region. The characteristic decay chain in this region of mSUGRA is $\widetilde{q} \rightarrow q\widetilde{\chi}_2^0 \rightarrow q\tau^{\pm}\widetilde{\tau}_1^{\mp} \rightarrow q\tau^{\pm}\tau^{\mp}\widetilde{\chi}_1^0$. In the mSUGRA region of the allowed parameter space that can generate the relic density in the SSC scenario, the three characteristic decays are $\widetilde{\chi}_2^0 \rightarrow \widetilde{\tau}_1^{\pm}\tau^{\mp} \rightarrow \tau^{\pm}\tau^{\mp}\widetilde{\chi}_1^0$, $\widetilde{\chi}_2^0 \rightarrow h_0\widetilde{\chi}_1^0$, and $\widetilde{\chi}_2^0 \rightarrow Z^0\widetilde{\chi}_1^0$ [7]. In the region of the $D6$-brane model parameter space with patterns *ID6BraneP4* and *ID6BraneP5* that can generate the WMAP observed relic density, we see similar states to that of mSUGRA, namely low energy ($\leq$20 GeV) opposite sign tau pairs. On the other hand, the states do begin to differ between the $D6$-brane model and mSUGRA in the SSC scenario. We showed that the final states in the SSC region for patterns *ID6BraneP4* and *ID6BraneP5* will be high energy ($\geq$20 GeV) opposite sign tau pairs. High energy tau will be dominant in the region of the mSUGRA parameter space with a large universal gaugino mass $m_{1/2}$, nevertheless, as $m_{1/2}$ is decreased, the dominant decay chains shift to the Higgs boson and Z boson. Therefore, we see similar LHC signals in the SSC region of the $D6$-brane allowed parameter space with patterns *ID6BraneP4* and *ID6BraneP5* and the SSC region of the mSUGRA allowed parameter space only at higher values of $m_{1/2}$. For lower values of $m_{1/2}$ in mSUGRA in the SSC region, there are obvious distinctions with the $D6$-brane model. Clearly identifiable differences exist between the LHC states of mSUGRA and the $D6$-brane model states in the regions of the allowed parameter space with pattern *ID6BraneP1*. The decay $\widetilde{\chi}_2^0 \rightarrow \nu\overline{\nu}\widetilde{\chi}_1^0$ is favored in the $D6$-brane model, but is kinematically forbidden in mSUGRA, and moreover, the production of opposite sign tau pairs is suppressed in the WMAP and SSC regions of the $D6$-brane parameter space with pattern *ID6BraneP1*, as compared to mSUGRA.

D. Neutralino Coannihilation

We have found that in the region of the allowed parameter space that generates the WMAP constrained dark matter density for patterns *ID6BraneP4* and *ID6BraneP5*, the final states of an intersecting $D6$-brane model are essentially the same as the final states for mSUGRA. In mSUGRA, only specific regions of the parameter space are cosmologically allowed within the WMAP dark matter density upper and lower bounds. One of these regions is referred to as the stau-neutralino coannihilation region, where early universe neutralinos can annihilate with stau, producing low-energy tau. It is characterized by a nearly degenerate mass between the lightest neutralino $\widetilde{\chi}_1^0$ and the tau slepton $\widetilde{\tau}_1$, this near degeneracy measured by the mass difference $\Delta\mathrm{M} = m_{\widetilde{\tau}_1} - m_{\widetilde{\chi}_1^0}$. We found regions of the $D6$-brane model parameter space with stau patterns *ID6BraneP4* and *ID6BraneP5* possess stau-neutralino coannihilation regions, as shown in Fig. 9. The regions plotted in Fig. 9 have 1.7 GeV $< \Delta\mathrm{M} \leq$ 20 GeV. In these regions of the $D6$-brane model parameter space, the stau decays to a neutralino and tau 100% of the time through the process $\widetilde{\tau}_1^{\pm} \rightarrow \widetilde{\chi}_1^0 \tau^{\pm}$, thus, if $\Delta\mathrm{M} \leq 1.7$ GeV, the mass of the tau, then the only evidence of the process will be missing energy. In light of this, for this particular plot we exclude regions of the parameter space where $\Delta\mathrm{M} \leq 1.7$ GeV. If we restrict the upper bound to $\sim$20 GeV, then the result will be low energy tau production. Thus, we expect to find similarities between the final states within the shaded regions in Fig. 9 and those regions in the coannihilation region of mSUGRA. This will affect how the intersecting $D6$-brane model can be validated at LHC, since any analysis of kinematical variables will have to discriminate between the coannihilation region of mSUGRA and the *ID6BraneP4* and *ID6BraneP5* regions of the $D6$-brane model parameter space. We shall discuss this in more detail shortly.

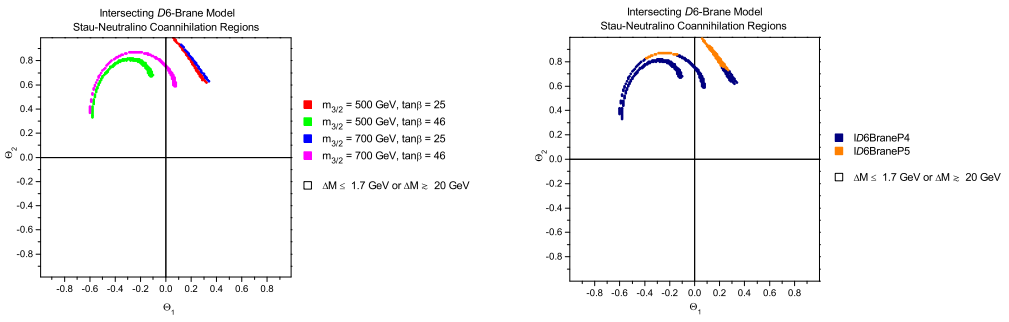

Fig. 9. Stau-neutralino coannihilation regions within the intersecting $D6$-Brane model allowed parameter space. The upper plot is differentiated by gravitino mass and $\tan\beta$, whilst the lower plot is differentiated by the mass hierarchy patterns. $\Delta M = m_{\widetilde{\tau}_1} - m_{\widetilde{\chi}_1^0}$. These regions will generate the WMAP observed dark matter density.

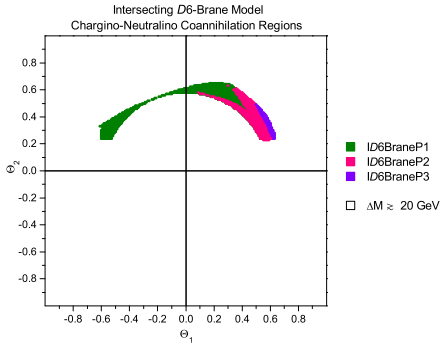

Fig. 10. Chargino-neutralino coannihilation regions within the intersecting $D6$-Brane model allowed parameter space. The plot is differentiated by the mass hierarchy patterns. The shaded regions represent a mass difference of 20 GeV between the $\widetilde{\chi}_1^{\pm}$ or $\widetilde{\chi}_2^0$ and the $\widetilde{\chi}_1^0$. Of the three regions plotted here, only the *ID6BraneP1* region will generate the WMAP observed dark matter density and diluted relic density in the SSC scenario. The *ID6BraneP2* and *ID6BraneP3* regions can only generate an extremely small relic density of $\Omega_\chi \leq 0.01$.

The regions in Fig. 7 that generate the WMAP observed dark matter density that are not represented in Fig. 9 are situated in the chargino-neutralino coannihilation region. In this region in an intersecting $D6$-brane model, the lightest neutralino $\widetilde{\chi}_1^0$ has a nearly degenerate mass with the lightest chargino $\widetilde{\chi}_1^{\pm}$ and second lightest neutralino $\widetilde{\chi}_2^0$. Here, early universe $\widetilde{\chi}_1^0$ can annihilate with $\widetilde{\chi}_1^{\pm}$ and $\widetilde{\chi}_2^0$. We found regions of the parameter space with the patterns *ID6BraneP1*, *ID6BraneP2*, and *ID6BraneP3* containing chargino-neutralino coannihilation regions, as shown in Fig. 10. However, only regions of the parameter space with pattern *ID6BraneP1* can generate the WMAP observed relic density in the chargino-coannihilation region. Furthermore, regions of the allowed parameter space with the patterns *ID6BraneP2* and *ID6BraneP3* cannot generate the diluted dark matter density in the SSC scenario either, however, regions with the pattern *ID6BraneP1* can generate the correct SSC relic density. The regions of the parameter space with patterns *ID6BraneP2* and *ID6BraneP3* can only generate an extremely small relic density of $\Omega_\chi \leq 0.01$, thus, the neutralino could only comprise a very small portion of the WMAP observed dark matter density. The remainder of the relic density would have to be composed of matter other than neutralinos. We use an upper bound of $\sim$20 GeV in Fig. 10 to include all of the regions that generate the WMAP relic density. The stau-neutralino coannihilation region in the intersecting $D6$-brane model and in mSUGRA produces low energy tau from stau decays, and this is in contrast to low energy tau in the chargino-neutralino coannihilation region predominantly resulting from $\widetilde{\chi}_1^{\pm}$ and $\widetilde{\chi}_2^0$ decays. This fact will be important when constructing kinematical observables that must distinguish between the intersecting $D6$-brane model and mSUGRA.

E. Observables and Model Parameter Determination

The ultimate goal is to determine the model parameters of the intersecting brane model, although this presents new challenges since the soft-terms are in general non-universal. In the present model we have seven soft-supersymmetry breaking mass parameters at the unification scale which are functions of three goldstino angles which parameterize the F-terms, along with the free parameter $\tan\beta$. A minimum of four experimental observables are needed to determine the model parameters, where the four observables could be constructed so as to determine four of the eight parameters, say, for example, $M3$, m_L, A_0, and $\tan\beta$. Once $M3$, m_L, and A_0 are determined, then Eqs. (3.1), (3.3), and (3.6) can be solved simultaneously for the three free parameters Θ_1, Θ_2, and $m_{3/2}$. After solving these three equations, these three free parameters can be used to compute the remaining four soft-supersymmetry breaking mass parameters $M2$, $M1$, m_R, and m_H^2, and henceforth, along with a known $\tan\beta$, the sparticle masses and relic density can be computed. It has yet to be determined whether four experimental observables could be constructed to compute four of the eight $D6$-brane model parameters. For mSUGRA, it was shown in [74] that the model parameters can be determined for the WMAP constrained region of the relic density, and in [7] in the context of SSC, where four experimental observables were derived, one for each of the four soft-supersymmetry breaking parameters in mSUGRA.

The final states in the regions of the parameter space with pattern *ID6BraneP1* are different than the final states in regions of the parameter space with patterns *ID6BraneP4* and *ID6BraneP5*, demonstrated by the fact the $D6$-brane model contains both stau-neutralino and chargino-neutralino coannihilation regions that generate the WMAP observed dark matter density, as well as multiple independent regions that generate the diluted relic density of the SSC scenario. This greatly complicates

the task since the construction of experimental observables to determine the model parameters in those regions of the parameter space with pattern *ID6BraneP1* will not necessarily determine the model parameters in those regions of the parameter space with patterns *ID6BraneP4* and *ID6BraneP5*. Therefore, with the intersecting $D6$-brane model parameter space as it is currently constrained by Standard Model measurements, it is likely more than four experimental observables will be necessary. The final states in the WMAP and SSC regions of the parameter space are quite similar, though the energy of the lepton pairs will be higher in the SSC region than in the WMAP region. This will necessitate different selection cuts on the data distributions, creating a new experimental observable. Therefore, in this context, the maximum number of observables necessary to determine the model parameters in the $D6$-brane model could well exceed four.

It is essential that an intersecting $D6$-brane model be distinguished from mSUGRA, though this task is complicated by the possibility that the final states of both models are similar in the stau-neutralino coannihilation regions. For the $D6$-brane model, the goal is to build four experimental observables to determine the seven soft-supersymmetry breaking terms and $\tan\beta$ by solving for the free parameters and then computing the remaining soft terms. Likewise, it has been shown [74][7] that only four observables are necessary to determine the model parameters in mSUGRA, although the universal gaugino and scalar masses in mSUGRA will be different from the non-universal masses in an intersecting brane model. However, since none of the experimentally allowed regions of the $D6$-brane model parameter space that we generated using the equations given in Eqs. (3.1), (3.2), (3.3), (3.6), and (3.12) for u-moduli dominated SUSY breaking have universal gaugino masses and universal scalar masses, mSUGRA is not presumed to be a subset of the $D6$-brane model, and hence, the observables in the $D6$-brane model will most likely possess a different construction than the corre-

sponding observables in mSUGRA.

Construction of experimental observables that can determine model parameters is beyond the scope of this work. In order to do this it is first imperative that the parameter space be further constrained to eventually narrow down the number of different patterns of the mass spectra to only one. This could limit the number of experimental observables necessary to determine the model parameters to four. This can be accomplished by application of new data, both from colliders and from cosmological measurements, such as from direct dark-matter detection and constraints on the galactic gamma flux resulting from neutralino annihilations. For a discussion on direct dark matter detection cross-sections and annihilation rates in the present model, see [75] and the following section.

F. Stringy Wimp Detection

As briefly mentioned in the Introduction, observations in cosmology and astrophysics suggest the presence of a stable dark matter particle. Supersymmetry (SUSY) supplies a satisfactory candidate for a dark matter particle, where R-parity is conserved and the lightest supersymmetric particle (LSP) is stable [1], which is usually the lightest neutralino $\widetilde{\chi}_1^0$ [1, 2]. Two proposed methods of discovering this weakly interacting massive particle (WIMP) are directly through WIMP interactions with ordinary matter and indirectly via the products of WIMP annihilations. The direct detection method searches for elastic scattering of WIMPs off nuclei in underground experiments. The experiments are conducted in deep underground laboratories in an effort to reduce the background to minimal levels. The indirect detection method seeks out debris resulting from WIMP annihilations in the galactic halo. One galactic process that could produce gamma-rays from WIMP annihilation is the process $\widetilde{\chi}_1^0\widetilde{\chi}_1^0 \rightarrow \gamma\gamma$,

where two gamma-rays are produced directly from a WIMP annihilation, and another is $\widetilde{\chi}_1^0\widetilde{\chi}_1^0 \to q\overline{q} \to \pi^0 \to \gamma\gamma$. Analyses of direct detection cross-sections and gamma-ray flux within mSUGRA (or CMSSM) models have been completed [14, 15, 16, 17]. It is, however, a worthwhile pursuit to analyze the direct and indirect detection parameters in alternative models.

In this work we show the parameter space allowed by all the experimental constraints for this intersecting $D6$-brane model for varying cases of gravitino masses and tanβ. The spin-independent cross-sections are computed and plotted against the current dark matter detection experiment constraints. Furthermore, we present the proton spin-dependent cross-sections, whereas the computed neutron spin-dependent cross-sections only vary slightly from those of the proton, so the neutron cross-sections are not shown. The gamma-ray flux resulting from neutralino annihilations in the galactic halo for the $D6$-brane model is plotted and compared to the most recent telescope measurements. Finally, in order to compare our results with a model with universal soft terms representing the opposite extreme, we calculate the spin-independent and spin-dependent cross-sections for the so-called one-parameter model [38, 39, 40, 62], including the gamma-ray flux. The one-parameter model of Chapter II is a highly constrained small subset of the mSUGRA parameter space such that the soft supersymmetry breaking terms are all functions of the common gaugino mass. In no-scale supergravity models, generically $m_0 = m_0(m_{1/2})$ and $A = A(m_{1/2})$, thus the number of free parameters is reduced to two, $m_{1/2}$ and tanβ. Adopting a strict no-scale framework, one can also fix the B-parameter as $B = B(m_{1/2})$, and hence we are led to a *one-parameter* model where all of the soft terms may be fixed in terms of $m_{1/2}$. Therefore, the one-parameter model represents a suitable case with which to compare the intersecting $D6$-brane model with non-universal soft supersymmetry breaking terms.

The set of soft terms at the unification scale are generated in the same manner as was performed in [68] for u-moduli dominated SUSY breaking. The soft terms are run down to the electroweak scale via the Renormalization Group Equations (RGEs) and the corresponding relic neutralino density calculated as in Chapter II. We take the top quark mass to be $m_t = 172.6$ GeV [72]. The results are then filtered according to the criteria given in Chapter II.

Direct detection experiments search for dark matter through an elastic collision of WIMPs with ordinary matter. The lightest neutralino, χ_1^0, is assumed to be stable, and as such represents the best possible candidate for dark matter, and hence, WIMPs. These WIMPs produce low energy recoils with nuclei. The interaction between the WIMPs and nuclei can be segregated into a spin-independent (SI) part and a spin-dependent(SD) part, where the SI (scalar) interactions are primarily the consequence of elastic collisions with heavy nuclei. First, we consider the SI cross-sections for an intersecting $D6$-brane model, then study the SD interactions.

Both the direct detection cross-sections and the gamma-ray flux are calculated using `MicrOMEGAs 2.1` [76]. For the SI calculation, we use the nucleon form factor coefficient values of

$$f_d^p = 0.033,\ f_u^p = 0.023,\ f_s^p = 0.26$$

$$f_d^n = 0.042,\ f_u^n = 0.018,\ f_s^n = 0.26$$

while for the SD computations, we use the following quark density coefficients

$$\Delta_u^p = 0.842 \pm 0.012,\ \Delta_d^p = -0.427 \pm 0.013,\ \Delta_s^p = -0.085 \pm 0.018$$

$$\Delta_u^n = \Delta_d^p,\ \Delta_d^n = \Delta_u^p,\ \Delta_s^n = \Delta_s^p$$

In addition, we use $v_0 = 220$ km/s for the dark matter velocity distribution in the galaxy rest frame, $v_E = 244.4$ km/s for the Earth velocity with respect to the

galaxy, and $v_{max} = 600$ km/s for the maximal dark matter velocity in the sun's orbit with respect to the galaxy.

In Fig. 11, we plot the SI cross-sections for an intersecting $D6$-brane model. The cross-sections and flux were calculated only for those regions of the parameter space satisfying all the experimental constraints. Those allowed regions are shown in Fig. 7. The plots in Fig. 11 are subdivided by dark matter density, where for clarity we use the 2σ WMAP limits. The most recent experimental results for Zeplin-III [8], Xenon 10 [9], and CDMS [10] are shown, in addition to the projected sensitivity of the future SuperCDMS [77] and Xenon-1 Ton [78] experiments. Only for $m_{3/2} = 500$ GeV and $\tan\beta = 10$ are the cross-sections within the current experimental limits, however, in this case there is only a small region of the allowed parameter space within the CDMS results, where these points have a very small dark matter density only allowed since we removed the lower WMAP 2σ boundary. Most of the points will be within the experimental limits of the SuperCDMS and Xenon-1 Ton future experiments, potentially providing incentive for the design and development of the next generation of dark matter direct detection experiments. In the SSC region, we allow for a dilution factor of $\mathcal{O}(10)$, resulting in a dark matter density up to $\Omega_{\chi^\circ} h^2 \sim 1.1$, permitting the inclusion of more points. As can be seen in Fig. 11, in general, the SSC regions have a smaller cross-section than the WMAP regions. The dark matter density $\Omega_{\chi^\circ} h^2$ is inversely proportional to the annihilation cross-section $\langle \sigma_{ann} v \rangle$, so one expects the points with a higher $\Omega_{\chi^\circ} h^2$ to possess a smaller annihilation cross-section, as depicted in Fig. 11.

The proton SD cross-sections are shown in Fig. 12. The format of the SD charts is similar to the SI charts. For comparison of the intersecting $D6$-brane model cross-sections to the current experimental limits, we show the latest results for COUPP [79], NAIAD [80], KIMS [81], and SuperK [82]. We also calculated the neutron SD cross-

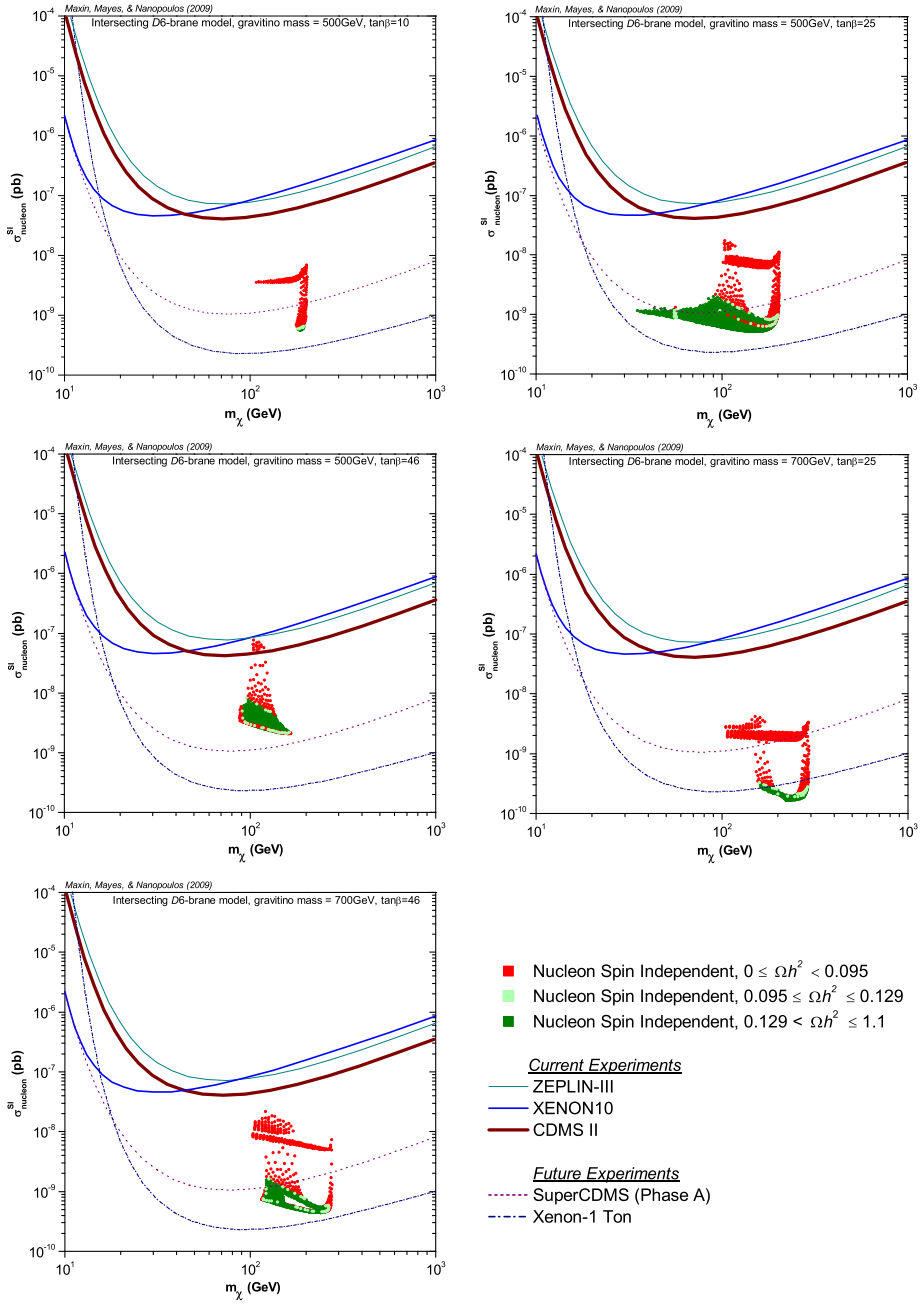

Fig. 11. Spin-independent cross-sections of an intersecting $D6$-brane model. Each marker satisfies all experimental constraints for an explicit gravitino mass and $\tan\beta$. The three marker colors identify the dark matter density.

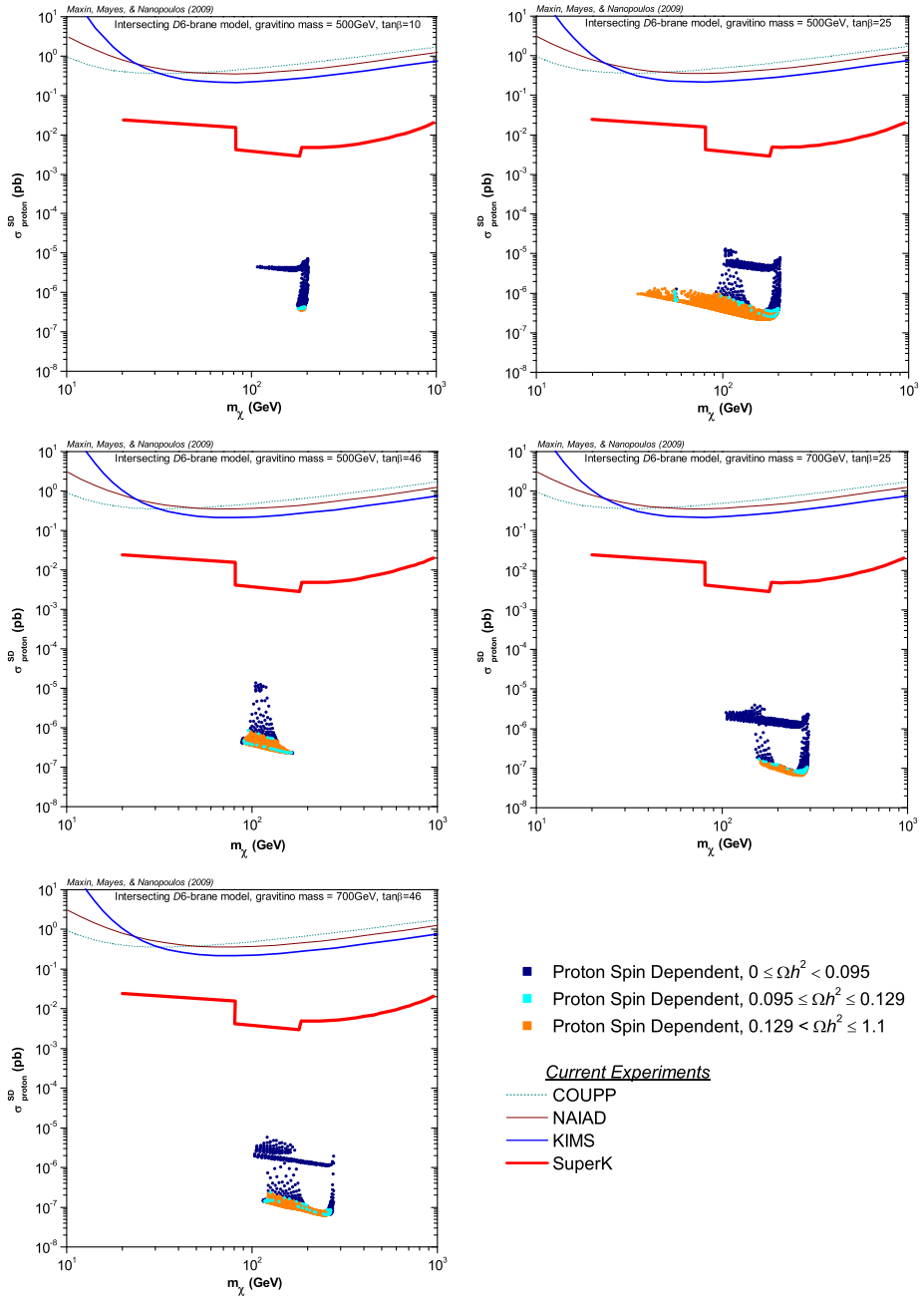

Fig. 12. Proton spin-dependent cross-sections of an intersecting $D6$-brane model. Each marker satisfies all experimental constraints for an explicit gravitino mass and $\tan\beta$. The three marker colors identify the dark matter density.

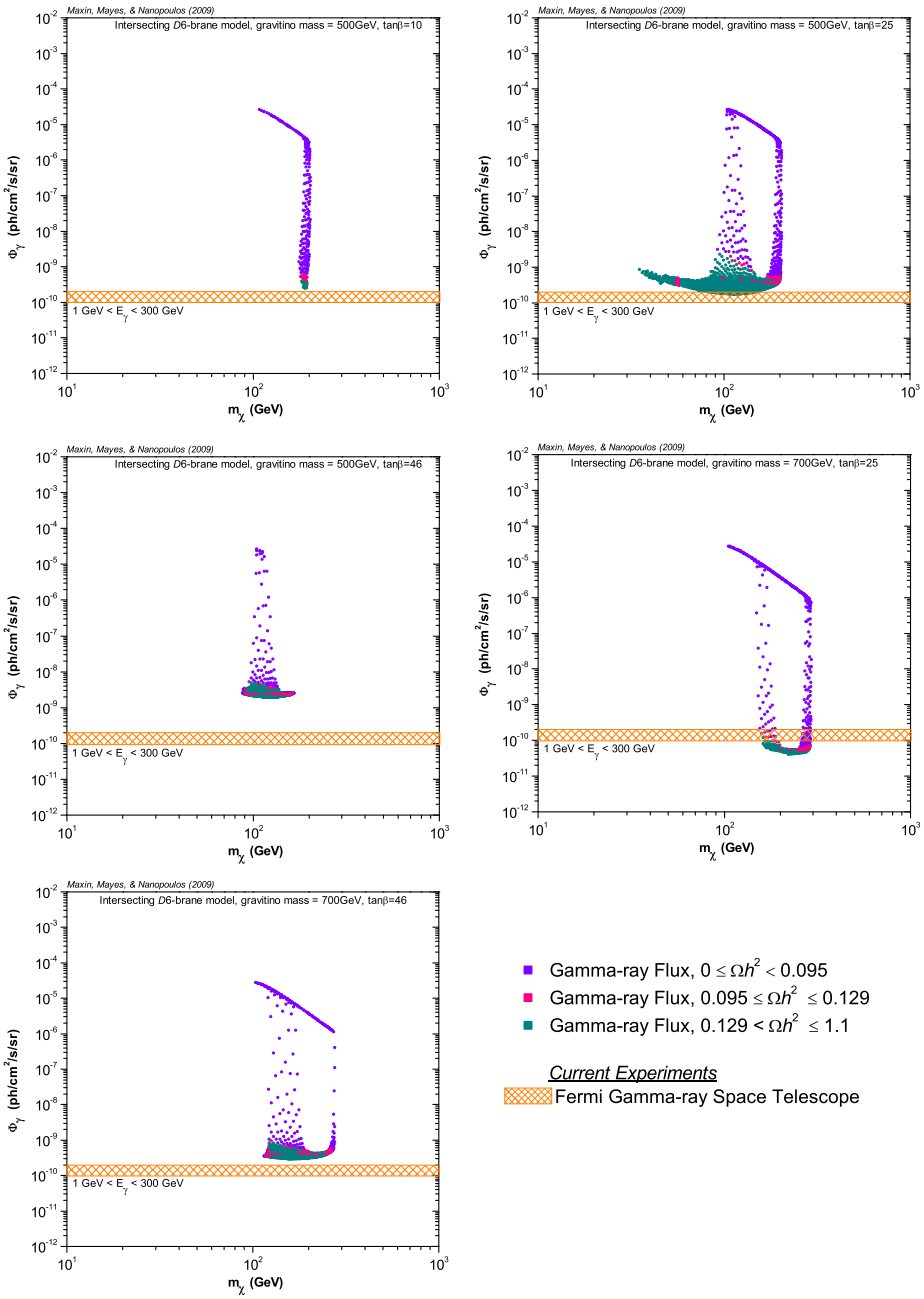

Fig. 13. Gamma-ray flux of an intersecting $D6$-brane model. Each marker satisfies all experimental constraints for an explicit gravitino mass and $\tan\beta$. The three marker colors identify the dark matter density.

sections (not shown), though there was only a slight difference between the proton and neutron SD. The patterns were generally the same, but the neutron SD cross-sections were slightly larger, and the shape of the SD patterns is essentially identical to the SI patterns. None of the intersecting $D6$-brane model points are within the current experimental limits of the SD dark matter detectors, and in fact, they are still three orders of magnitude away from the discovery region. Again, since $\Omega_{\chi^o} h^2 \sim \frac{1}{\langle \sigma ann v \rangle}$, we see in Fig. 12 that the SSC points have in general a smaller annihilation cross-section than the WMAP points.

G. Indirect Dark Matter Detection

Indirect detection experiments search for high energy neutrinos, gamma-rays, positrons, and anti-protons emanating from neutralino annihilation in the galactic halo and core, or in the case of neutrinos, in the core of the sun or the earth. In this section, we focus only on the flux of gamma-rays Φ_γ in the galactic core or halo. The gamma-ray flux Φ_γ for the intersecting $D6$-brane model is shown in Fig. 13, including the projected sensitivity of the Fermi experiment [12]. The sensitivity is not constant, but is a function of photon energy, and for this reason, to be precise, we delineate it using a band. Most of the points allowed by the experimental constraints will be within the sensitivity of the Fermi telescope. As mentioned in the Introduction, two possible decay channels where WIMPs can produce gamma-rays in the galactic core and halo are $\widetilde{\chi}_1^0 \widetilde{\chi}_1^0 \to \gamma\gamma$ and $\widetilde{\chi}_1^0 \widetilde{\chi}_1^0 \to q\overline{q} \to \pi^0 \to \gamma\gamma$. Hence, the flux of gamma-rays is directly dependent upon the annihilation cross-section. Fig. 11 and Fig. 12 show and we have explained that the SSC points have a smaller annihilation cross-section. Consequently, we expect the SSC points to also exhibit a smaller gamma-ray flux Φ_γ, and accordingly, this is illustrated in Fig. 13.

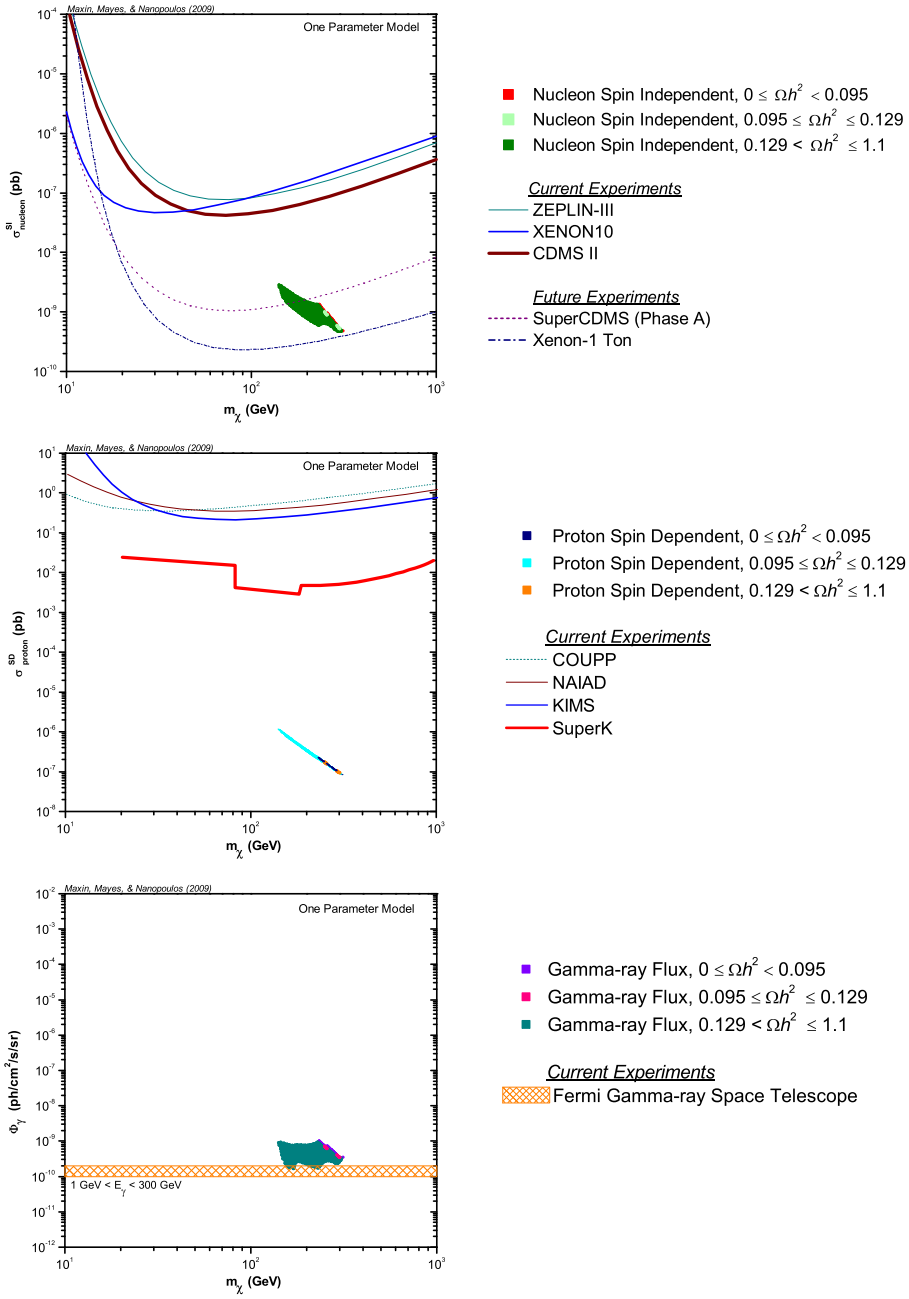

Fig. 14. Spin-independent cross-section, proton spin-dependent cross-section, and gamma-ray flux for the one-parameter model. Each marker satisfies all experimental constraints. The different marker colors identify the dark matter density.

H. Universality vs. Non-universality WIMP Detection

It is an intriguing question as to how a model with non-universal soft-supersymmetry breaking terms, such as an intersecting $D6$-brane model, compares to a model with universal soft-supersymmetry breaking terms, for example, mSUGRA. The one-parameter model [38, 39, 40, 62] of Chapter II is a highly constrained small subset of mSUGRA, where all the soft-supersymmetry breaking terms may be fixed in terms of the gaugino mass $m_{1/2}$. The OPM has universal soft-supersymmetry breaking terms, so it is ideal to compare to the $D6$-brane model. Details of the phenomenology of the OPM using the most recent measurements of the experimental constraints can be found in [62]. The parameter space of the OPM is quite constrained by the experimental constraints, and this leads to small regions of allowed direct and indirect detection parameters. In Fig. 14 we plot the direct and indirect detection parameters of the OPM. As described in [62], the range of $\tan\beta$ for spectra that satisfy all the experimental constraints in the WMAP region is $35.2 < \tan\beta < 38$, while the range in the SSC region is $10.2 < \tan\beta < 38$. Note that the points shown in Fig. 14 are for all $\tan\beta$ within the aforementioned ranges. However, it can be concluded from Fig. 14 that the points with the same WIMP mass do exhibit the same characteristics as the points in the intersecting $D6$-brane model. For the same WIMP mass, the WMAP spectra have a larger annihilation cross-section, and hence, gamma-ray flux than the SSC points, due to the fact that in the WMAP region, we are not allowing for the $\mathcal{O}(10)$ dilution factor to $\Omega_{\chi^o}h^2$.

I. WIMP-Nucleon Direct Detection Cross-sections in Light of CDMS II

Recently the Cryogenic Dark Matter Search (CDMS) II experiment has announced what may be the first positive evidence for the direct detection of WIMP-like dark

matter [18], including the detection of two candidate events, although there is a 23% chance that these events could be due to background. We investigate regions of the intersecting $D6$-brane model parameter space that satisfy all the experimental constraints and possess WIMP-nucleon spin-independent cross-sections σ_{SI} that satisfy the latest CDMS II upper limit of $\sigma_{SI} = 3.8 \times 10^{-8}$ pb at a mass of 70 GeV/c^2. The results of [75] and this chapter indicate the regions of the parameter space we wish to target for WIMP-nucleon spin-independent cross-sections near the CDMS II upper limit are regions with low $m_{3/2}$ and high tanβ. Soft-supersymmetry breaking terms are generated using the equations given in [68, 69] and in this chapter. The soft terms are run down to the electroweak scale via the Renormalization Group Equations (RGEs) and the corresponding relic neutralino density calculated as in Chapter II. We use a top quark mass of $m_t = 173.1$ GeV [83]. The direct detection cross-sections are calculated using `MicrOMEGAs 2.1`. We employ the experimental constraints given in Chapter II.

We find the optimal cases that are consistent with the latest CDMS II data occur for $m_{3/2} = 500$ GeV and tan$\beta = 46$ - 50. The two cases for tan$\beta = 46$ and tan$\beta = 50$ are shown in Fig. 15, where the maximum WIMP-nucleon cross section is $\sigma_{SI} \approx 1 \times 10^{-8}$ pb for these two tanβ. The LSP for these cases is 99.5% bino. In addition to the latest data from the CDMS II experiment, the limits resulting from the previous ZEPLIN-III, XENON 10, and CDMS experiments are also delineated on the plot. For a gravitino mass $m_{3/2} < 500$ GeV, the LEP Higgs mass constraint of 114 GeV becomes too restrictive, hence, $m_{3/2} \approx 500$ GeV appears to be most favorable. The points near $\sigma_{SI} \approx 1 \times 10^{-8}$ pb reside in the WMAP 2σ relic density region, and these points generate the WMAP observed relic density through stau-neutralino coannihilation. The intersecting $D6$-brane model also possesses regions of the parameter space with chargino-neutralino coannihilation, and furthermore, both

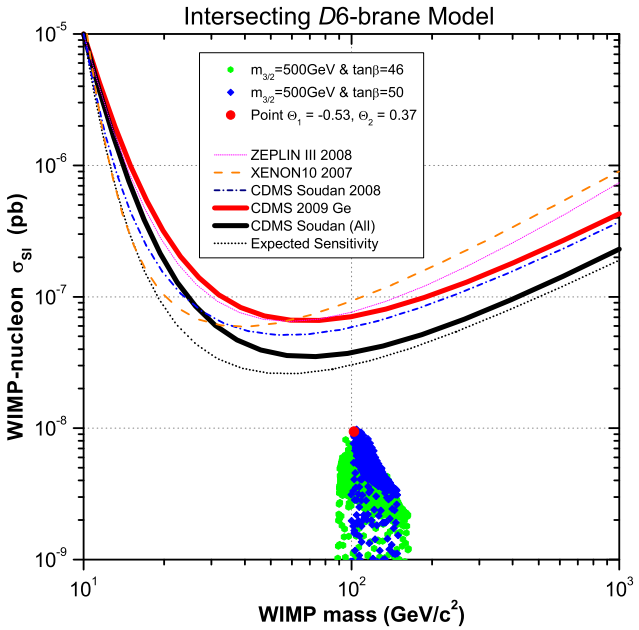

Fig. 15. Spin-independent WIMP-nucleon cross-sections of an intersecting $D6$-brane model. The two cases shown here are $m_{3/2} = 500$ GeV, $\tan\beta = 46$, and $m_{3/2} = 500$ GeV, $\tan\beta = 50$. Each marker satisfies all experimental constraints. The point detailed in Table XXI and Table XXII is annotated on the plot by the red point.

of these coannihilation regions can generate very small mass differences between the lightest SUSY particle (LSP) neutralino $\widetilde{\chi}_1^0$ and the next-to-lightest SUSY particle (NLSP), either the lightest chargino $\widetilde{\chi}_1^{\pm}$ or stau $\widetilde{\tau}_1$, and thus, a very small relic density. In this scenario, the neutralino can account for only a small portion of the overall composition of the total observed dark matter. The remaining fraction of the observed relic density in this situation would be composed of other particles, such as axions or crytpons, or additional astrophysical matter. In order to enable a direct comparison of Fig. 15 to the data from CDMS II and other direct-detection experiments, for those points in Fig. 15 with a relic density less than the observed WMAP 2σ data, we plot a modified WIMP-nucleon cross-section $\sigma_{SI} \times \frac{\Omega_\chi}{\Omega_{WMAP}}$.

The points in Fig. 15 with the largest WIMP-nucleon cross-section σ_{SI} possess

a WMAP 2σ relic density. The SUSY and Higgs spectrum for one of these typical points is shown in Table XXI and the low energy observables are given in Table XXII. This particular point lives in the stau-neutralino coannihilation region, as evidenced by the less than 15 GeV difference in mass between the LSP $\widetilde{\chi}_1^0$ and the NLSP $\widetilde{\tau}_1$. The lightest CP-even Higgs mass is just above the LEP constraint, and well within the discovery potential at LHC. The process with the largest production differential cross-section at LHC for this point is $q + \overline{q} \to \widetilde{\chi}_2^0 + \widetilde{\chi}_1^{\pm}$. The $\widetilde{\chi}_2^0$ and $\widetilde{\chi}_1^{\pm}$ are virtually degenerate, though the $\widetilde{\tau}_1^{\pm}$ is lighter than both the $\widetilde{\chi}_2^0$ and $\widetilde{\chi}_1^{\pm}$, so both the $\widetilde{\chi}_2^0$ and $\widetilde{\chi}_1^{\pm}$ will decay to $\widetilde{\tau}_1^{\pm}$ nearly 100% of the time. The second lightest neutralino will decay to tau through the decay chain $\widetilde{\chi}_2^0 \to \widetilde{\tau}_1^{\pm}\tau^{\mp} \to \tau^{\pm}\tau^{\mp}\widetilde{\chi}_1^0$, while the chargino will also decay to tau through $\widetilde{\chi}_1^{\pm} \to \widetilde{\tau}_1^{\pm}\nu \to \tau^{\pm}\nu\widetilde{\chi}_1^0$, so the end product of both decay chains for this point at LHC will be low energy tau. These points in the parameter space also satisfy all limits on other non-LHC observables such as the limit on the gamma-ray flux from neutralino annihilations. For further details on the LHC phenomenology of this model, see [69].

In light of the CDMS II results, we examine more closely the gamma-ray flux for the cases under study in this section. The gamma-ray flux Φ_γ for an intersecting $D6$-brane model is shown in Fig. 16, including the expected sensitivity of the Fermi experiment [12]. The gamma-ray flux is calculated using `MicrOMEGAs 2.1`. All regions of the experimentally allowed parameter space for $m_{3/2} = 500$ GeV, $\tan\beta = 46$ and $\tan\beta = 50$ are within the expected sensitivity of the Fermi telescope.

Table XXI. SUSY and Higgs spectrum for a typical point with $\sigma_{SI} \approx 1 \times 10^{-8}$ pb. Here, $m_{3/2} = 500$ GeV, $\tan\beta = 50$, $\Omega_\chi = 0.1113$, $\Theta_1 = -0.53$, and $\Theta_2 = 0.37$ (see [68] for a complete definition of these parameters). The GUT scale mass parameters for this point are $M3 = 490$ GeV, $M2 = 160$ GeV, $M1 = 256$ GeV, $m_H = 177$ GeV, $m_L = 446$ GeV, $m_R = 270$ GeV, $A_0 = 272$ GeV.

Sparticle	*Mass (GeV)*	*(S)particle*	*Mass (GeV)*
$\widetilde{\chi}_1^0$	102.2	$\widetilde{t}_1$	853.2
$\widetilde{\chi}_2^0$	120.1	$\widetilde{t}_2$	1010.1
$\widetilde{\chi}_3^0$	661.4	$\widetilde{u}_R$	1025.7
$\widetilde{\chi}_4^0$	664.1	$\widetilde{u}_L$	1083.5
$\widetilde{\chi}_1^\pm$	120.1	$\widetilde{b}_1$	928.1
$\widetilde{\chi}_2^\pm$	666.1	$\widetilde{b}_2$	1006.8
$\widetilde{\tau}_1$	116.5	$\widetilde{d}_R$	1025.9
$\widetilde{\tau}_2$	453.9	$\widetilde{d}_L$	1086.4
$\widetilde{e}_R$	287.3	$\widetilde{g}$	1140.8
$\widetilde{e}_L$	458.3	m_h	114.1
$\widetilde{\nu}_{e/\mu}$	451.5	m_A	447.9
$\widetilde{\nu}_\tau$	423.9	$m_{H^\pm}$	455.9

Table XXII. Low energy observables for the point $m_{3/2} = 500$ GeV, $\tan\beta = 50$, $\Omega_\chi = 0.1113$, $\Theta_1 = -0.53$, and $\Theta_2 = 0.37$ (see [68] for a complete definition of these parameters). The GUT scale mass parameters are $M3 = 490$ GeV, $M2 = 160$ GeV, $M1 = 256$ GeV, $m_H = 177$ GeV, $m_L = 446$ GeV, $m_R = 270$ GeV, $A_0 = 272$ GeV.

$g_\mu - 2$	$Br(b \to s\gamma)$	$Br(B_s^0 \to \mu^+\mu^-)$
41×10^{-10}	2.98×10^{-4}	5.3×10^{-8}

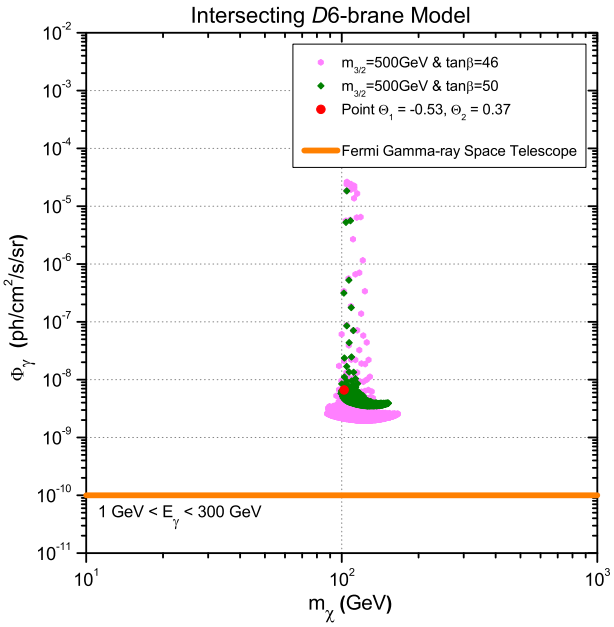

Fig. 16. Gamma-ray flux of an intersecting $D6$-brane model with the expected sensitivity of the Fermi Gamma-ray Space Telescope. The two cases shown here are $m_{3/2} = 500$ GeV, $\tan\beta = 46$, and $m_{3/2} = 500$ GeV, $\tan\beta = 50$. Each marker satisfies all experimental constraints. The point detailed in Table XXI and Table XXII is annotated on the plot by the red point.

CHAPTER IV

F-THEORY

A. F-Theory GUTs

The great challenge of string phenomenology is constructing realistic string models that allow us to make unique predictions that can be tested at the Large Hadron Collider (LHC), future International Linear Collider (ILC), and other experiments. If these predictions are confirmed in future experiments, we will possess strong evidence to support that string theory is indeed the correct fundamental description of nature. To the present, string phenomenology has been primarily concentrated on heterotic string theory and Type II string theories with D-branes, though unfortunately, this has not resulted in any unique predictions thus far.

Certainly, F-Theory model building and phenomenology have been studied extensively [84, 85, 86, 87, 88, 89, 90, 91, 92, 93, 94, 95, 96]. An exciting new feature is that $SU(5)$ gauge symmetry can be broken down to the SM gauge symmetry by turning on $U(1)_Y$ flux [97, 98, 94], and additionally, the $SO(10)$ gauge symmetry can be broken down to the $SU(5) \times U(1)_X$ and $SU(3) \times SU(2)_L \times SU(2)_R \times U(1)_{B-L}$ gauge symmetries by turning on the $U(1)_X$ and $U(1)_{B-L}$ fluxes, respectively [97, 98, 85, 93, 84, 94]. It is significant to note that realistic GUTs from F-theory can be constructed locally, hence, the next key question is whether a unique prediction can be made that can tested at LHC, ILC, and other future experiments.

To study the low energy phenomenology from F-theory GUTs previously, gauge mediated supersymmetry breaking was predominantly considered since the F-theory GUTs were constructed locally [87, 88]. However, to construct the realistic F-theory GUTs, these local GUTs must be embedded into a globally consistent framework [89,

90, 91, 92]. Consequently, here we study gravity mediated supersymmetry breaking. In F-theory $SU(5)$ and $SO(10)$ models where the gauge symmetries are broken down to the $SU(3) \times SU(2)_L \times U(1)_Y$ and $SU(3) \times SU(2)_L \times SU(2)_R \times U(1)_{B-L}$ gauge symmetries by turning on the $U(1)_Y$ and $U(1)_{B-L}$ fluxes, respectively, the exact gaugino mass relation (See Eq. (4.1) in the following) is obtained near the electroweak scale at one loop [99]. These F-theory GUTs are constructed locally, so we do not know the Kähler potential for the SM fermions and Higgs fields. For this reason, we cannot calculate the supersymmetry breaking scalar masses and trilinear soft terms. Interestingly, our gaugino mass relation can be preserved reasonably well at the low energy two-loop level if the scalar masses and trilinear soft terms are near the TeV scale. We must emphasize that our gaugino mass relation is different from those that have been studied thus far [100], and the gaugino masses can be measured at LHC and ILC [101, 102]. As a result, these F-theory GUTs can be tested at the colliders. Note that the generic scalar masses and trilinear soft terms will not affect our prediction on the gaugino mass relation at low energy, so we assume a universal scalar mass m_0 and universal trilinear soft term A_0 for simplicity. Examining two typical scenarios of gaugino masses, we present the viable parameter space which satisfies all the latest experimental constraints and is consistent with the CDMS II experiment [103]. In particular, the gaugino mass relation is in fact satisfied at two-loop level with only a very slight deviation at low energy.

B. Gaugino Mass Relation

Using the one-loop renormalization group equations (RGEs), we obtain the gaugino mass relation around the electroweak scale [99]

$$\frac{M_1}{\alpha_1} - \frac{M_3}{\alpha_3} = \frac{3}{5}\left(\frac{M_2}{\alpha_2} - \frac{M_3}{\alpha_3}\right) , \tag{4.1}$$

where α_3, α_2, and α_1 are the gauge couplings for the $SU(3)_C$, $SU(2)_L$, and $U(1)_Y$ gauge symmetries, respectively. Relation (4.1) was derived first, twenty-five years ago in ref [104] in the framework of an effective Supergravity theory. For further generalizations see [105] and references therein. A similar result was suggested in Ref. [96] during the preparation of this work. Furthermore, the gaugino mass relation in minimal Supergravity (mSUGRA) satisfies the above equation [100]. However, if $2(M_1\alpha_1^{-1} - M_3\alpha_3^{-1})/(M_1\alpha_1^{-1} + M_3\alpha_3^{-1})$ is quite small, our gaugino mass relation can definitely be distinguished from that of mSUGRA. Moreover, the gluino mass can be measured at the LHC [101] and the gaugino masses M_1 and M_2 can be determined at ILC [102]. Therefore, these F-theory GUTs can be tested at LHC and ILC.

To test the gaugino mass relation close to the electroweak scale, we define a parameter η as follows [99]

$$\eta \;=\; \frac{5\left(M_1\alpha_1^{-1} - M_3\alpha_3^{-1}\right)}{3\left(M_2\alpha_2^{-1} - M_3\alpha_3^{-1}\right)} \; . \tag{4.2}$$

Notice η is exactly one at the GUT scale. In addition, η is one around the electroweak scale from one-loop RGE running, yet η may deviate slightly from one as a result of two-loop RGE running.

For gaugino masses, we consider two typical scenarios [99]

(I) For Scenario I, the gaugino masses at the GUT scale are

$$\begin{aligned} M_3 \;&\simeq\; \alpha M_{1/2} \; , \;\; M_2 \;\simeq\; (\alpha+2)\, M_{1/2} \; , \\ M_1 \;&\simeq\; \left(\alpha + \frac{6}{5}\right) M_{1/2} \; , \end{aligned} \tag{4.3}$$

where $M_{1/2}$ is a mass parameter. In our numerical calculations, we will choose $\alpha = 3$.

(II) For Scenario II, the gaugino masses at the GUT scale are

$$M_3 \;\simeq\; (\gamma-\alpha)\, M_{1/2} \; , \;\; M_2 \;\simeq\; (\gamma-\alpha-2)\, M_{1/2} \; ,$$

$$M_1 \simeq \left(\gamma - \alpha - \frac{6}{5}\right) M_{1/2} \, . \tag{4.4}$$

In our numerical calculations, we choose $(\gamma - \alpha) = 5$. In summary, we have $M_3 < M_1 < M_2$ in scenario I and $M_2 < M_1 < M_3$ in scenario II.

C. F-Theory Low Energy Supersymmetry Phenomenology

We take $\mu > 0$, so we have four free parameters in our models: $M_{1/2}$, m_0, A_0, and $\tan\beta$, where $\tan\beta$ is the ratio of the Higgs vacuum expectation values. The soft terms are run down to the electroweak scale via the Renormalization Group Equations (RGEs) and the corresponding relic neutralino density calculated as in Chapter II. We use a top quark mass of $m_t = 173.1$ GeV [83]. The direct detection cross-sections are calculated using `MicrOMEGAs 2.1`. We employ the experimental constraints listed in Chapter II.

For scenario I, we commence with $M_{1/2}$, m_0, A_0, and $\tan\beta$ as free parameters, however, a comprehensive scan uncovers $A_0 = m_0$ as the most phenomenologically favored. As shown in Fig. 17, the experimentally allowed parameter space for $\tan\beta = 51$ after applying all these constraints consists of small $M_{1/2}$ and large m_0. We find from the viable parameter space in Fig. 18 that the lightest neutralino-nucleon direct-detection cross-section σ_{SI} is very close to the CDMS II upper limit. The constraints from previous ZEPLIN-III, XENON 10, and CDMS experiments are also delineated in Fig. 18. In these figures, we present our benchmark point as an orange point which has $\Omega_\chi = 0.1156$, $\sigma_{SI} = 6.15 \times 10^{-8}$ pb, and $m_{\widetilde{\chi}_1^0} = 316$ GeV. The SUSY and Higgs spectrum for this point is detailed in Table XXIII. In addition, we compute η at the electroweak scale, and find that the deviation of η from one is very small, about 1.009% - 1.014%, as shown in Fig. 19.

For scenario II, with $A_0 = m_0$ and $\tan\beta = 27$, we present the experimentally

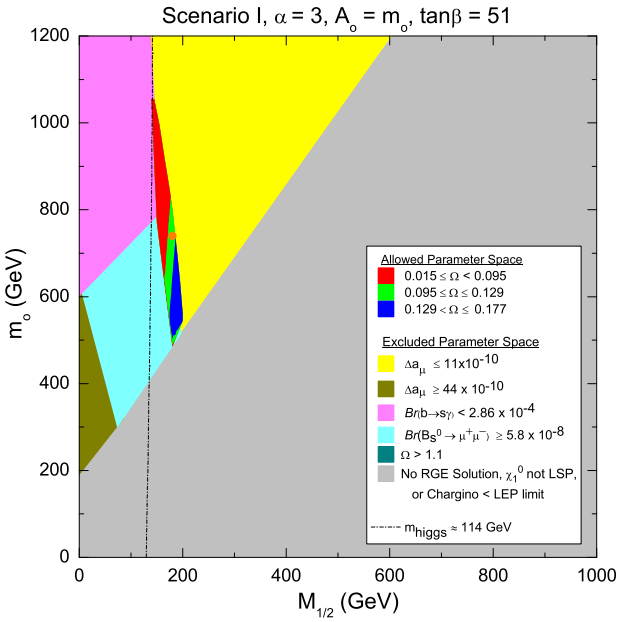

Fig. 17. Experimentally allowed parameter space for Scenario I, $\alpha = 3$, $A_0 = m_0$, tanβ = 51. The benchmark point detailed in Table XXIII is annotated on the plot by the orange point.

allowed region in the m_0 and $M_{1/2}$ plane in Fig. 20. For the viable parameter space, we obtain that the lightest neutralino-nucleon direct-detection cross-section σ_{SI} is about 2×10^{-8} pb. This is also consistent with the CDMS II experiment due to the uncertainties of the QCD effects. Moreover, we find that at the electroweak scale the deviation of η from one is also very small, about 1.02% to 1.035%, as depicted in Fig. 21. Similarly, the orange point is our benchmark point which has $\Omega_\chi = 0.107$, $\sigma_{SI} = 2.03 \times 10^{-8}$ pb, and $m_{\widetilde{\chi}_1^0} = 170$ GeV. The SUSY and Higgs spectrum for this benchmark point is detailed in Table XXIV.

The five lightest SUSY particles for the $\alpha = 3$ and tan$\beta = 51$ benchmark point, including the heavy Higgs, are $\widetilde{\chi}_1^0 < A < H^\pm < \widetilde{\chi}_1^\pm < \widetilde{\chi}_2^0$. The production of squarks $\widetilde{q}$ and gluinos $\widetilde{g}$ have the largest differential cross-sections at LHC, and what's more, the $\widetilde{g}$ will produce sbottoms $\widetilde{b}$ and stops $\widetilde{t}$ with the $\widetilde{q}$ decaying to neutralinos and

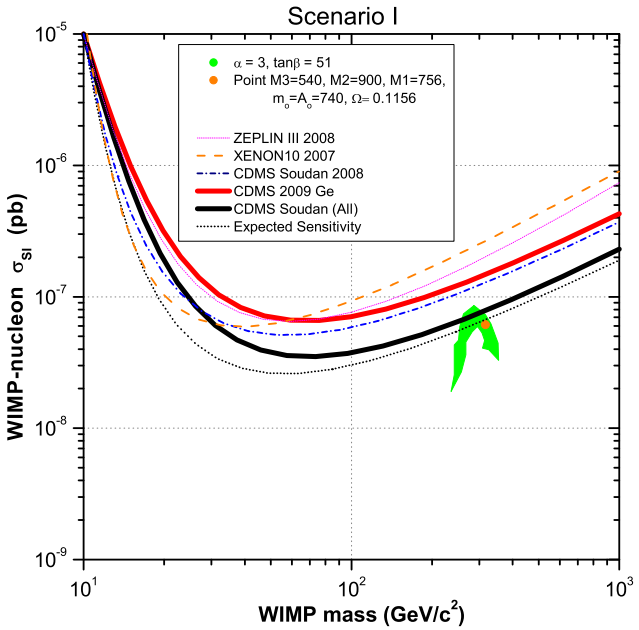

Fig. 18. Spin-independent lightest neutralino-nucleon cross-sections for Scenario I, $\alpha = 3$, $A_0 = m_0$, $\tan\beta = 51$. The green shaded region satisfies all experimental constraints. The point detailed in Table XXIII is annotated on the plot by the orange point.

charginos. The $\widetilde{b}$ and $\widetilde{t}$ decay to the top quark t, bottom quark b, neutralinos, and charginos. Additionally, we will get b quarks from $\widetilde{\chi}_2^0$ through light Higgs in the process $\widetilde{\chi}_2^0 \rightarrow h_0\widetilde{\chi}_1^0$ with a branching ratio of 93%. These light Higgs will in turn decay to $b\bar{b}$ with a 73% branching ratio. Leptons and hadronic jets will result from the decay $\widetilde{\chi}_1^{\pm} \rightarrow W^{\pm}\widetilde{\chi}_1^0$, where this is the only kinematically allowed $\widetilde{\chi}_1^{\pm}$ process. Due to the less massive nature of the heavy Higgs particles, the $q + \overline{q}$ reaction will provide some neutral heavy Higgs A that will decay to $b\bar{b}$ pairs 87% of the time, while the heavy charged Higgs $H^{\pm}$ will produce $\bar{b}t$ or $b\bar{t}$ pairs 84% of the time, with $t \rightarrow W^+b$. Thus, this benchmark point will produce mainly light Higgs h_0, b quarks, and W bosons at LHC. We calculate the differential cross-sections and branching ratios with `PYTHIA 6.4`, using `SuSpect 2.34` to compute the sparticle masses.

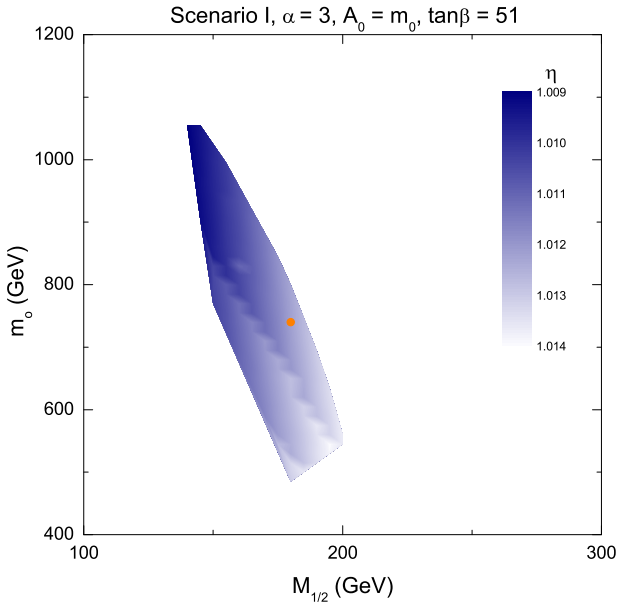

Fig. 19. Plot of η for Scenario I. The shaded regions satisfy all experimental constraints. The point detailed in Table XXIII is annotated on the plot by the orange point.

In addition to the viable parameter space of Scenario I, Scenario II can also generate a well constrained region at the relic densities we consider here. We see from the SUSY and Higgs spectrum in Table XXIV the small mass difference of 10 GeV between the LSP $\widetilde{\chi}_1^0$ and next-to-lightest SUSY particle (NLSP) $\widetilde{\tau}_1^{\pm}$. This is similar to what's referred to as the stau-neutralino coannihilation region in mSUGRA since early universe neutralinos can annihilate with stau, producing low energy tau. Hence, we expect this point to produce LHC physics similar to the stau-neutralino coannihilation region of mSUGRA. Moreover, the LSP for this point is 99.7% bino. A close examination of this $\gamma - \alpha = 5$ point reveals $\widetilde{\chi}_2^0 \rightarrow \widetilde{\tau}_1^{\mp}\tau^{\pm} \rightarrow \tau^{\mp}\tau^{\pm}\widetilde{\chi}_1^0$ as the dominant decay, therefore, we would expect opposite sign tau pair to be characteristic of this point at LHC.

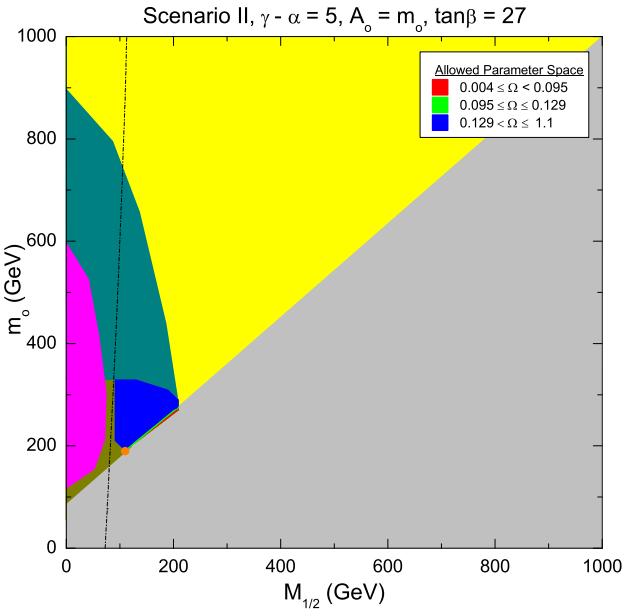

Fig. 20. Experimentally allowed parameter space for Scenario II, $\gamma - \alpha = 5, A_0 = m_0$, $\tan\beta = 27$. The benchmark point detailed in Table XXIV is annotated on the plot by the orange point. Identification of the excluded regions is shown in the chart legend in Fig. 17.

Table XXIII. SUSY and Higgs spectrum for a Scenario I, $\alpha = 3$ benchmark point with $\sigma_{SI} = 6.15 \times 10^{-8}$ pb. Here, $\tan\beta = 51$ and $\Omega_\chi = 0.1156$. The GUT scale mass parameters for this point are (in Gev) $m_{1/2} = 180$, $M3 = 540$, $M2 = 900$, $M1 = 756$, $m_0 = A_0 = 740$.

Sparticle	*Mass (GeV)*	*(S)particle*	*Mass (GeV)*
$\widetilde{\chi}_1^0$	316	$\widetilde{t}_1$	973
$\widetilde{\chi}_2^0$	477	$\widetilde{t}_2$	1201
$\widetilde{\chi}_3^0$	487	$\widetilde{u}_R$	1302
$\widetilde{\chi}_4^0$	743	$\widetilde{u}_L$	1402
$\widetilde{\chi}_1^\pm$	473	$\widetilde{b}_1$	1103
$\widetilde{\chi}_2^\pm$	743	$\widetilde{b}_2$	1195
$\widetilde{\tau}_1$	489	$\widetilde{d}_R$	1294
$\widetilde{\tau}_2$	843	$\widetilde{d}_L$	1404
$\widetilde{e}_R$	790	$\widetilde{g}$	1263
$\widetilde{e}_L$	946	m_h	115.4
$\widetilde{\nu}_{e/\mu}$	942	m_A	465
$\widetilde{\nu}_\tau$	837	$m_{H^\pm}$	473

Table XXIV. SUSY and Higgs spectrum for a Scenario II, $\alpha - \gamma = 5$ benchmark point with $\sigma_{SI} = 2.03 \times 10^{-8}$ pb. Here, $\tan\beta = 27$ and $\Omega_\chi = 0.107$. The GUT scale mass parameters for this point are (in Gev) $m_{1/2} = 110$, $M3 = 550$, $M2 = 330$, $M1 = 418$, $m_0 = A_0 = 190$.

Sparticle	*Mass (GeV)*	*(S)particle*	*Mass (GeV)*
$\widetilde{\chi}_1^0$	102.2	$\widetilde{t}_1$	853.2
$\widetilde{\chi}_2^0$	120.1	$\widetilde{t}_2$	1010.1
$\widetilde{\chi}_3^0$	661.4	$\widetilde{u}_R$	1025.7
$\widetilde{\chi}_4^0$	664.1	$\widetilde{u}_L$	1083.5
$\widetilde{\chi}_1^\pm$	120.1	$\widetilde{b}_1$	928.1
$\widetilde{\chi}_2^\pm$	666.1	$\widetilde{b}_2$	1006.8
$\widetilde{\tau}_1$	116.5	$\widetilde{d}_R$	1025.9
$\widetilde{\tau}_2$	453.9	$\widetilde{d}_L$	1086.4
$\widetilde{e}_R$	287.3	$\widetilde{g}$	1140.8
$\widetilde{e}_L$	458.3	m_h	114.1
$\widetilde{\nu}_{e/\mu}$	451.5	m_A	447.9
$\widetilde{\nu}_\tau$	423.9	$m_{H^\pm}$	455.9

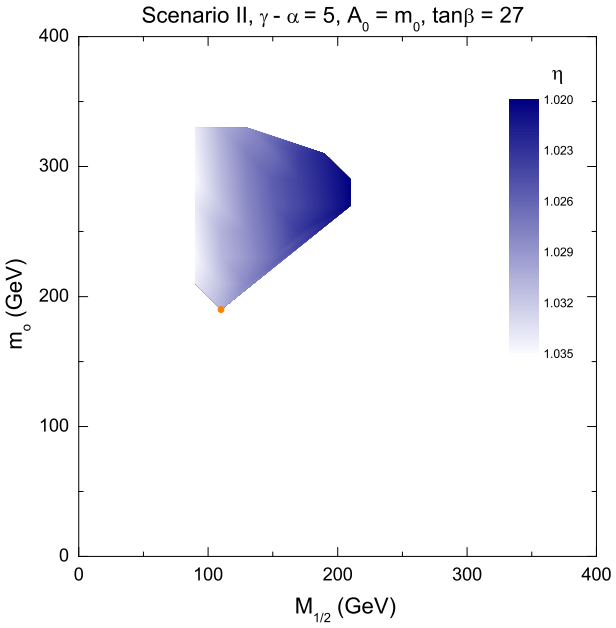

Fig. 21. Plot of η for Scenario II. The shaded regions satisfy all experimental constraints. The point detailed in Table XXIV is annotated on the plot by the orange point.

CHAPTER V

FLIPPED F-SU(5)

A. $\mathcal{F}$-$SU(5)$

We can break the $SO(10)$ gauge symmetry down to the flipped $SU(5) \times U(1)_X$ gauge symmetry by turning on the $U(1)_X$ flux. The flipped $SU(5) \times U(1)_X$ models with TeV scale vector-like particles [106], which have been dubbed "$\mathcal{F}$-$SU(5)$", have been constructed systematically in F-theory [85, 93]. In $\mathcal{F}$-$SU(5)$, the $SU(3)_C \times SU(2)_L$ gauge symmetries are unified at about 10^{16} GeV, and the $SU(5) \times U(1)_X$ gauge symmetries are unified above 10^{17} GeV. On top of this, the TeV scale vector-like particles are potentially observable at the Large Hadron Collider (LHC), the lightest CP-even Higgs boson mass can be lifted [107], and the predicted proton decay [108, 109, 95, 110] is within the reach of the future Hyper-Kamiokande [111] and Deep Underground Science and Engineering Laboratory (DUSEL) [112] experiments.

Although the gaugino masses are not unified at the traditional GUT scale, we still have the same gaugino mass relation at the electroweak scale as the minimal supergravity (mSUGRA) scenario at one loop [113]. We also introduce two parameters testable at the colliders to measure the small two-loop deviations from the mSUGRA gaugino mass relations at the electroweak scale. Next, we incorporate TeV scale vector particles and generate regions of the parameter space that can satisfy all current experimental constraints and are consistent with the CDMS II experiment. In addition, we compute the annihilation cross-section of two neutralinos into two gamma-rays and evaluate the results in light of the first published Fermi-LAT measurement. Then we compute the new parameters to measure the two-loop deviations for both $\mathcal{F}$-$SU(5)$ and mSUGRA. We find that the deviations from the mSUGRA

gaugino mass relation in mSUGRA are smaller than 5%, while the deviations in the $\mathcal{F}$-$SU(5)$ are larger as a result of the TeV scale vector-like particles. An analytical comparison of the deviation between mSUGRA and $\mathcal{F}$-$SU(5)$ is illustrated. Next, the expected observable final states at the LHC are given for the viable regions of the parameter space.

B. Gaugino Mass Relation

In flipped $SU(5) \times U(1)_X$ models, the $SU(3)_C \times SU(2)_L$ gauge couplings are first joined at the scale M_{32}, and the $SU(5)$ and $U(1)_X$ gauge couplings are subsequently unified at the higher scale M_U. To separate the M_{32} and M_U scales and obtain true string-scale gauge coupling unification, we introduce vector-like particles which form complete flipped $SU(5) \times U(1)_X$ multiplets. We can only introduce the following two sets of vector-like particles around the TeV scale [106]

$$Z1 : XF = (\mathbf{10}, \mathbf{1}) \ , \ \overline{XF} = (\overline{\mathbf{10}}, -\mathbf{1}) \ ; \tag{5.1}$$

$$Z2 : XF \ , \ \overline{XF} \ , \ Xl = (\mathbf{1}, -\mathbf{5}) \ , \ \overline{Xl} = (\mathbf{1}, \mathbf{5}) \ . \tag{5.2}$$

For notational simplicity, we define the flipped $SU(5) \times U(1)_X$ models with $Z1$ and $Z2$ sets of vector-like particles as Type I and Type II flipped $SU(5) \times U(1)_X$ models, respectively. We choose to focus in this paper on the Type II model, although results are similar in most regards for Type I. We emphasize that the Type I and II flipped $SU(5) \times U(1)_X$ models have been constructed consistently from F-theory in Refs. [85, 93].

The gaugino mass relation from the scale M_U down to the scale M_{32} is [105]

$$\frac{M_5}{\alpha_5} \ = \ \frac{M_{1X}}{\alpha_{1X}} \ , \tag{5.3}$$

where M_5 and M_{1X} are gaugino masses for $SU(5)$ and $U(1)_X$ respectively, and α_5 and α_{1X} are the $SU(5)$ and $U(1)_X$ gauge couplings. This gaugino mass relation is renormalization scale invariant under one-loop renormalization group equation (RGE) running.

The gaugino mass M_1 for $U(1)_Y$ at the scale M_{32} is [114]

$$\frac{M_1}{\alpha_1} \equiv \frac{24}{25}\frac{M_{1X}}{\alpha_{1X}} + \frac{1}{25}\frac{M_5}{\alpha_5} , \tag{5.4}$$

where $\alpha_1 \equiv 5\alpha_Y/3$ is the $U(1)_Y$ gauge coupling. With Eq. (5.3), we obtain at the scale M_{32}

$$\frac{M_1}{\alpha_1} = \frac{M_5}{\alpha_5} . \tag{5.5}$$

Note that the gauge couplings α_1 and α_5 are split, and thus we do not have universal gaugino masses at the usual GUT scale. Applying RGE running, we obtain the gaugino mass relation which is valid from the scale M_{32} down to the electroweak scale at one loop [105]

$$\frac{M_3}{\alpha_3} = \frac{M_2}{\alpha_2} = \frac{M_1}{\alpha_1} , \tag{5.6}$$

where α_3 and α_2 are couplings of the $SU(3)_C$ and $SU(2)_L$ gauge symmetries respectively, and M_3 and M_2 are masses of the $SU(3)_C$ and $SU(2)_L$ gauginos. This gaugino mass relation is the same as that in mSUGRA [113]. The gaugino masses can be measured at the LHC and future ILC [101, 102], hence, we can test this relation at future experiments.

Considering two-loop RGE running, we will have a small deviation for the gaugino mass relation given by Eq. (5.6). To quantify the deviations, we first define

$$\left(\frac{M_i}{\alpha_i}\right)_{\rm L} \equiv \text{maximum}\left[\frac{M_3}{\alpha_3}, \frac{M_2}{\alpha_2}, \frac{M_1}{\alpha_1}\right] ,$$

$$\left(\frac{M_i}{\alpha_i}\right)_{\rm M} \equiv \text{median}\left[\frac{M_3}{\alpha_3},\ \frac{M_2}{\alpha_2},\ \frac{M_1}{\alpha_1}\right] ,$$
$$\left(\frac{M_i}{\alpha_i}\right)_{\rm S} \equiv \text{minimum}\left[\frac{M_3}{\alpha_3},\ \frac{M_2}{\alpha_2},\ \frac{M_1}{\alpha_1}\right] . \tag{5.7}$$

Then, we define the small deviations as follows

$$\delta_+ = \frac{\left(\frac{M_i}{\alpha_i}\right)_{\rm L} - \left(\frac{M_i}{\alpha_i}\right)_{\rm M}}{\left(\frac{M_i}{\alpha_i}\right)_{\rm M}} , \quad \delta_- = \frac{\left(\frac{M_i}{\alpha_i}\right)_{\rm S} - \left(\frac{M_i}{\alpha_i}\right)_{\rm M}}{\left(\frac{M_i}{\alpha_i}\right)_{\rm M}} . \tag{5.8}$$

We emphasize that $\delta_+ \geq 0$ and $\delta_+ \leq 0$. In other words, we have

$$\left(\frac{M_i}{\alpha_i}\right)_{\rm L} : \left(\frac{M_i}{\alpha_i}\right)_{\rm M} : \left(\frac{M_i}{\alpha_i}\right)_{\rm S} = (1+\delta_+) : 1 : (1+\delta_-) . \tag{5.9}$$

For example, in $\mathcal{F}$-$SU(5)$ we have

$$\left(\frac{M_i}{\alpha_i}\right)_{\rm L} = \frac{M_3}{\alpha_3} , \quad \left(\frac{M_i}{\alpha_i}\right)_{\rm M} = \frac{M_2}{\alpha_2} , \quad \left(\frac{M_i}{\alpha_i}\right)_{\rm S} = \frac{M_1}{\alpha_1} . \tag{5.10}$$

C. Low Energy Supersymmetry Phenomenology

The $\mathcal{F}$-$SU(5)$ type models have been constructed locally in F-theory [85, 93], and thus we do not know the Kähler potential for the SM fermions and Higgs fields and cannot calculate the supersymmetry breaking scalar masses and trilinear soft terms. Interestingly, as long as the scalar masses and trilinear soft terms are around the TeV scale, the gaugino mass relation can be preserved very well at low energy to two loops. For simplicity, in this paper, we consider the universal scalar mass m_0 and the universal trilinear soft term A_0. Essentially speaking, we study the F-theory inspired low energy supersymmetry phenomenology, so that we have four free parameters in our model: M_5, m_0, A_0, and $\tan\beta$, where $\tan\beta = \langle H_u\rangle/\langle H_d\rangle$, the ratio of the vacuum expectation values of the Higgs scalar fields. In addition, we must choose the sign of μ. We take $\mu > 0$, as suggested by the results of $g_\mu - 2$ for the muon. We also assume that the masses for the vector-like particles are universal, at 1 TeV. The contributions

to the beta functions of the SM gauge couplings from the vector-like particles must be accounted for in the one-loop and two-loop gauge coupling RGEs when running the soft terms down to the electroweak scale. We alter the one-loop and two-loop gauge coupling RGE code in `SuSpect 2.34` to realize the beta function corrections. In an effort to minimize the complexity of revising the code, we use only the one-loop RGEs for the SM fermion Yukawa couplings and supersymmetry breaking soft terms. The Yukawa coupling RGEs contribute to the gauge coupling RGEs at second order, so it is consistent to run only the Yukawa coupling RGEs at one-loop. However, for future investigations of GUTs with vector-like particles, we intend to extend our analysis to include two-loop RGEs for all supersymmetry breaking terms. Next, we modify the one-loop gaugino mass RGEs to include the strong coupling effects of the vector-like particles. Finally, the `SuSpect 2.34` code must be revised to require gauge coupling unification at $g_2 = g_3$, rather than the default unification configuration of $g_1 = g_2$. This necessitates lowering the ceiling on the running of the gauge couplings at high scale due to large effects on g_2 at scales above 10^{18} GeV. We see in Fig. 22 the split in unification at the M_{32} scale, as explained in the previous section. Below 1 TeV, there is only the running of the SM gauge couplings, which are shown as the red dotted lines in Fig. 22 for an unflipped $SU(5)$ point with universal gaugino masses, however, at 1 TeV and higher energies, we see the effects of the vector-like particles on the running of the couplings and masses. The relic LSP neutralino density and WIMP-nucleon direct detection cross-sections are computed with `MicrOMEGAs 2.1`, although the `MicrOMEGAs 2.1` code must also be reworked to include the revised RGEs. We use `SuSpect 2.34` as the RGE code in our relic density and WIMP-nucleon cross-section computations, and hence we implement the revised `SuSpect 2.34` RGEs in `MicrOMEGAs 2.1` as well. Supersymmetry breaking soft terms for the present model are generated using the gaugino mass relation in Eq. (5.5) at the scale M_{32}. The

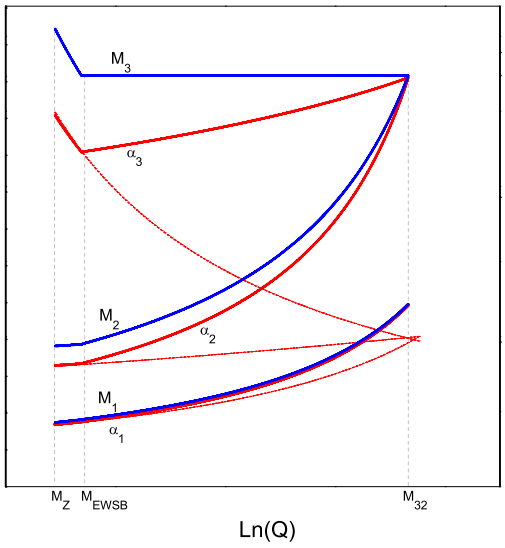

Fig. 22. Running of the $\mathcal{F}$-$SU(5)$ gaugino masses and gauge couplings from the M_Z scale to the M_{32} partial unification scale. The red dotted line represents the running of the gauge couplings for unflipped $SU(5)$ with universal gaugino masses at M_{GUT}. We suppress labeling of the vertical axes to preserve general heuristic applicability to the full parameter space considered.

gaugino mass M_1 is dependent upon the ratio of the unification scale gauge couplings α_1 and α_5, therefore, an iterative procedure must first be used to determine the final value of M_1 before any low energy phenomenology can be investigated. We use a top quark mass of $m_t = 173.1$ GeV [83] and employ the experimental constraints from Chapter II.

We commence with M_5, m_0, A_0, and $\tan\beta$ as free parameters, however, for simplicity we take $A_0 = m_0$. A comprehensive scan of the entire parameter space uncovers $\tan\beta = 51$ as most consistent with the WMAP relic density observations and latest CDMS II results. As shown in Fig. 23, the experimentally allowed parameter space for $\tan\beta = 51$ after applying all these constraints consists of two segregated small regions. We look to examine more closely those regions of the experimentally

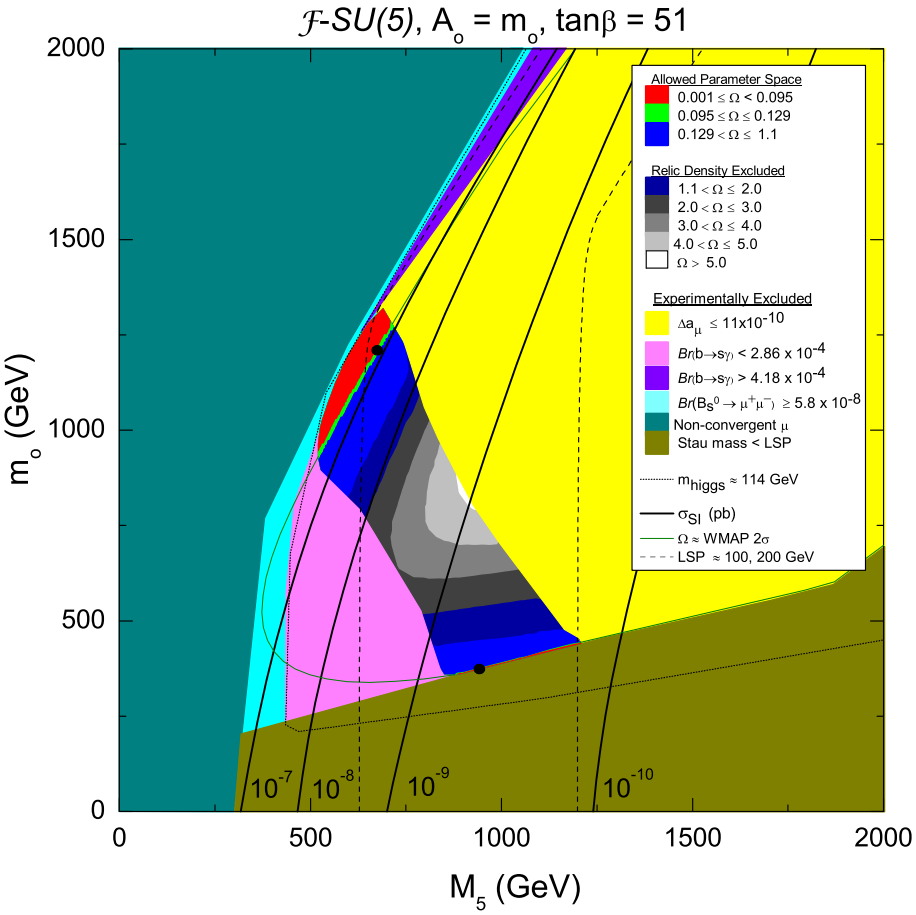

Fig. 23. $\mathcal{F}$-$SU(5)$ experimentally allowed parameter space for $\tan\beta = 51$, $A_0 = m_0$. The benchmark points detailed in Table XXV and Table XXVI are annotated by the black points. The solid black lines demarcate the WIMP-nucleon spin-independent cross-sections. The dotted line indicates the LEP boundary for the light Higgs. The two dashed lines represent an LSP mass of 100 GeV and 200 GeV. The dark green line denotes the region satisfying the WMAP 2σ relic density, however, only the bright green region within the designated allowed parameter space can fulfill all the experimental constraints.

allowed parameter space that comply with the recent CDMS II data and the WMAP relic density observations. This encompasses the narrow WMAP strip in both experimentally allowed regions, so we choose points from each allowed region within these narrow WMAP strips as our benchmark points for analysis. In fact, with relic densities of $\Omega_\chi = 0.1093$ and $\Omega_\chi = 0.1151$, these benchmark points additionally satisfy the very constrained WMAP 7-year [115] results. Inspecting the sparticle and Higgs spectrum for our benchmark point in Table XXV with relic density $\Omega_\chi = 0.1093$ reveals that the additional contribution of the 1 TeV vector-like particles lower the gluino mass quite dramatically. The gaugino mass M_3 runs flat from the M_{32} unification scale to the electroweak scale as shown in Fig. 22, though, due to SUSY radiative corrections, the physical gluino mass is larger than M_3 at the M_{32} scale. This is true for all regions of the $\mathcal{F}$-$SU(5)$ parameter space. In mSUGRA, the focus point region consists of large m_0 where the WMAP observed relic density can be satisfied with a mixed Bino-Higgsino state in the LSP due to a small $|\mu|$, leading to enhanced $\widetilde{\chi}_1^0\widetilde{\chi}_1^0$ annihilation. However, even though m_0 is reasonably large for the Table XXV benchmark point, here the LSP is 99% Bino for $\mathcal{F}$-$SU(5)$. In contrast, the sparticle and Higgs spectrum for our benchmark point in Table XXVI illustrates that the WMAP relic density $\Omega_\chi = 0.1151$ is generated through stau-neutralino coannihilation. This is demonstrated by the near degenerate mass between the $\widetilde{\chi}_1^0$ neutralino LSP and $\widetilde{\tau}_1$ stau next-to-lightest supersymmetric particle (NLSP). Accordingly, the LSP for the benchmark point in Table XXVI is 99.9% bino.

The WIMP-nucleon direct-detection cross-sections σ_{SI} depicted in Fig. 24 underscore the fact that the case of $\tan\beta = 51$ produces WIMPs with σ_{SI} that comply with the CDMS II upper limits, with our benchmark point in Table XXV at $\sigma_{SI} = 1.4 \times 10^{-7}$ pb and $m_{\widetilde{\chi}_1^0} = 107$ GeV, and the benchmark point in Table XXVI at $\sigma_{SI} = 5.4 \times 10^{-10}$ pb and $m_{\widetilde{\chi}_1^0} = 152$ GeV. The constraints from previous ZEPLIN-III,

Table XXV. Sparticle and Higgs spectrum for the $M_5 = 670$ GeV and $m_0 = 1215$ GeV benchmark point illustrated in Fig. 23. Here, $\tan\beta = 51$, $\Omega_\chi = 0.1093$, $\sigma_{SI} = 1.4 \times 10^{-7}$ pb, and $\langle\sigma v\rangle_{\gamma\gamma} = 2.0 \times 10^{-26}\ cm^3/s$. The GUT-scale mass parameters for this point are (in GeV) $M_3 = 670$, $M_2 = 670$, $M_1 = 296$, $A_0 = m_0 = 1215$.

Sparticle	Mass (GeV)	Sparticle	Mass (GeV)
$\widetilde{\chi}_1^0$	107	$\widetilde{t}_1$	1206
$\widetilde{\chi}_2^0$	224	$\widetilde{t}_2$	1359
$\widetilde{\chi}_3^0$	337	$\widetilde{b}_1$	1341
$\widetilde{\chi}_4^0$	363	$\widetilde{b}_2$	1374
$\widetilde{\chi}_1^\pm$	223	$\widetilde{u}_R$	1627
$\widetilde{\chi}_2^\pm$	363	$\widetilde{u}_L$	1670
$\widetilde{\tau}_1$	822	$\widetilde{d}_R$	1626
$\widetilde{\tau}_2$	1107	$\widetilde{d}_L$	1672
$\widetilde{e}_R$	1221	$\widetilde{g}$	817
$\widetilde{e}_L$	1276	m_h	116.6
$\widetilde{\nu}_{e/\mu}$	1274	$m_{H,A}$	337
$\widetilde{\nu}_\tau$	1103	$m_{H^\pm}$	349

Table XXVI. Sparticle and Higgs spectrum for the $M_5 = 925$ GeV and $m_0 = 375$ GeV benchmark point illustrated in Fig. 23. Here, $\tan\beta = 51$, $\Omega_\chi = 0.1151$, $\sigma_{SI} = 5.4 \times 10^{-10}$ pb, and $\langle\sigma v\rangle_{\gamma\gamma} = 1.1 \times 10^{-27}\ cm^3/s$. The GUT-scale mass parameters for this point are (in GeV) $M_3 = 925$, $M_2 = 925$, $M_1 = 418$, $A_0 = m_0 = 375$.

Sparticle	Mass (GeV)	Sparticle	Mass (GeV)
$\widetilde{\chi}_1^0$	152	$\widetilde{t}_1$	1122
$\widetilde{\chi}_2^0$	336	$\widetilde{t}_2$	1375
$\widetilde{\chi}_3^0$	1027	$\widetilde{b}_1$	1289
$\widetilde{\chi}_4^0$	1030	$\widetilde{b}_2$	1378
$\widetilde{\chi}_1^\pm$	336	$\widetilde{u}_R$	1523
$\widetilde{\chi}_2^\pm$	1031	$\widetilde{u}_L$	1609
$\widetilde{\tau}_1$	168	$\widetilde{d}_R$	1521
$\widetilde{\tau}_2$	634	$\widetilde{d}_L$	1611
$\widetilde{e}_R$	408	$\widetilde{g}$	1060
$\widetilde{e}_L$	656	m_h	118.3
$\widetilde{\nu}_{e/\mu}$	651	$m_{H,A}$	732
$\widetilde{\nu}_\tau$	607	$m_{H^\pm}$	737

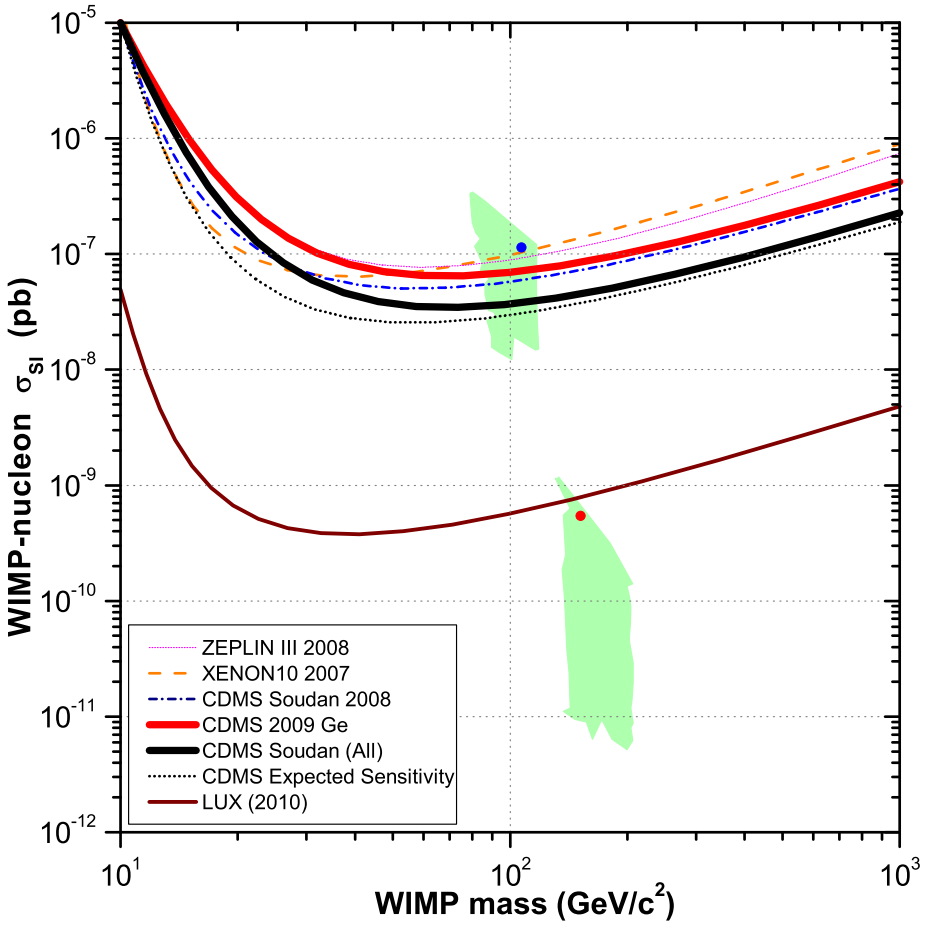

Fig. 24. $\mathcal{F}$-$SU(5)$ spin-independent WIMP-nucleon cross-sections for $\tan\beta = 51$, $A_0 = m_0$, overlaid with direct-detection limits from recent and forthcoming experiments. The shaded regions satisfy all experimental constraints. The benchmark point in Table XXV is annotated by the blue point, while the benchmark point in Table XXVI is annotated by the red point.

XENON 10, and CDMS experiments are also delineated on the plot, in addition to the forthcoming LUX experiment [11]. Despite the fact the WIMP-nucleon cross-section of our Table XXV benchmark point in Fig. 24 is above the CDMS II upper limit, experimental uncertainties and QCD corrections can account for this variation. On the contrary, the entire region of the experimentally allowed parameter space with large M_5 and small m_0 has WIMP-nucleon cross-sections less than the recent CDMS II upper limits. The present model also possesses regions of the parameter space where the neutralino can account for only a small portion of the overall composition of the total observed dark matter. The remaining fraction of the observed relic density in this situation would be composed of other particles, such as axions or cryptons, or additional astrophysical matter. In order to enable a direct comparison of Fig. 24 to the data from CDMS II and other direct-detection experiments, for those points in Fig. 24 with a relic density less than the observed WMAP 2σ data, we plot a modified WIMP-nucleon cross-section $\sigma_{SI} \times \frac{\Omega_\chi}{\Omega_{WMAP}}$.

Indirect detection experiments search for high energy neutrinos, gamma-rays, positrons, and anti-protons emanating from neutralino annihilation in the galactic halo and core, or in the case of neutrinos, in the core of the sun or the earth. Here, we focus on the annihilation cross-section $\langle \sigma v \rangle_{\gamma\gamma}$ of two neutralinos into two gamma-rays in the galactic core or halo. Two possible decay channels where WIMPs can produce gamma-rays in the galactic core and halo are $\widetilde{\chi}_1^0 \widetilde{\chi}_1^0 \rightarrow \gamma\gamma$ and $\widetilde{\chi}_1^0 \widetilde{\chi}_1^0 \rightarrow q\overline{q} \rightarrow \pi^0 \rightarrow \gamma\gamma$. One such current experiment to measure the debris from WIMP annihilations is Fermi-LAT (formerly GLAST) [12], with new constraints on cross-sections of neutralino annihilations into two gamma-rays [13]. Figure 25 shows that the Fermi-LAT sensitivity has reached the $\mathcal{F}$-$SU(5)$ parameter space. The $\mathcal{F}$-$SU(5)$ cross-sections $\langle \sigma v \rangle_{\gamma\gamma}$ in Figure 25 are calculated using the modified `MicrOMEGAs 2.1` code to include the effects of the 1 TeV vector multiplet in `SuSpect 2.34`. The Fermi-

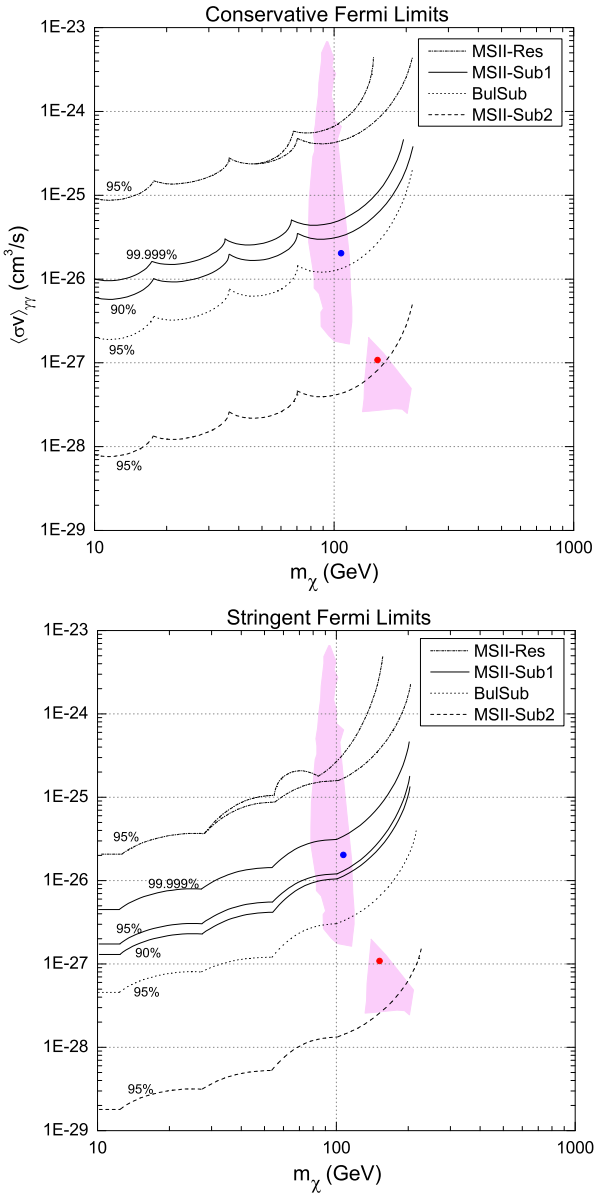

Fig. 25. $\mathcal{F}$-$SU(5)$ annihilation cross-section $\langle \sigma v \rangle_{\gamma\gamma}$ of two neutralinos into two gamma-rays for $\tan\beta = 51$, $A_0 = m_0$, overlaid with the most recent Fermi-LAT constraints. The shaded regions satisfy all experimental constraints. The benchmark point in Table XXV is annotated by the blue points, while the benchmark point in Table XXVI is annotated by the red points. For detailed explanations of the four dark matter scenarios (MSII-Res, MSII-Sub1, MSI-I-Sub2, BulSub), upper limits (conservative, stringent), and confidence limits (90%, 95%, 99.999%), we refer the reader to [13].

LAT collaboration applies four dark matter structure evolution scenarios (MSII-Res, MSII-Sub1, MSII-Sub2 and BulSub), which we overlay onto the $\mathcal{F}$-$SU(5)$ parameter space in Figure 25, as well as conservative and stringent upper limits on $\langle\sigma v\rangle$. For thorough descriptions of these four dark matter scenarios and upper limits, we refer the reader to [13]. Additionally, the upper 95% confidence limits for each of the four dark matter scenarios as determined by the Fermi-LAT collaboration are identified in Figure 25, including the 90% and 99.999% confidence limits for the Fermi-LAT reference model MSII-Sub1. For the benchmark point in Table XXV, $\langle\sigma v\rangle_{\gamma\gamma} = 2.0 \times 10^{-26}\ cm^3/s$, in the very near proximity of the Fermi-LAT reference model MSII-Sub1 upper limits for both the conservative and stringent cases, whilst for the benchmark point in Table XXVI, $\langle\sigma v\rangle_{\gamma\gamma} = 1.1 \times 10^{-27}\ cm^3/s$, well below the Fermi-LAT reference model MSII-Sub1 upper limits.

In the preceding section, we introduced the δ_+ and δ_- parameters of Eq. (5.8) in order to quantify the small two-loop deviations from the mSUGRA gaugino mass relations in Eq. (5.6) at the electroweak scale. The gaugino masses can be measured at the LHC and ILC [101, 102], allowing for a test of these gaugino mass relations. In Fig. 26 we present the deviations δ_+ and δ_- in $\mathcal{F}$-$SU(5)$. Fig. 26 demonstrates that δ_+ and δ_- are indeed small, with $\delta_+ \approx 6\%$ and $\delta_- \approx -11\%$ for $\mathcal{F}$-$SU(5)$. However, these deviations are larger than the F-$SU(5)$ second loop deviations in Ref. [99]. Thus, it is imperative we understand the reason for the larger deviations in $\mathcal{F}$-$SU(5)$.

In an effort to compare the deviations in $\mathcal{F}$-$SU(5)$, we calculate the deviations in mSUGRA, *i.e.*, the minimal $SU(5)$ model with gravity mediated supersymmetry breaking. We consider two cases: (i) Two-loop RGE running for the SM gauge couplings and one-loop RGE running for the gaugino masses; (ii) Two-loop RGE running for both the gauge couplings and the gaugino masses. We find that in case (i), the order of M_i/α_i is the same as that in $\mathcal{F}$-$SU(5)$ given in Eq. (5.10), while in

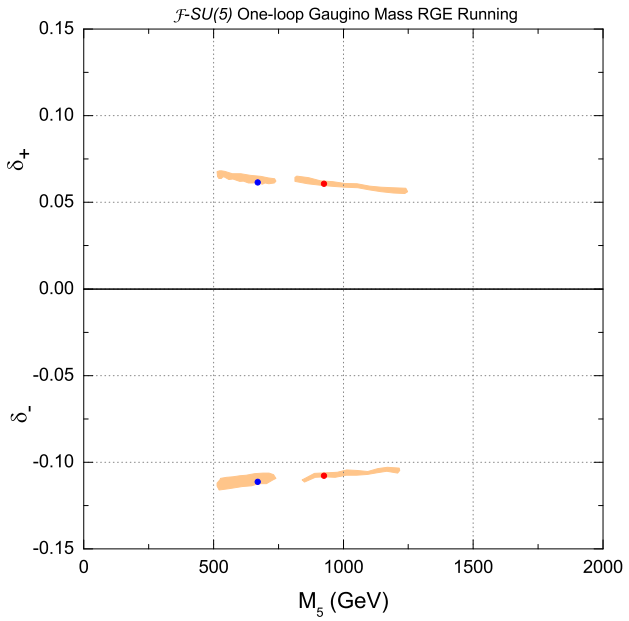

Fig. 26. The δ_+ and δ_- parameters for $\tan\beta = 51$, $A_0 = m_0$ for $\mathcal{F}$-$SU(5)$. The shaded regions satisfy all experimental constraints. The $\mathcal{F}$-$SU(5)$ benchmark point in Table XXV is annotated by the blue points, while the benchmark point in Table XXVI is annotated by the red points. For the benchmark point in Table XXV, we find $\delta_+ = 0.0615$ and $\delta_- =$ -0.1113, and likewise, for the benchmark point in Table XXVI, $\delta_+ = 0.0607$ and $\delta_- =$ -0.1077.

case (ii) we have

$$\left(\frac{M_i}{\alpha_i}\right)_{\rm L} = \frac{M_3}{\alpha_3}\ , \quad \left(\frac{M_i}{\alpha_i}\right)_{\rm M} = \frac{M_1}{\alpha_1}\ , \quad \left(\frac{M_i}{\alpha_i}\right)_{\rm S} = \frac{M_2}{\alpha_2}\ . \tag{5.11}$$

We present the small deviations δ_+ and δ_- in mSUGRA for both case (i) and case (ii) in Fig. 27. We find that for case (i) we have $\delta_+ \approx 1.8\%$ and $\delta_+ \approx -1.6\%$, and for case (ii) we have $\delta_+ \approx 3\%$ and $\delta_- \approx -1.6\%$. These deviations are similar to the F-$SU(5)$ second loop deviations in Ref. [99], and are indeed smaller than these in $\mathcal{F}$-$SU(5)$. Therefore, we conclude that the existence of TeV scale vector-like particles in $\mathcal{F}$-$SU(5)$ enlarge the deviations, thereby presenting a potential opportunity to experimentally infer the underlying theory at high energies since there is a rather compelling need for TeV scale vector-like particles in $\mathcal{F}$-$SU(5)$. On the contrary, unflipped GUTs require no such TeV scale vector-like particles. The vital point here is that an experimental measurement of the two-loop deviations through the $\delta_\pm$ parameters can certainly assist us in determining whether the underlying theory at the string scale is a flipped or unflipped GUT.

There is a noticeable resemblance of the experimentally allowed parameter space in Fig. 23 with that of mSUGRA. For comparison, we study a recent analysis of the mSUGRA parameter space in [116]. Upon closer examination of the two models, we see that it appears the vector-like particles and partial gaugino mass universality are shifting the upper narrow WMAP strip to a larger gaugino mass and smaller m_0. The essential aspect is that the gaugino mass RGE running is changed significantly due to the additional vector-like particles. The consequences of this include a heavier LSP for large m_0 when compared to mSUGRA, with the LSP mass increasing to a limited range centered around 100 GeV. Recall, our benchmark point from the WMAP strip at large m_0 is $m_{\widetilde{\chi}_1^0} = 107$ GeV. In contrast, the LSP mass in the experimentally allowed region of mSUGRA for large m_0 and small $m_{1/2}$ is well below 100 GeV.

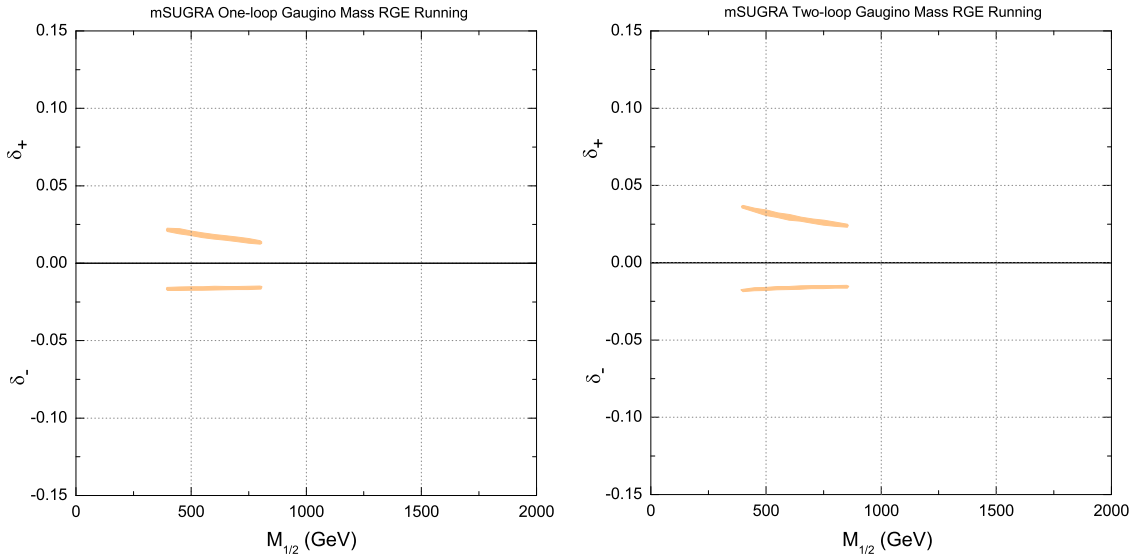

Fig. 27. The δ_+ and δ_- parameters for $\tan\beta = 51$, $A_0 = m_0$ for case (i) (left) and case (ii) (right). The shaded regions satisfy all experimental constraints.

Moreover, the experimentally allowed region of a larger gaugino mass and smaller m_0 gets shifted to a heavier gaugino mass. In these regions of small m_0, as already noted, the WMAP relic density is generated through stau-neutralino coannihilation. However, as we described, in $\mathcal{F}$-$SU(5)$ this region of large M_5 and small m_0 possesses WIMP-nucleon cross-sections well below the CDMS II upper limit.

It is interesting to consider what we could see at the LHC for the $\mathcal{F}$-$SU(5)$ model framework. We calculate the differential cross-sections and branching ratios with `PYTHIA 6.4`, using the revised `SuSpect 2.34` code that includes the effects of the vector-like particle contributions to compute the sparticle masses for input into `PYTHIA 6.4`. The three lightest sparticles for the $\tan\beta = 51$ Table XXV benchmark point are $\widetilde{\chi}_1^0 < \widetilde{\chi}_1^\pm < \widetilde{\chi}_2^0$. The production of gluinos $\widetilde{g}$ and squarks $\widetilde{q}$ have the largest differential cross-sections at the LHC. The $\widetilde{q}$ decays to a gluino and hadronic jet due to the noticeably lighter mass of the gluino in comparison to the squarks, while the $\widetilde{g}$ will produce a neutralino or chargino along with a hadronic jet. The

$\widetilde{\chi}_2^0$ produce Z_0 through $\widetilde{\chi}_2^0 \rightarrow Z_0\widetilde{\chi}_1^0$ with a branching ratio of 64%. We will get b quarks from the remainder of the $\widetilde{\chi}_2^0$ through light Higgs in the process $\widetilde{\chi}_2^0 \rightarrow h_0\widetilde{\chi}_1^0$ with a branching ratio of 36%. These light Higgs will in turn decay to $b\bar{b}$ with a 75% branching ratio. Leptons and hadronic jets will result from the decay $\widetilde{\chi}_1^\pm \rightarrow W^\pm\widetilde{\chi}_1^0$, where this is the only kinematically allowed $\widetilde{\chi}_1^\pm$ process. Thus, this benchmark point will produce mainly W and Z bosons, and some b quarks through light Higgs h_0 at LHC. Additionally, the vector-like particles can couple to SM fermions and Higgs fields via Yukawa interactions, and they can then decay to SM fermions and Higgs fields, as well as the LSP neutralino.

We see quite different LHC states for the benchmark point in Table XXVI. This point resides in the region of the experimentally allowed parameter space that generates the WMAP relic density through stau-neutralino coannihilation. Hence, the four lightest sparticles for this benchmark point are $\widetilde{\chi}_1^0 < \widetilde{\tau}_1^\pm < \widetilde{\chi}_2^0 \sim \widetilde{\chi}_1^\pm$. Here, as in the benchmark point in Table XXV, the gluino is lighter than the squarks, so all squarks will predominantly decay to a gluino and hadronic jet, with a small percentage of squarks producing a neutralino or chargino, plus a jet, and the gluinos will then decay to neutralinos or charginos as well. The result is low-energy tau through the processes $\widetilde{\chi}_2^0 \rightarrow \widetilde{\tau}_1^\mp\tau^\pm \rightarrow \tau^\mp\tau^\pm\widetilde{\chi}_1^0$ and $\widetilde{\chi}_1^\pm \rightarrow \widetilde{\tau}_1^\pm\nu_\tau \rightarrow \tau^\pm\nu_\tau\widetilde{\chi}_1^0$. The LHC final states of low-energy tau in the $\mathcal{F}$-$SU(5)$ stau-neutralino coannihilation region are similar to those same low-energy LHC final states in mSUGRA, however, in the stau-neutralino coannihilation region of mSUGRA, the gluino is typically heavier than the squarks. Again, the strong coupling effects from the additional vector-like particles on the gaugino mass RGE running reduce the physical gluino mass below the squark masses in $\mathcal{F}$-$SU(5)$. As a consequence, the LHC final low-energy tau states in the stau-neutralino coannihilation regions of $\mathcal{F}$-$SU(5)$ and mSUGRA will differ in that in $\mathcal{F}$-$SU(5)$, the low-energy tau states will result largely from neutralinos and charginos

produced by gluinos, as opposed to the low-energy tau states in mSUGRA resulting primarily from neutralinos and charginos produced from squarks.

CHAPTER VI

CONCLUSIONS*

A. One-Parameter Model

We have updated and surveyed the allowed parameter space of the one-parameter model. Our motivation for studying this model stems from the commonality of the universal soft supersymmetry breaking ansatz across multiple types of string compactifications. These include weak coupled and heterotic M-theory vacua, as well as Type IIB flux vacua, in particular the so-called large-volume compactification models. By performing a comprehensive scan of the entire parameter space and filtering the results according to experimental constraints, the allowed parameter space was obtained. In the strict moduli dominant case, we found that there is no parameter space which can satisfy all of the constraints, whereas there is a small parameter space allowed for the dilaton scenario. We identified the probable squark and gluino interactions and presented cascade decay modes that will produce specific favorable collider signatures. The dominant component of these favorable signatures are tau and hadronic jets.

We compared the collider signatures of the one-parameter model to a model with non-universal soft terms, in particular an intersecting $D6$-brane model with

---

*Part of this chapter is reprinted with permission from "Supergravity and Superstring Signatures of the One-Parameter Model at LHC" by J. A. Maxin, V. E. Mayes and D. V. Nanopoulos, 2009, Physical Review D, **79**, 066010, Copyright 2009 by the American Physical Society. Part of this chapter is reprinted with permission from "Stringy WIMP Detection and Annihilation" by J. A. Maxin, V. E. Mayes and D. V. Nanopoulos, 2009, Physical Review D, **79**, 123528, Copyright 2009 by the American Physical Society. Part of this chapter is reprinted with permission from "The Search for a Realistic String Model at LHC" by J. A. Maxin, V. E. Mayes and D. V. Nanopoulos, 2010, Physical Review D, **81**, 015008, Copyright 2010 by the American Physical Society.

interesting phenomenological properties. We found that for one particular intersecting $D6$-brane pattern of mass hierarchies, there are possible distinguishing characteristics between these two classes of models. Although there may also be a lot of overlap in the observable signatures of these two models, there are regions of the parameter space of each class which may give strikingly different observable signatures which may be used to distinguish them. Thus, it may be possible for LHC to say something about the structure of the underlying theory at high-energies, e.g. universality vs. non-universality.

A well-motivated framework for studying supersymmetry breaking is to assume that it is dominated by the Kähler moduli and/or the universal dilaton. Such scenarios give rise to very constrained supersymmetry breaking soft-terms which depend only on a universal gaugino mass. In addition, modulus-dominated supersymmetry breaking appears as a generic feature of many string compactifications. We find that the simplest models are not viable, at least under a standard RGE running between the electroweak scale and $M_{GUT} = 2 \times 10^{16}$ GeV. Although these models may have some parameter space which can satisfy experimental constraints, the value of $\tan\beta$ determined at the electroweak scale is not consistent with the B parameter at the GUT scale. Despite this, it is still possible that supersymmetry breaking could be dominated by the moduli if one considers a non-standard RGE running or if the high-energy scale M_{High} at which the boundary condition on the soft-terms is defined is different from M_{GUT}. A non-standard RGE running could result if vector-like matter is introduced at intermediate mass scales. Indeed, the introduction of such vector-like matter is one way of pushing the GUT scale up to the string scale $M_{string} = \mathcal{O}(10^{18})$ GeV. Moreover, the string scale for large-volume Type IIB flux models can be substantially lower than M_{GUT}. Thus, modulus-dominated supersymmetry breaking is possibly still viable under non-minimal assumptions.

B. Intersecting $D6$-brane Model

We have explored the low-energy supersymmetry phenomenology of a near-realistic intersecting $D6$-brane model in Type IIA string theory. The $D6$ model has three generations of SM fermions and exhibits automatic gauge coupling unification. In addition, it is possible to obtain correct masses and mixings for both up and down-type quarks as well as the tau lepton. To date, this is the only known string model where this is possible. We calculated the soft-supersymmetry breaking terms and superpartner spectra satisfying all presently known experimental constraints for the u-moduli dominated SUSY breaking scenario and showed there are regions within the parameter space which may generate both the WMAP observed dark matter density and the diluted relic density in the context of SSC. Five regions in the allowed parameter space were identified that possess a different hierarchy of the four lightest sparticles in the mass spectrum. It was found that only three of these regions can generate the correct WMAP and SSC relic densities. We constructed the final states for regions of the parameter space that can generate the WMAP observed relic density, which consisted of low energy tau and jets in the stau-neutralino coannihilation region, and low energy leptons, high energy neutrinos, and jets in the chargino-neutralino coannihilation region. In the SSC scenario, we found the final states are high energy leptons, high energy neutrinos, and jets. We found that the minimum number of required observables to determine the free parameters is four, although this number of observables could exceed the minimum due to the dissimilar final states between the three regions of the allowed parameter space that can generate the correct relic density. Finally, we discussed how further constraining the parameter space with new measurements can set the maximum number of observables.

Much advancement has been made in the last few years toward the discovery of

dark matter. Current generation direct detection experiments that search for elastic collisions of WIMPs off nuclei have come within shouting distance of the allowed parameter space of models with universal soft-supersymmetry breaking terms such as mSUGRA. Furthermore, the Fermi Gamma-ray space telescope is edging closer to the parameter space of these same models. In light of this experimental progress, it is a good time to start examining the direct and indirect detection parameters of semi-realistic string models. To this end, we began an investigation of the experimental detection parameters for a particular string-derived model with many appealing phenomenological properties. There are various theoretical models currently offered, so our goal is present the phenomenology of a promising new model, in contrast to the usual standard, mSUGRA. In this work, we investigated an intersecting $D6$-brane model, presenting the spin-independent and proton spin-dependent cross-sections. We find that only a small region of the allowed parameter space is within the current limits of the direct detection experiments. Regions with a larger $\Omega_{\chi^o} h^2$ have smaller cross-sections, thus cross-sections for SSC are smaller than those of WMAP. Additionally, we illustrated the galactic gamma-ray flux for this model resulting from neutralino annihilations. We discover that most of the regions of the $D6$-brane model allowed parameter space will be within the sensitivity of the Fermi telescope.

The new results from CDMS II provide a tantalizing hint that we may be on the verge of the first direct detection of dark matter. Combined with data from the now operational LHC as well as indirect detection experiments such as Fermi, it may be possible to finally converge on the fundamental nature of the dark matter. Here, we studied the implications for dark matter direct and indirect detection experiments for a realistic intersecting D-brane model in light of the new results from CDMS II. We found that there are points in the parameter space which are consistent with the CDMS II results, and which satisfy all other experimental constraints. In addition,

we considered the indirect detection gamma-ray flux resulting from neutralino annihilations for these points and find that they are within the sensitivity of the Fermi telescope. Although the two events detected by CDMS II are currently of limited statistical significance, it is very interesting to entertain the possibility that these events are due to dark matter and see what are the implications of this for different models. The next few years should be very exciting as more data arrives from CDMS as well as other experiments.

C. F-Theory

We considered gravity mediated supersymmetry breaking and predicted the exact gaugino mass relation at one loop near the electroweak scale in the F-theory $SU(5)$ and $SO(10)$ models with the $U(1)_Y$ and $U(1)_{B-L}$ fluxes, respectively. The gaugino mass relation presented in this work differs from the typical gaugino mass relations that have been studied in the past, and should be preserved reasonably well at low energy in general. Thus, these F-theory GUTs can be tested at LHC and the forthcoming ILC. We exhibited two concrete scenarios that satisfy all the latest experimental constraints and are consistent with the CDMS II experiment. Most importantly, the gaugino mass relation is indeed satisfied at two-loop level with only a very small deviation.

D. Flipped F-SU(5)

We have considered gravity mediated supersymmetry breaking in $\mathcal{F}$-$SU(5)$. The gaugino masses are not unified at the traditional grand unification scale, though we do indeed obtain the mSUGRA one-loop gaugino mass relation at the electroweak scale. However, the gaugino mass relation will have a small two-loop deviation, and this

deviation may be measurable at the LHC and ILC. There is a considerable need for TeV scale vector-like particles in $\mathcal{F}$-$SU(5)$, while unflipped GUTs, such as mSUGRA or F-$SU(5)$, require no such vector-like particles. In light of this key distinction between flipped and unflipped GUTs, we introduced a parameter to measure the small two-loop deviation from the mSUGRA gaugino mass relation at the electroweak scale.

To implement a numerical analysis, we modified a popular and well-established public RGE code to incorporate the effects of TeV scale vector-like particles. In this work, we employed two-loop RGEs for the gauge couplings, but only considered one-loop RGEs for the Yukawa couplings and soft-supersymmetry breaking terms, though we look to extend this to all two-loop supersymmetry breaking RGEs in our future work. The results lead us to conclude there is a clear disparity in the extent of the deviation between GUTs with vector-like particles, such as $\mathcal{F}$-$SU(5)$, and GUTs without vector-like particles, such as mSUGRA or F-$SU(5)$. The predicted correlation between largeness of the deviation from the mSUGRA gaugino mass relation and the existence of vector-like particles can be tested at the colliders.

Furthermore, we have determined the viable parameter space of this model which simultaneously satisfies all the current experimental constraints and is consistent with the findings of CDMS II. The cross-section of two neutralinos into two gamma-rays for the experimentally allowed regions of the parameter space was computed and assessed against the first published Fermi-LAT measurement. The results showed the $\mathcal{F}$-$SU(5)$ parameter space is consistent with the recent Fermi-LAT findings.

A wealth of experimental data is on the horizon, so it is imperative that phenomenologically appealing GUTs, for instance $\mathcal{F}$-$SU(5)$, be researched so that unambiguous experimental predictions may be presented. These predictions will be key milestones in deducing the underlying theory at high energies as we progress through

the next few exciting years of LHC, direct dark matter detection, Fermi-LAT, and proton decay experiments. We have supplemented the conventional bottom-up analysis of traditional GUTs to include TeV scale vector-like particles, and our results feature encouraging prospects for the experimental determination of whether high-energy theory indeed admits these proposed multiplets. We believe that in the next few years experiment will certainly have something key to say about $\mathcal{F}$-$SU(5)$ in particular and string theory in general.

REFERENCES

[1] J. R. Ellis, J. S. Hagelin, D. V. Nanopoulos and M. Srednicki, Phys. Lett. B **127**, 233 (1983); J. R. Ellis, J. S. Hagelin, D. V. Nanopoulos, K. A. Olive and M. Srednicki, Nucl. Phys. B **238**, 453 (1984).

[2] H. Goldberg, Phys. Rev. Lett. **50**, 1419 (1983).

[3] D. N. Spergel, L. Verde, H. V. Peiris, E. Komatsu, M. R. Nolta *et al.* (WMAP Collaboration), Astrophys. J. Suppl. **148**, 175 (2003); Astrophys. J. Suppl. **170**, 377 (2007).

[4] G. Hinshaw, J. L. Weiland, R. S. Hill, N. Odegard, D. Larson *et al.* (WMAP Collaboration), Astrophys. J. Suppl. **180**, 225 (2009).

[5] I. Antoniadis, C. Bachas, J. R. Ellis and D. V. Nanopoulos, Phys. Lett. B **211**, 393 (1988); Nucl. Phys. B **328**, 117 (1989); Phys. Lett. B **257**, 278 (1991); J. R. Ellis, N. E. Mavromatos and D. V. Nanopoulos, Lectures given at International Workshop on Recent Advances in the Superworld, Woodlands, TX, 13-16 Apr 1993, Published in Woodlands Superworld 1993:3-26 (QCD161:I966:1993) arXiv:hep-th/9311148; J. R. Ellis, N. E. Mavromatos and D. V. Nanopoulos, Mod. Phys. Lett. A **10**, 1685 (1995); Phys. Lett. B **619**, 17 (2005); D. V. Nanopoulos and D. Xie, Phys. Rev. D **78**, 044038 (2008).

[6] A. B. Lahanas, N. E. Mavromatos and D. V. Nanopoulos, PMC Phys. A **1**, 2 (2007); Phys. Lett. B **649**, 83 (2007).

[7] B. Dutta, A. Gurrola, T. Kamon, A. Krislock, A. B. Lahanas, N. E. Mavromatos and D. V. Nanopoulos, Phys. Rev. D **79**, 055002 (2009).

[8] V. N. Lebedenko, H. M. Araujo, E. J. Barnes, A. Bewick, R. Cashmore *et al.*, Phys. Rev. D **80**, 052010 (2009).

[9] J. Angle, E. Aprile, F. Arneodo, L. Baudis, A. Bernstein *et al.* (XENON Collaboration), Phys. Rev. Lett. **100**, 021303 (2008).

[10] CDMS Collaboration, Phys. Rev. Lett. **102**, 011301 (2009).

[11] P. Sorenson, LUX Collaboration, Direct Detection of Dark Matter with LUX, DNP October meeting 2009.

[12] A. Morselli, A. Lionetto, A. Cesarini, F. Fucito and P. Ullio (GLAST Collaboration), Nucl. Phys. Proc. Suppl. **113**, 213 (2002).

[13] A. A. Abdo, M. Ackermann, M. Ajello, L. Baldini, J. Ballet *et al.* (Fermi-LAT collaboration), arXiv:astro-ph.CO/1002.4415.

[14] E. A. Baltz and P. Gondolo, JHEP **0410**, 052 (2004).

[15] J. R. Ellis, K. A. Olive, Y. Santoso and V. C. Spanos, Phys. Rev. D **71**, 095007 (2005).

[16] L. Roszkowski, R. Ruiz de Austri and R. Trotta, JHEP **0707**, 075 (2007).

[17] H. Baer, A. Belyaev, T. Krupovnickas and J. O'Farrill, JCAP **0408**, 005 (2004).

[18] J. Cooley [for the CDMS Collaboration], arXiv:astro-ph.CO/0912.1601.

[19] Heavy Flavor Averaging Group (HFAG) Collaboration, arXiv:hep-ex/0704.3575.

[20] M. Misiak, H. M. Asatrian, K. Bieri, M. Czakon, A. Czarnecki *et al.*, Phys. Rev. Lett. **98**, 022002 (2007).

[21] G. W. Bennett, B. Bousquet, H. N. Brown, G. Bunce, R. M. Carey *et al.* [Muon g-2 Collaboration], Phys. Rev. Lett. **92**, 161802 (2004).

[22] T. Aaltonen, J. Adelman, T. Akimoto, M. G. Albrow, B. Alvarez Gonzalez *et al.* [CDF Collaboration], Phys. Rev. Lett. **100**, 101802 (2008).

[23] LEP Working Group for Higgs boson searches and ALEPH Collaboration, Phys. Lett. B **565**, 61 (2003); W. M. Yao, C. Amsler, D. Asner, R. M. Barnett, J. Beringer *et al.* (Particle Data Group), J. Phys. G **33**, 1 (2006).

[24] E. Cremmer, S. Ferrara, C. Kounnas, and D. V. Nanopoulos, Phys. Lett. B **133**, 61 (1983); J. Ellis, A. Lahanas, D. V. Nanopoulos, and K. Tamvakis, Phys. Lett. B **134**, 429 (1984); J. Ellis, C. Kounnas, and D. V. Nanopoulos, Nucl. Phys. B **241**, 406 (1984) and B **247** 373 (1984); For a review see A. Lahanas and D. V. Nanopoulos, Phys. Rep. **145**, 1 (1987).

[25] J. R. Ellis, D. V. Nanopoulos and K. Tamvakis, Phys. Lett. B **121**, 123 (1983).

[26] J. R. Ellis, J. S. Hagelin, D. V. Nanopoulos and K. Tamvakis, Phys. Lett. B **125**, 275 (1983).

[27] L. Alvarez-Gaume, J. Polchinski and M. B. Wise, Nucl. Phys. B **221**, 495 (1983).

[28] J. L. Lopez and D. V. Nanopoulos, Int. J. Mod. Phys. A **11**, 3439-3478 (1996).

[29] V. Kaplunovsky and J. Louis, Phys. Lett. B **306**, 269 (1993).

[30] A. Brignole, L. Ibáñez, and C. Munõz, Nucl. Phys. B **422**, 125 (1994).

[31] J. R. Ellis and D. V. Nanopoulos, Phys. Lett. B **110**, 44 (1982).

[32] I. Antoniadis, J. R. Ellis, J. S. Hagelin and D. V. Nanopoulos, Phys. Lett. B **194**, 231 (1987); Phys. Lett. B **205**, 459 (1988); Phys. Lett. B **208**, 209 (1988) [Addendum-ibid. B **213**, 562 (1988)]; Phys. Lett. B **231**, 65 (1989).

[33] Tianjun Li, Phys. Rev. D **59**, 107902 (1999).

[34] V. Balasubramanian, P. Berglund, J. P. Conlon and F. Quevedo, JHEP **0503**, 007 (2005).

[35] J. P. Conlon, F. Quevedo, and K. Suruliz, JHEP **0508**, 007 (2005).

[36] J. P. Conlon, S. S. Abdussalam, F. Quevedo, and K. Suruliz, JHEP **0701**, 032 (2007).

[37] C. M. Chen, T. Li, V. E. Mayes and D. V. Nanopoulos, Phys. Lett. B **665**, 267 (2008); Phys. Rev. D **77**, 125023 (2008).

[38] J. L. Lopez, D. V. Nanopoulos and A. Zichichi, Phys. Lett. B **319**, 451 (1993).

[39] J. L. Lopez, D. V. Nanopoulos and A. Zichichi, Int. J. Mod. Phys. A **10**, 4241 (1995).

[40] J. L. Lopez, D. V. Nanopoulos and A. Zichichi, Phys. Rev. D **52**, 4178 (1995); For a review, see `Searching for the Superworld: A Volume in Honor of Antonino Zichichi on the Occasion of the Sixth Centenary Celebrations of the University of Turin, Italy`, Antonino Zichichi, Sergio Ferrara, Rudolf M. Mössbauer, World Scientific (2007), ISBN 9812700188, 9789812700186.

[41] G. Belanger, F. Boudjema, A. Pukhov and A. Semenov, Comput. Phys. Commun. **176**, 367 (2007); Comput. Phys. Commun. **174**, 577 (2006); Comput. Phys. Commun. **149**, 103 (2002).

[42] A. Djouadi, J. L. Kneur and G. Moultaka, Comput. Phys. Commun. **176**, 426 (2007).

[43] The Tevatron Electroweak Working Group for the CDF and D0 Collaborations, arXiv:hep-ex/0608032v1.

[44] B. Dutta, Y. Mimura and D. V. Nanopoulos, Phys. Lett. B **656**, 199 (2007).

[45] R. Arnowitt, B. Dutta, T. Kamon, N. Kolev, D. Toback, Phys. Lett. B **639**, 46 (2006).

[46] R. Arnowitt, A. Aurisano, B. Dutta, T. Kamon, N. Kolev *et al.*, Phys. Lett. B **649**, 73 (2007).

[47] R. Arnowitt, B. Dutta, A. Gurrola, T. Kamon, A. Krislock, D. Toback, Phys. Rev. Lett. **100**, 231802 (2008).

[48] T. Sjostrand, S. Mrenna and P. Skands, JHEP **0605**, 026 (2006).

[49] F.E. Paige, S.D. Protopopescu, H. Baer, and X. Tata, arXiv:hep-ph/0312045v1.

[50] The CMS Collaboration, J. Phys. G: Nucl. Part. Phys **34**, 995-1579 (2007); http://www.iop.org/EJ/abstract/0954-3899/34/6/S01/.

[51] http://www.physics.ucdavis.edu/∼conway/research/software/pgs/pgs4-general.htm

[52] J. Conway, Third LHC Olympics, UC Santa Barbara, Aug. 24, 2006

[53] D. Feldman, Z. Liu and P. Nath, Phys. Lett. B **662**, 190 (2008).

[54] P. Skands, B. C. Allanach, H. Baer, C. Balazs, G. Belanger *et al.*, JHEP **0407**, 036 (2004).

[55] http://v1.jthaler.net/olympicswiki/doku.php?id=lhc_olympics:trigger-table-what-are-triggers

[56] http://v1.jthaler.net/olympicswiki/doku.php?id=lhc_olympics:chroot

[57] http://wwwphy.princeton.edu/∼verlinde/research/lhco/BOXC/

[58] G. Kane, P. Kumar, and J. Shao, arXiv:hep-ph/0709.4259v1.

[59] R. Blumenhagen, M. Cvetic, P. Langacker and G. Shiu, Ann. Rev. Nucl. Part. Sci. **55**, 71 (2005).

[60] R. Blumenhagen, B. Kors, D. Lust and S. Stieberger, Phys. Rept. **445**, 1 (2007).

[61] B. Kors and P. Nath, Nucl. Phys. B **681**, 77 (2004).

[62] J. A. Maxin, V. E. Mayes and D. V. Nanopoulos, Phys. Rev. D **79**, 066010 (2009).

[63] L. Aparicio, D. G. Cerdeno and L. E. Ibanez, JHEP **0807**, 099 (2008).

[64] M. Berkooz, M. R. Douglas and R. G. Leigh, Nucl. Phys. B **480**, 265 (1996).

[65] M. Cvetic, T. Li and T. Liu, Nucl. Phys. B **698**, 163 (2004).

[66] C.-M. Chen, T. Li and D. V. Nanopoulos, Nucl. Phys. B **740**, 79 (2006).

[67] C. M. Chen, T. Li, V. E. Mayes and D. V. Nanopoulos, Phys. Lett. B **665**, 267 (2008).

[68] C. M. Chen, T. Li, V. E. Mayes and D. V. Nanopoulos, Phys. Rev. D **77**, 125023 (2008).

[69] J. A. Maxin, V. E. Mayes and D. V. Nanopoulos, Phys. Rev. D **81**, 015008 (2010).

[70] A. Font and L. E. Ibanez, JHEP **0503**, 040 (2005).

[71] G. L. Kane, P. Kumar, J. D. Lykken and T. T. Wang, Phys. Rev. D **71**, 115017 (2005).

[72] Tevatron Electroweak Working Group and CDF Collaboration and D0 Collab, arXiv:hep-ex/0808.1089.

[73] D. Feldman, Z. Liu and P. Nath, Phys. Rev. Lett. **99**, 251802 (2007) [Erratum-ibid. **100**, 069902 (2008)].

[74] R. L. Arnowitt, B. Dutta, A. Gurrola, T. Kamon, A. Krislock and D. Toback, Phys. Rev. Lett. **100**, 231802 (2008).

[75] J. A. Maxin, V. E. Mayes and D. V. Nanopoulos, Phys. Rev. D **79**, 123528 (2009).

[76] G. Belanger, F. Boudjema, A. Pukhov and A. Semenov, Comput. Phys. Commun. **180**, 747 (2009).

[77] The SuperCDMS Collaboration, arXiv:astro-ph/0502435.

[78] E. Aprile (The XENON Collaboration), arXiv:astro-ph/0502279.

[79] E. Behnke, J. I. Collar, P. S. Cooper, K. Crum, M. Crisler *et al.*, Science **319**, 933 (2008).

[80] G. J. Alner, H. M. Araujo, G. J. Arnison, J. C. Barton, A. Bewick *et al.*, Phys. Lett. B **616**, 17 (2005).

[81] H. S. Lee., H. C. Bhang, J. H. Choi, H. Dao, I. S. Hahn *et al.* (KIMS Collaboration), Phys. Rev. Lett. **99**, 091301 (2007).

[82] S. Desai, Y. Ashie, S. Fukuda, Y. Fukuda, K. Ishihara *et al.* (Super-Kamiokande Collaboration), Phys. Rev. D **70**, 083523 (2004) [Erratum-ibid. D **70**, 109901 (2004)].

[83] Tevatron Electroweak Working Group and CDF Collaboration and D0 Collab, arXiv:hep-ex/0903.2503.

[84] A. Font and L. E. Ibanez, JHEP **0902**, 016 (2009).

[85] J. Jiang, T. Li, D. V. Nanopoulos and D. Xie, Phys. Lett. B **677**, 322 (2009).

[86] R. Blumenhagen, Phys. Rev. Lett. **102**, 071601 (2009).

[87] J. J. Heckman, G. L. Kane, J. Shao and C. Vafa, JHEP **0910**, 039 (2009).

[88] J. J. Heckman, J. Shao and C. Vafa, arXiv:hep-ph/1001.4084.

[89] R. Donagi and M. Wijnholt, arXiv:hep-th/0904.1218.

[90] J. Marsano, N. Saulina and S. Schafer-Nameki, JHEP **0908**, 046 (2009).

[91] J. Marsano, N. Saulina and S. Schafer-Nameki, arXiv:hep-th/0912.0272.

[92] T. W. Grimm, S. Krause and T. Weigand, arXiv:hep-th/0912.3524.

[93] J. Jiang, T. Li, D. V. Nanopoulos and D. Xie, arXiv:hep-th/0905.3394.

[94] T. Li, arXiv:hep-th/0905.4563.

[95] T. Li, D. V. Nanopoulos and J. W. Walker, arXiv:hep-ph/0910.0860.

[96] G. K. Leontaris and N. D. Tracas, arXiv:hep-ph/0912.1557.

[97] C. Beasley, J. J. Heckman and C. Vafa, JHEP **0901**, 058 (2009).

[98] C. Beasley, J. J. Heckman and C. Vafa, JHEP **0901**, 059 (2009).

[99] T. Li, J. A. Maxin and D. V. Nanopoulos, arXiv:hep-ph/1002.1031.

[100] K. Choi and H. P. Nilles, JHEP **0704**, 006 (2007).

[101] W. S. Cho, K. Choi, Y. G. Kim and C. B. Park, Phys. Rev. Lett. **100**, 171801 (2008); M. M. Nojiri, Y. Shimizu, S. Okada and K. Kawagoe, JHEP **0806**, 035 (2008).

[102] V. D. Barger, T. Han, T. Li and T. Plehn, Phys. Lett. B **475**, 342 (2000).

[103] The CDMS-II Collaboration, arXiv:astro-ph.CO/0912.3592.

[104] J. R. Ellis, K. Enqvist, D. V. Nanopoulos and K. Tamvakis, Phys. Lett. B **155**, 381 (1985).

[105] T. Li and D. V. Nanopoulos, arXiv:hep-ph/1002.4183.

[106] J. Jiang, T. Li and D. V. Nanopoulos, Nucl. Phys. B **772**, 49 (2007).

[107] Y. J. Huo, T. Li, D. V. Nanopoulos and C. L. Tong, in preparation.

[108] J. R. Ellis, J. L. Lopez and D. V. Nanopoulos, Phys. Lett. B **371**, 65 (1996).

[109] J. R. Ellis, D. V. Nanopoulos and J. Walker, Phys. Lett. B **550**, 99 (2002).

[110] T. Li, D. V. Nanopoulos and J. W. Walker, arXiv:hep-ph/1003.2570.

[111] K. Nakamura, Int. J. Mod. Phys. A **18**, 4053 (2003).

[112] S. Raby, T. Walker, K. S. Babu, H. Baer, A. B. Balantekin *et al.*, arXiv:hep-ph/0810.4551.

[113] A. H. Chamseddine, R. L. Arnowitt and P. Nath, Phys. Rev. Lett. **49**, 970 (1982); H. P. Nilles, Phys. Lett. B **115**, 193 (1982); L. E. Ibanez, Phys. Lett. B **118**, 73 (1982); R. Barbieri, S. Ferrara and C. A. Savoy, Phys. Lett. B **119**, 343 (1982); H. P. Nilles, M. Srednicki and D. Wyler, Phys. Lett. B **120**, 346 (1983); J. R. Ellis, D. V. Nanopoulos and K. Tamvakis, Phys. Lett. B **121**, 123 (1983); J. R. Ellis, J. S. Hagelin, D. V. Nanopoulos and K. Tamvakis, Phys. Lett. B **125**, 275 (1983); L. J. Hall, J. D. Lykken and S. Weinberg, Phys. Rev. D **27**, 2359 (1983).

[114] T. Li, J. A. Maxin, D. V. Nanopoulos and J. W. Walker, arXiv:hep-ph/1003.4186.

[115] E. Komatsu, K. M. Smith, J. Dunkley, C. L. Bennett, B. Gold *et al.*, arXiv:astro-ph.CO/1001.4538.

[116] R. Allahverdi, B. Dutta and Y. Santoso, arXiv:hep-ph/0912.4329.

VITA

James A. Maxin received his Bachelor of Science degree in electrical engineering from Southern Illinois University in Edwardsville, Illinois in 1987. He enjoyed a successful career as an Electrical Engineer with the Department of Defense, and as a Senior Design Electrical Engineer with Sony Corporation. He entered graduate study in physics at Texas A&M University in the Fall of 2003, and received his Doctor of Philosophy degree in August 2010. Under the supervision of Dimitri V. Nanopoulos, his research and study interests have included superstring phenomenology.

Dr. Maxin may be reached at 4242 TAMU, College Station, TX 77843-4242. His email address is jmaxin@physics.tamu.edu.